Measured and Predicted Particle Number and Mass Emissions from Spark-Ignition Engines

Department of Mechanics, Mathematics and Management

MECHANICAL AND MANAGEMENT ENGINEERING

Ph.D. Program

SSD: ING-IND/08–FLUID MACHINERY

Final Dissertation

Measured and Predicted Particle Number and Mass Emissions from Spark-Ignition Engines

---

by

Elia Distaso

Referees:

Emer. Prof. Rolf. D. Reitz

Prof. Ing. Nicolò Cavina

Supervisors:

Prof. Ing. R. Amirante

Prof. Ing. M. Napolitano

Coordinator of Ph.D Program:

Prof. Ing. Giuseppe P. Demelio

-XXIX Cycle, 2014-2016-

Alla mia famiglia.

Da loro ho imparato quando le parole
valgono più del silenzio che interrompono.
Ché il sapere non è moneta, ma abito bellissimo
che si consuma attraverso l'uso e l'ostentazione.

"How do you want to be known in my chronicle—as the discoverer of fire, or as the first man to pollute the atmosphere?"

Abstract

Modern engine technologies are subject to increasingly tighter emission standards and recent number-based regulations have become a new challenge, since historically only a mass-based regulation needed to be met. This evolution derives from the need to control the emissions of very fine particles, that are believed to cause more damage than larger ones.

The aim of the present work is to provide further guidance in understanding the mechanisms of particle emission processes in Spark-Ignition (SI) engines. By means of both numerical and experimental investigations, it tries to answer some still open questions related to this complex topic. Different fuels are considered, such as gasoline and other promising cleaner alternatives for the future, including natural gas.

3-D Computational Fluid Dynamics simulation are used as useful additional tool to investigate the fuel-related soot emissions and help explain the experimental-derived results. The modified version of the KIVA-3V code, developed at the Engine Research Center (ERC) of the University of Wisconsin-Madison, is used for the present modeling work. It includes improvements in its ignition, combustion and emission models. In particular, a semi-detailed soot model and a chemical kinetic model, including Poly-Aromatic Hydrocarbon formation, are coupled with a SI model and the G equation flame propagation model for the engine simulations and for predictions of soot mass and particulate number density. The present work improves and extends the laminar flame speed correlations for several fuels of practical use in order to assure the correct prediction of combustion phasing and in-cylinder pressure evolution.

The effects of a load increase achieved by pure oxygen addition in gasoline SI engines, as well as, the influence of natural gas composition on combustion are investigated. Furthermore, additional extensive experimental investigations provide more insights about the effects of lubricant oil on particle emissions from both gasoline and natural gas SI engines. In this last case both Port Fuel and Direct Injection mode are considered.

The experimental tests were performed at the “Istituto Motori CNR”, Italy.

Contents

Abbreviations

A_2	Naphthalene
A_4	Pyrene
ABDC	After Bottom Dead Center
ATDC	After Top Dead Center
Ba	Barium
BBDC	Before Bottom Dead Center
C_2H_2	Acetylene
C_2H_6	Ethane
C_3H_8	Propane
Ca	Calcium
CAD	Crank Angle Degree
CFD	Computational Fluid Dynamics
CH_4	Methane
CNG	Compressed Natural Gas
CO	Carbon Monoxide
CO_2	Carbon Dioxide
COV	Coefficient Of Variation
CTC	Characteristic Timescale Combustion (model)
Cu	Copper
CVS	Constant Volume Sampling
DI	Direct Injection
DNS	Direct Numerical Simulation
DOC	Duration of Combustion
DOI	Duration Of Injection
DPF	Diesel Particulate Filter
DPIK	Discrete Particle Ignition Kernel
EGR	Exhaust Gas Recirculation
EVO	Exhaust Valve Opening

Fe	Iron
GDI	Gasoline Direct Injection
HC	Hydrocarbons
HCCI	Homogeneous Charge Compression Ignition
HHR	Heat Release Ratio
IMEP	Indicating Mean Effective Pressure
IVC	Intake Valve Closure
LTC	Low Temperature Combustion
MBF	Mass Burned Fraction
Mg	Magnesium
MN	Methane Number
Mn	Manganese
MUHCs	Methane Unburned Hydrocarbons
N_2	Nitrogen
Ni	Nickel
NO_x	Oxides of Nitrogen
NTC	Negative Temperature Coefficient
P	Phosphorus
PAH	Poly-Aromatic Hydrocarbon
PDF	Probability Density Function
PFI	Port-Fuel Injection
PLIF	Planar Laser-Induced Fluorescence
PM	Particulate Matter
PMP	Particle Measurement Programme
PN	Particle Number
PRF	Primary Reference Fuel
PSDs	Particle Size Distributions
SI	Spark-Ignition
SOI	Start of Injection
TDC	Top Dead Center
TUHCs	Total Unburned Hydrocarbons
TWC	Three-Way Catalyst
UHCs	Unburned Hydrocarbons
VPR	Volatile Particle Remover
WHTC	World Harmonized Transient Cycle
WSR	Well-Stirred Reactors
Zn	Zinc

Nomenclature

Chapter 1 and Chapter 2

A_f	Mean flame front area
c_{m1}	Model constant in transition criterion (Eq. 2.29)
c_{m2}	Model constant in turbulent flame speed correlation (Eq. 2.22)
c_p	Heat capacity
D	Laminar molecular diffusivity
Da	Damk$\acute{}$ohler number
D_T	Turbulent molecular diffusivity
G	non-reactive scalar in G-equation
$\tilde{G}, \widetilde{G''^2}$	Favre mean and variance of non-reactive scalar
I_P	Progress variable in turbulent flame speed correlation
k	Turbulence kinetic energy
Ka	Karlovitz number
$\mathcal{L}$	Markstein length
ℓ_I, ℓ_η	Turbulence integral length scale, Kolmogorov length scale
$\ell_F, \ell_{F,T}$	Laminar flame thickness and turbulent flame brush thickness
$\ell_\delta, \ell_\varepsilon$	Inner layer thickness, oxidation layer thickness
Nu	Nusselt number
Pr	Prandtl number
$\dot{Q}_{spk}$	Electrical energy discharge
Re	Reynolds number
Sc	Schmidt number
S_L^0, S_T^0	Unstretched laminar and turbulent flame speeds
S_{plasma}	Plasma velocity
t_F	flame/chemical time scale
t_I, t_η	Turbulent integral and Kolmogorov time scales

$\mathbf{u}, u'u''$	Flow velocity vector, conventional average turbulence intensity, Favre average turbulence intensity
$\mathbf{u}_{vertex}$	Vertex velocity in KIVA
V	Fluid volume
V_S	Volume swept by the mean flame front in a flame-containing cell within s timestep dt
α_T	Turbulent thermal diffusivity
ε	Dissipation rate of turbulence kinetic energy
κ	Mean flame front curvature
λ	Heat conductivity of fluid
ν_T	Turbulent kinematic viscosity
ρ	Fluid density

Chapter 4

ϕ	Equivalence ratio
p_0	Room pressure
p_u	Unburned mixture pressure
T_0	Room temperature
T_u	Unburned mixture temperature
S_L	Laminar flame speed
S_{L0}	Laminar flame speed at room conditions
α	Temperature influence exponent
β	Temperature influence exponent
B_m, B_2, ϕ_m, S_{u0}	Coefficients in Metghalchi et al.'s correlations
$\alpha_0, \alpha_1, \alpha_2$	Coefficients for exponent α
b_0, b_1, b_2	Coefficients for exponent β
Z, W, η, ξ, σ	Coefficients in "Gülder's formulation" for pure compounds
$\nu, \tau, \varepsilon, \Omega$	Coefficients in "Gülder's formulation" for fuel mixtures
χ	Volume fraction of other compounds in methane fuel mixtures

Chapter 6

$\dot{m}_i$	Mass flow rate
A_{inj}	Nozzle cross section area of the injector
p_i^0	Total injection pressure
T_i^0	Total injection temperature
R_i	Specific heat ratio
γ_i	Specific heat ratio
f_{inj}	Injection frequency
f_{inj}^{ref}	Reference injection frequency
Δt_i	Duration of injection
Γ	Corrected mass flow rate
i	Refers to either methane or propane

List of Figures

List of Tables

"Once it was well known that cigarettes
increased the incidence of lung cancer,
the obvious remedy was to stop smoking,
but the desired remedy was
a cigarette that did not cause cancer.

When it became clear that the internal-combustion engine
was polluting the atmosphere dangerously,
the obvious remedy was to abandon such engines,
and the desired remedy was
to develop non-polluting engines."

— Isaac Asimov, *The Gods Themselves*

Introduction

Over the past several years road transportation has seen significant advances in what are considered alternative technologies. Energy storage, electric drive systems, and fuel cell technologies all seem to be poised to find a significant place in the automotive marketplace [1–3]. However, it would be a mistake to believe that such technologies will completely replace conventional internal combustion engines in short time [4]. The need for practical mid-term solutions that can meet new fuel economy and emissions standards has pushed the development of new technologies for internal combustion engines, comprising innovative combustion techniques [5, 6] as well as their control strategies [7–9].

A possible way to meet present emission requirements being considered by several researchers consists in the use of alternative fuels, since it has been found that fuel selection impacts the power output and exhaust emission of vehicles [10–13]. Therefore, investigating the behavior of alternative fuels, as well as of their mixtures, represents a practical solution for the automotive sector, until more advanced technologies are available that are economically attractive. Natural gas represents one of the most concrete alternatives to conventional petroleum fuels (especially in the heavy-duty vehicle segment) since it produces significantly lower emissions, such as particulate

matter (PM) and oxides of nitrogen (NO_x), than conventional diesel engines [14–16]. Natural gas is a mixture of various components whose concentration can significantly change [17] and this can have non-negligible effects on the combustion process and emissions, especially NO_x and particulate. [12, 13, 18–24]. Controlling its composition with addition of hydrocarbons and diluents content could represent a solution for even cleaner and better performing engines.

Soot emissions are characterized by two competing in-cylinder processes, namely soot formation and soot oxidation. The common thought is that inhibiting the formation of soot is the best way to reduce its emissions. However, soot oxidation rates can also have a strong effect on soot emissions levels and improving the oxidation rate can result in beneficial effects. Soot oxidation can be enhanced by increasing the in-cylinder O_2 content. Oxygenated fuels represent an interesting choice and they are often added to gasoline in order to achieve more efficient combustion [10, 25–28]. However, in the engine simulations field, chemical mechanisms for these fuels are still uncertain and ambiguous results can be produced when the effect of oxygenated fuels on gasoline engine combustion is considered [29–31], especially in soot predictions.

Generally speaking, particle characterization from vehicle emissions is a comparatively new field, which has originated in response to concerns about the health effects of inhaled particles in the ambient environment. Recent toxicological findings have suggested that the adverse health effects may not only be dependent on total particulate mass. These epidemiological findings point to the health effects resulting from inhalation of the finest particles that are believed to cause more adverse effects than large particles [32–36]. A few years ago, Particulate Matter (mass) (PM) was the only particulate-emission parameter to be measured. However, PM test methods can fail at today's low emission levels [37] because the fine particles account very little for particle mass, but can contribute significantly to the Particulate Number (PN). Hence, the fine and ultra-fine particles emitted from internal combustion engines have attracted an increasing level of attention, considering that in recent years, it has been recognized that a large proportion of particles emitted from vehicles really lie in the ultra-fine region (< 100 nm diameter or rather $PM_{0.1}$) [38].

This scenario has led to the establishment of new and more stringent regulations for particle number concentration criteria limits. Euro VI limits for heavy-duty vehicles were introduced in Regulation 595/2009, and were amended by Regulations 582/2011 and 133/2014. The Euro 6 limits for light-duty vehicles came earlier and were introduced along with Euro 5 limits under Regulation 715/2007, promulgated in 2007. The most relevant novelty that has be introduced is that, for the first time, a limit PN-concentration have been set. And although toxicological investigations have focused their effort on the potential negative effects of fine and ultra-fine particle engine emissions on health and environment, such a limit has been defined only recently. This is because it is common knowledge that of all the regulated automotive emissions, particulate emissions are most difficult to quantify as they comprise a complex mixture of particles of varying size and composition, each of which may be influenced by many external factors including engine technology, fuel composition, after-treatment and the act of measurement itself. It was recognized that characterization of particle number and size is more complex than total mass measurement, especially for transient tests, and that

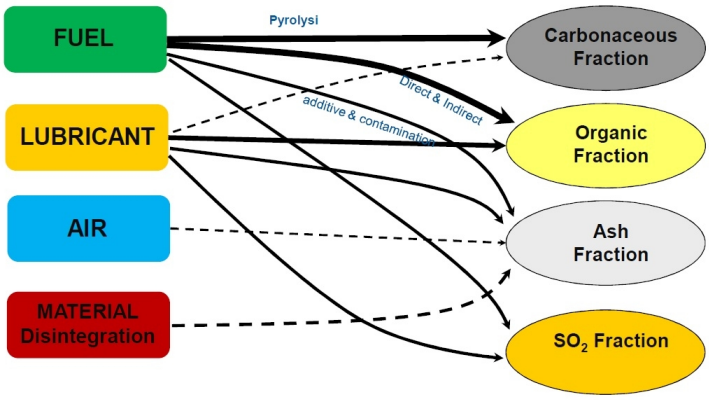

Figure 1: Conversion of fuel, lubricant, air and engineering materials into carbonaceous, organic, ash and sulphate particulate. Adapted from [39].

the repeatability of measurement techniques was not as good as for total mass measured by filter paper methods. Therefore, a great research effort is put worldwide into better understanding the production mechanisms of such emissions and thus meeting number-based regulations.

Particulate emerging from the engine derives mainly from fuel, but the contribution of lubricant oil cannot be neglected or underestimated, especially when the fuel itself produces low levels of soot emissions, such as in the case of premixed natural gas. Air and material breakdown can be additional sources, but these are small in normal circumstances. Figure 1 reports a conceptual representation of the relative significance of each source. If lubricant contribution to particulate mass in in Diesel engine gravimetric measurements of PM has been historically considered negligible, very scarce information is available in the literature about its role in PN emissions in SI engines. It has been shown that particles with size around 10 nm are strongly correlated with lubrication-oil-derived elemental species detected in gravimetric PM samples, indicating the possible existence of nanoparticles below 25 nm formed as a result of lubrication oil passage through the combustion chamber [40].

Motivations

Previous experimental investigations, included in the Master's Thesis work [41], highlighted some important findings and therefore pointed out the need of further investigations about the mechanisms of soot formation in SI engines. The most important results that represent the starting point of this dissertation are here briefly summarized, in order to provide a complete background to the present work.

In that instance, size distribution and concentration levels of particles emitted from a Heavy-Duty, Euro VI, 4-cylinder, SI engine fueled with compressed natural gas were investigated. These emissions were measured using not only an AVL APC489 and the PMP particle counting technique, but also with a fast-response particle size spectrometer (DMS500) so that engine transients could be studied in detail and particle size information could be studied.

The experimental study was conducted over several World Harmonized Transient Cycles (WHTCs) following the procedure defined by the PMP and showed the presence of some spikes, which occur during transient operation conditions, so a large amount of particles are released in a very short time period, reaching values of $1 \cdot 10^{13}$ particles/min, as shown in Figure 2. It was noticed that the most of the spikes appeared as a consequence of an acceleration from rest. This could be attributed to lubricant oil infusion into the combustion chamber or into the exhaust or intake manifold during idling.

In order to isolate the particulate emission mechanics and to correlate it with the rest period that precedes accelerations a further transient test was carried out sampling both from the dilution tunnel and directing from the exhaust gasses upstream of the turbine. Both sampler devices were used. As reported in Figure 3, the relationship between the presence of the spikes and an acceleration following a rest period was thus put clearly in evidence: more than 35% of the total particles emitted were detected (sampling from CVS) in the ten seconds just after each acceleration. It was also pointed

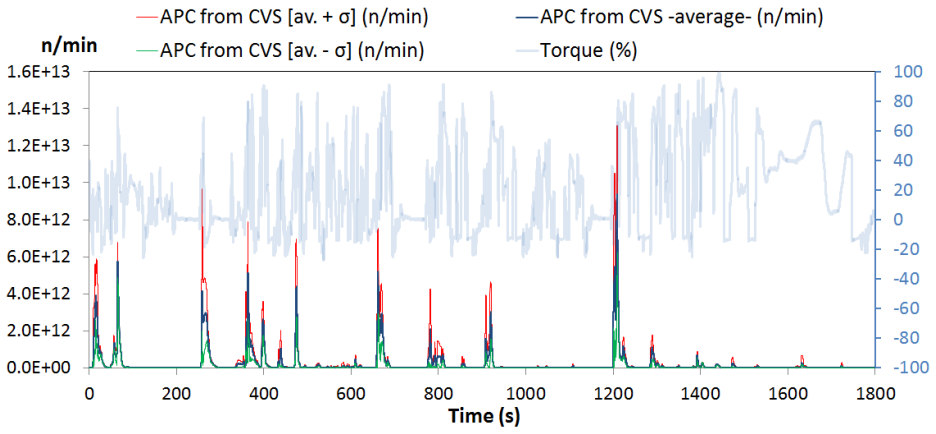

(a)

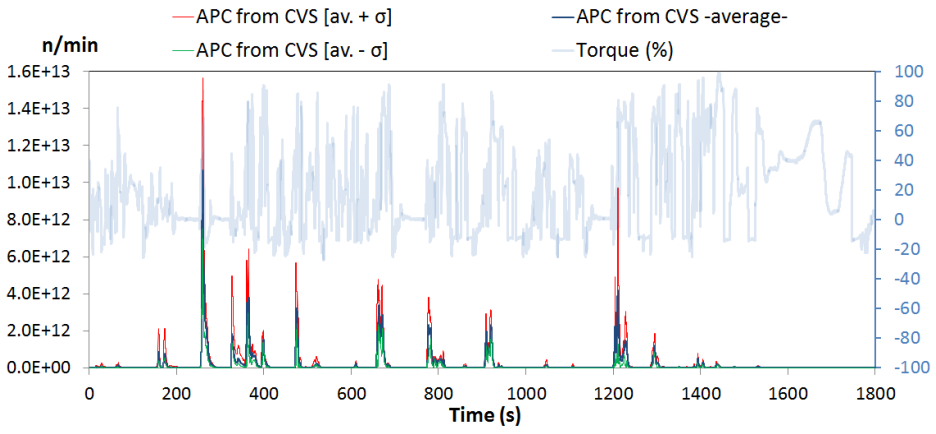

(b)

Figure 2: PN values recorded over several WHTCs, with cold (a) and hot (b) starts, by sampling with APC 489 from the dilution tunnel (CVS). Blue lines: mean values of the number of particles per minute; red and green (upper and lower) lines: 95% confidence interval of the measurements.

out how a longer rest period produces an higher particle number peak in the subsequent acceleration.

This behavior was confirmed by both devices and, in particular, the DMS500 showed that during accelerations the larger part of particles detected upstream of the turbine falls in the nucleation mode distribution (Figure 4). Instead, the following stationary operating conditions are characterized by a predominance of accumulation mode particles. A conclusion of the transient analysis was that the intake system could

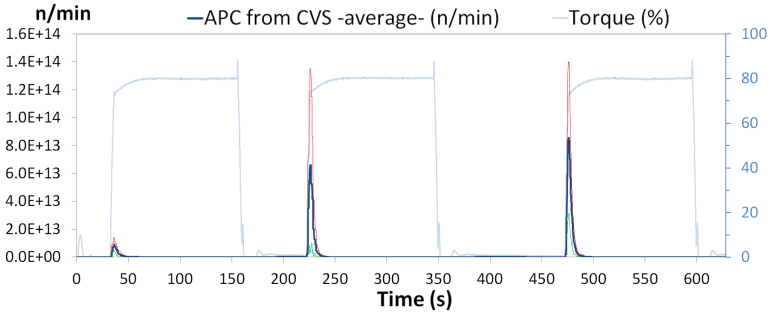

Figure 3: Particles per minute recorded by APC 489 sampling from CVS during transient test. Blue lines: mean values of the number of particles per minute; red and green (upper and lower) lines: 95% confidence interval of the measurements.

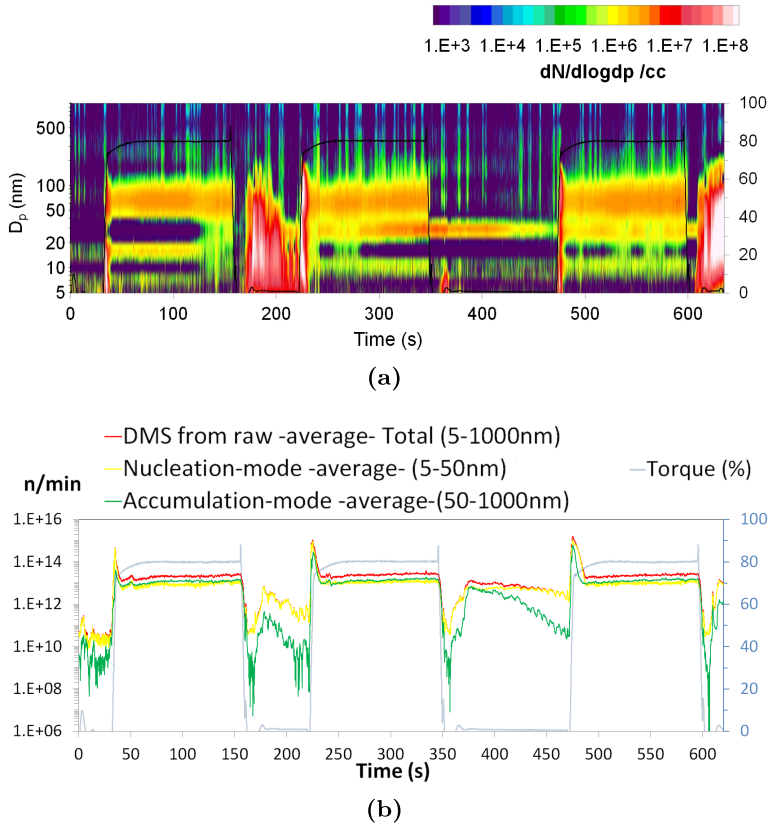

Figure 4: Granulometric distribution (a) and decomposition of total number of particles (red line) in the nucleation (yellow) and accumulation (green) modes (b) obtained by DMS500 sampling from the exhaust flow upstream turbine during transient tests.

play an important role in providing oil contamination. Additional information can be found in [11].

These results suggested that other possible sources besides the fuel combustion which can affect soot formation need to be taken into consideration as well as fuel combustion, and the oil is the main candidate.

Aim and outline

The aim of the present work is to provide further guidance in understanding the mechanisms of particle emission processes in SI engines, by means of both numerical and experimental investigations. Both gasoline and natural gas were considered as fuels. Following the evidences derived from the above-discussed work, 3-D numerical simulations were used as useful additional tool to investigate the fuel-related soot emissions and help explain the experimental-derived results. Additional experiments were designed with the aim the isolate the contribute of external sources to particle emissions, i. e., the lubricant oil. In this last case both Port Fuel and Direct Injection mode were considered. The experimental tests were carried out at the "Istituto Motori CNR", Italy.

Some fundamental concepts are first presented, so that, the reader can be more easily introduced into the main discussion regarding the obtained results that are presented in the subsequent chapters. In Chapter 1 an essential background on soot formation in internal combustion engines is provided. The most plausible chemical formation paths, particulate compositions, engine sources are here described. Other basic notions on the laminar and turbulent flame propagation theories, as well as an introduction to the application of detailed chemical kinetics to the engine combustion modeling are provided as well. Finally, an overview on different existing soot modeling approaches is provided.

Chapter 2 contains details about the numerical model used in the simulations. A description of the main sub-models implemented is presented, i.e., the G-equation model for simulating the turbulent flame propagation and the semi-detailed soot model used for the particulate emissions prediction.

In Chapter 3, 3-D Computational Fluid Dynamics (CFD) simulations of one of the four cylinders of the engine used during the Master's Thesis experimental campaign provided preliminary important results about the role that external sources can have on soot emissions.

Chapter 4 offers accurate empirical correlations for laminar flame speeds, developed for several practical fuels as a function of equivalence ratio and unburned mixture temperature and pressure over a wide range of operating conditions. An accurate as possible formulation for laminar flame speeds is needed for successful simulations.

In order to provide more insight into the effects of a load increase achieved by pure oxygen addition in gasoline SI engines, Chapter 5 looks at results deriving from both 3-D CFD simulations and experimental measurements. Such an approach provided additional basic information about oxygenated fuels combustion, while avoiding still existing uncertainties relating to chemistry models.

The influence of natural gas composition on combustion in SI engines is investigated in Chapter 6. Methane/propane mixtures were realized to isolate the effects of a variation of the main constituents in natural gas on engine performance and associated pollutant emissions. An innovative experimental procedure was designed to obtain precise real-time mixture fractions injected directly into the intake manifold.

Chapter 7 provides a deep analysis about the role of lubricant oil on particle emissions from both gasoline and Compressed Natural Gas (CNG) SI engines by means of an extensive experimental campaign designed for this very purpose. Three different ways of feeding the extra lubricant oil and two fuel injection modes – Port Fuel Injection (PFI) and Direct Injection (DI) – were investigated to mimic the different ways by which lubricant may reach the combustion chamber.

For the last-mentioned four Chapters, a brief literature review precedes the main discussion, providing some of the most recent and relevant findings related to the treated topics. Some conclusions and possible future works are reported as well at the end of each one.

A summary of the work and some recommendations for future research are given in Chapter 8.

Measured and Predicted Particle Number and Mass Emissions from Spark-Ignition Engines

Fundamentals 1

1.1 Background to soot formation in internal combustion engines

In this opening Chapter, an essential background on soot formation in internal combustion engine, togheter with fundamental notions on engine combustion modeling are provided. An overview on different existing soot modeling approaches is provided as well.

Chemical soot formation path

The formation of soot, conceptually, is known to follow the route depicted in Figure 1.1. Pyrolytic reactions break down the original fuel molecules, producing primarily smaller hydrocarbons, in particular acetylene (C_2H_2). The initial step in the production of soot is the formation of the first aromatic species from these aliphatic hydrocarbons, at less than 3 nm. The aromatic species grow by the addition of other aromatic and smaller alkyl species to form larger polyaromatic hydrocarbons (PAH). Carbon is added, and hydrogen removed, until spherules emerge at 20–50 nm. During this growth process the spherules themselves agglomerate, with surface growth occurring in parallel by addition of other aromatic and smaller alkyl species to form larger PAH. Continued growth of the PAH leads eventually to the smallest-identifiable soot particles with diameters of the order of 1 nm and with masses of around 1000 u [42]. The fourth mechanism, oxidation, opposes the other mechanisms, and in fact culls soot at any stage: as precursors, nuclei, spherules or agglomerates. Some workers include a carbonization stage (not depicted), in which polyaromatic layers are aligned, or perhaps realigned, and amorphous carbon is transformed into graphitic carbon [43].

To separate and describe these mechanisms in a tidy, linear manner is convenient, but this chronology is artificial. Overlapping to hugely varying degrees, different mechanisms

rise to prominence in different regions of the combustion chamber at different times, as pressure, temperature and air–fuel ratio dictate. None of these mechanisms is likely to enjoy wholehearted independence, and nucleation, surface growth and agglomeration probably compete with one another to some extent – and not just with oxidation. For example, as the amount of growth material is presumably finite, there is, perhaps, competition for this material between nucleation and surface growth.

The production of soot particles in a flame is inherently a chemically-controlled phenomenon. Low molecular weight (gaseous) hydrocarbons are converted to essentially solid carbon in just a few milliseconds. Thermodynamics alone cannot describe this process since soot is formed beyond regimes where it is thermodynamically stable relative to the oxides of carbon. Hence, chemical kinetics play an important role in soot production. Chemistry occurs during nearly all phases of soot production: inception, surface growth, aging, and surface oxidation. In addition, it is now recognized that soot may participate chemically in the reduction of another undesirable pollutant, nitric oxide [42].

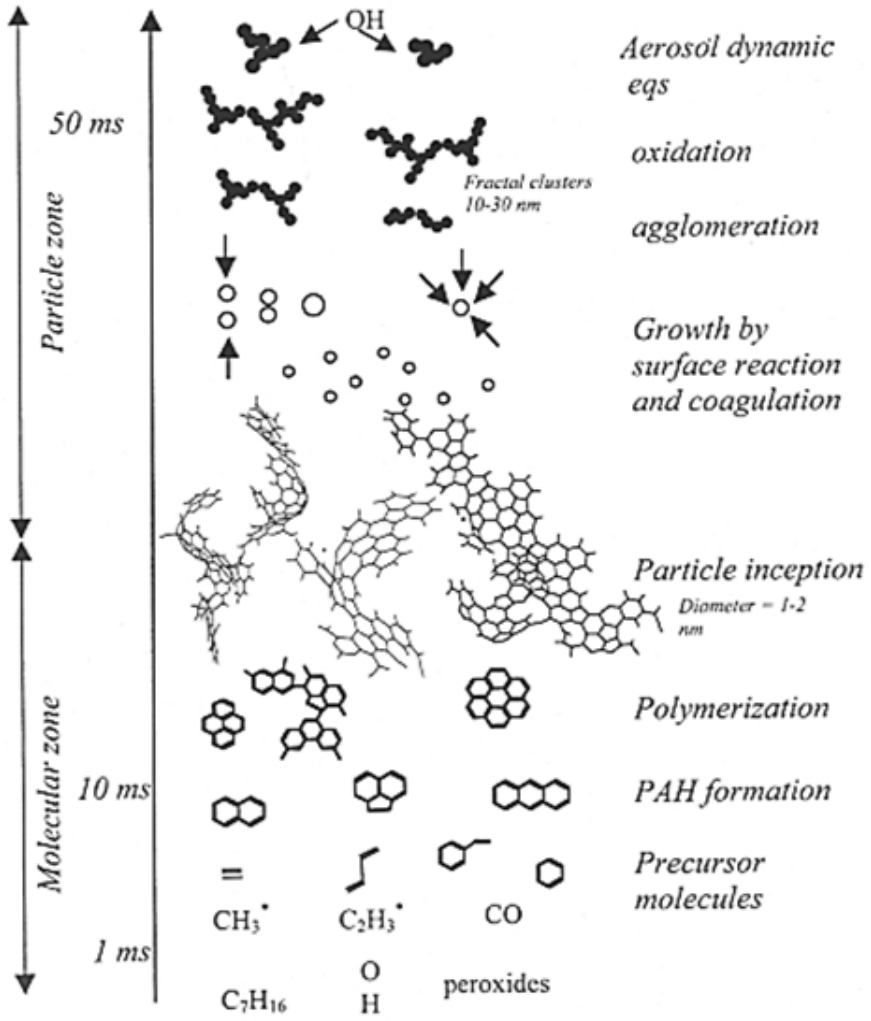

Figure 1.1: Conceptual scheme for the formation of soot.

Particulate composition

The chemical composition of particulate can be represented through the four-layered conceptual model depicted in Figure 1.2. At the first level, everything is included that might be captured when exhaust gas is passed through a filter, with the sole exception of condensed water, as prescribed by the soot measurements regulations.

Upon heating, some material evaporates, and some does not. This divides the particulate into that which is volatile or soluble, and that which is nonvolatile or insoluble. Thereafter, there are five clear subgroups: sulphates, nitrates, carbonaceous, organics and ash.

When exhaust gas is passed through a filter and the particles collected thereon are examined in an electron microscope, the image that it is possible to observe has the aspect reported in Figure 1.3(a), reported from [44]. Figure 1.3(b), by means of a conceptual representation proposed by Eastwood [39], summarizes the main features that can be inferred from Figure 1.3(a).

The most immediately striking aspect of Figure 1.3(b) is the presence of three distinct types of particle, labeled "nucleation mode", "accumulation mode" and "coarse mode". Coarse-mode particles are of varying nature, as this mode includes, also, atypical rust and scale from the exhaust system, for example; these particles are formed from the other two modes. These predecessors lodge somewhere within the exhaust system, become attached to one another, and then re-enter the exhaust stream as much larger, composite particles. This storage–release process makes the coarse mode a random and unpredictable emission. Perhaps because of this fickleness and their comparative rarity, these particles have been little studied. But, as suggested in the figure, they probably consist of a solid core and an outer layer of volatile material. Prior to the mid-1990s, hardly anything was known about nucleation-mode particles, since their dimension lies

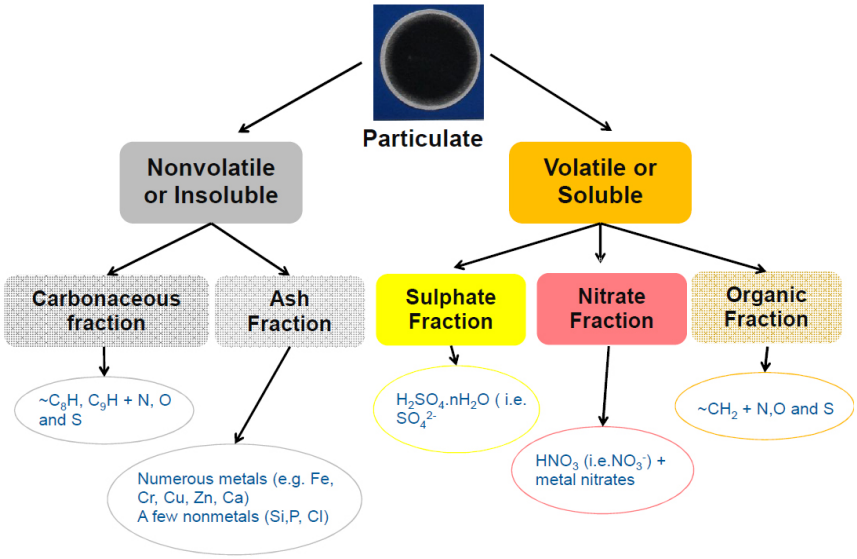

Figure 1.2: Conceptual model of particulate composition, terminating in five distinct fractions: sulphates, nitrates, organics, carbonaceous and ash. Adapted from [39].

at the limit of detection for many instruments. Most, but not all, research suggests that nucleation-mode particles consist of volatile material: this is why they are depicted as spherical in Figure 1.3(b). Other research suggests that some nucleation-mode particles are in fact solid, or at least possess minute solid kernels. These questions are being avidly researched in many research laboratories at the moment.

Accumulation-mode particles have received by far and away the greatest attention. The most immediately obvious feature of accumulation-mode particles is that they consist of a collection of much smaller "primary" particles. These primary particles are sometimes referred to as "spherules" meaning that, while not exactly spherical, they nonetheless quite closely approximate sphericity. The size range for spherules is typically

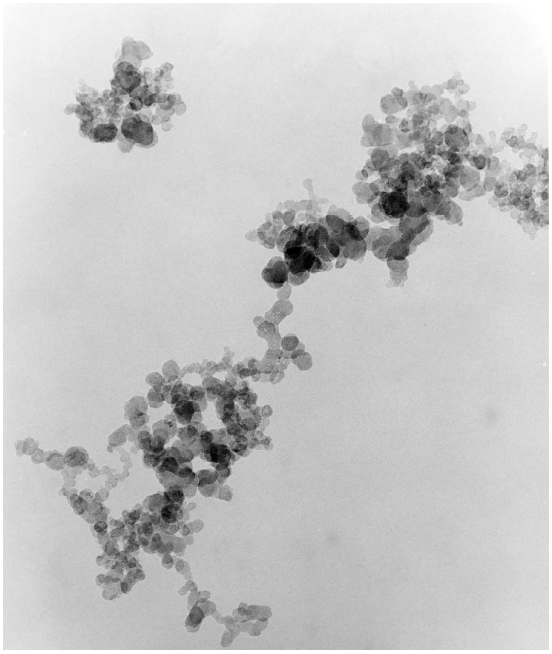

(a)

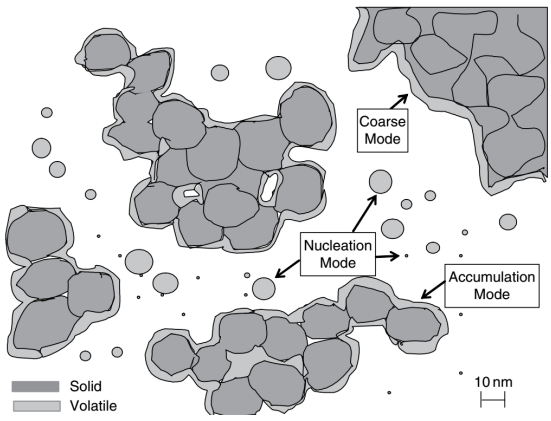

(b)

Figure 1.3: Typical soot particles emitted by an internal combustion engine. (a) micrography showing particles consisting of clumps of spherules, reported from [44]. (b) conceptual representation proposed in [39].

20–50 nm (cf. Figure 1.3(a)). Accumulation-mode particles vary in size because they contain greater or fewer numbers of spherules, and not because the spherules themselves vary in size. The number of spherules that may combine can ranges from tens to thousands. There are highly elaborate and interlinking chains, and clusters of widely varying compactness.

The agglomerate surface is coated by a layer of liquid or semi-liquid material: this is viscid, and penetrates into the pores and internal voids of the agglomerate. Significant compositional dissimilarity thus exists between the surface and the bulk. The adherence of this volatile or semi-volatile layer is what leads to the expression "wet" particulate, in contradistinction to the solid core that remains after a heating process, which is the 'dry' particulate.

The chemical composition (Figure 1.2) corresponds, in a large degree, to the physical representation (Figure 1.3(b)). But, more importantly, the five fractions are defined principally according to the analytical methods, laboratory procedures and test protocols used in their separation and quantification, rather than through any direct correspondence to features presented in Figure 1.3(b).

Sources of particulate emission within the engine

As shown previously in Figure 1, particulate emerging from the engine derives from different sources within the engine. The organic fraction arises from fuel in two ways: direct and indirect. The direct path is when fuel escapes combustion, and simply passes, unburned, through the engine: this might happen, for example, if some fuel is over-mixed with air, such that regions of the charge become too weak to support the flame. The indirect path is when pyrolytic reactions are for some reason interrupted in their conversion of fuel to soot. In this case the organic fraction will contain species not present in the fuel, i.e. those synthesized in the combustion.

The ash fraction arises either from molecules in the fuel that are entirely inorganic, or from inorganic elements that are bonded to organic fuel molecules. These inorganic components are sometimes deliberately added to the fuel, for example to improve various aspects of the combustion; at other times they are there as stowaways or interlopers, having been inadvertently introduced through contamination in the fuel distribution network, or simply because they are natural contaminants in the crude oil [45]. What exactly happens to these inorganic species in the combustion is poorly reported. They probably exist as vapours at typical combustion temperatures. But since their volatilities are low – much lower than any compounds in the organic fraction – their transition into the particulate phase is virtually assured before the exhaust gas is ejected from the engine. For this reason the ash fraction probably emerges slightly before or slightly after the carbonaceous fraction, depending on the elements, and the various compounds formed by these elements.

A significant non-fuel source of particulate emission is always the lubricant. Now, this fugitive oil is often enough perceived as solely contributing to the organic fraction. Lubricant contributes to all four fractions, although admittedly its organic presence has, in the historical picture, been the most keenly felt. With the advent of new emission control technologies, this situation is now changing. Great efforts are made to prevent

the escape of oil, but there is no insurmountable barrier, nor is the invention of such likely for internal combustion engines as traditionally designed. For example, oil residing on the bore is nakedly exposed to hot combustion gases, and hence may evaporate; other entry routes are via the valve stem seals and piston rings, particularly when these components are worn. The amount of oil-derived particulate cannot be predicted from oil consumption, because some of the escaping oil is completely combusted. The amount combusted depends on the entry point, as this decides exposure temperature and residence time. Escaping oil burns up less readily at low load when in-cylinder temperatures are cooler, conditions which also encourage the escape of unburned fuel, so that the two sources tend to reinforce one another.

Hydrocarbon species in the oil are not directly reflected in the hydrocarbons of the organic fraction. Some oil components are more likely to be volatilized than others; some will burn more effectively than others; and some may more readily form partial combustion products. The fuel and oil contributions to the organic fraction are often of comparable significance. Like fuel, oil also contains ashing elements: some of them are intentionally added to improve oil properties, such as anti-wear performance, and others are present naturally.

At completion of the combustion, or opening of the exhaust valve, the particulate phase is still a very, very long way from its final form; and in the exhaust process that follows, continuing transformations take place, the repercussions of which are profound and far-reaching. Initially, exhaust temperatures are still high enough for ongoing reactions, between gases or between particles and gases. Particles grow by agglomeration, and other particles lodge on internal surfaces. The volatile components, i.e. the sulphates, organics and nitrates, adhere to existing particles or nucleate into new particles. Gas–particle partitioning is absolutely central to the emission process. At the exhaust ports, where the temperature is high, only the carbonaceous and ash fractions are solid. But, as the exhaust temperature continues to fall, volatile components begin transferring into the particulate phase. This is the foremost problem in particulate measurement: particulate characteristics inevitably depend on how the exhaust gas has been conditioned. Samples of particulate extracted from various points in the exhaust system demonstrate that most gas-to-particle conversion happens quite late in the emission process – often post-tailpipe.

That wear occurs in engine components suggests another potential source of ash fraction. This does not appear to have been addressed specifically, and it seems that these wear particles are more likely to enter the lubricant than find an entry into the exhaust. In addition, various wear particles can be released from catalytic converters or other after-treatment devices, and from mufflers. Exhaust systems exhibit a remarkable proclivity for particle storage and release. The sudden and unexpected release of wall deposits, as triggered by vibration, temperature cycling, etc., is behind spikes, pulses or bursts of particulate, and this randomness easily leads to fictitious measurements.

Inducted air can be also a source of ash fraction and there are occasions in which it could become important. Depending on the environment, or the time of year, or the condition of the air filter, a vehicle may ingest, for example, mineral dust or road salt. This might be non-negligible if the other fractions are exceptionally low, for example with natural gas engines.

Number Versus Mass

If a sample of exhaust gas is collected and the size distribution of particles suspended therein are examined, the demographic information would not greatly differ from that depicted in Figure1.4 (adapted from Kittelson [46]). This figure plots the size distribution according to number, area and mass. The particles fall readily into three groups previously designed, namely nucleation, accumulation and coarse mode, accordingly to their size. The exact position of each peak on the x-axis varies, and the distribution is usually dominated by one mode, but the trimodality appears to be generic [46]. Each of the three modes, when plotted on a logarithmic x-axis, appears normally distributed, and this distribution is described as 'log-normal'.

A fundamental aspect is the domination of different ranges by mass and number. Most of the particles, according to number, reside in the nucleation mode; while most of the particles, according to mass, reside in the accumulation mode. Each of the two functions, then, inherently emphasizes different modes and different ranges of size.

Since transport and transformation are determined fundamentally by particle size, then mass and number are inevitably affected by these phenomena in completely different ways. If one were solely interested in mass concentration, then inaccuracies in measuring the nucleation mode might not appreciably alter the end result. If, on the other hand, one just wished to investigate the number concentration,then inaccuracies in measuring the accumulation mode would be of lesser concern [39]. Diffusion governs particle transport particularly strongly in the nucleation mode, and so potentially affects the number distribution, whereas inertial deposition has greater implications for the accumulation mode. It turns out that nucleation-mode particles are vastly more vulnerable to measurement falsifications than accumulation-mode particles. The nucleation-mode particles are created or destroyed according to how the exhaust is diluted, whereas the accumulation mode particles consist of a solid carbonaceous core, and are only affected by saturation insofar as this decides their capture or release of volatile compounds.

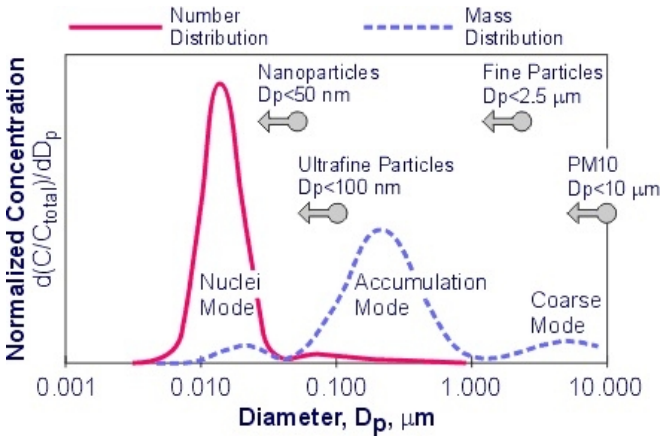

Figure 1.4: Generalised size distributions for typical particles emitted by internal combustion engines, taking spheres and constant density as a first approximation: by number N, surface area S and mass M (adapted from Kittelson [46]).

1.2 Modeling of Spark-Ignition engines

Laminar flame structure

Figure 1.5 schematically shows the structure of a typical premixed flame, where the whole structure is divided into a preheat zone, an inner layer and an oxidation layer [47]. The chemically inert *preheat zone* of dimensionless thickness order unity is followed by the highly diffusive-reactive *inner layer* of thickness of order δ where the fuel is consumed. In the *inner layer* of the asymptotic structure, it is assumed that all concentrations except that of the fuel, which is depleted, may be assumed constant to leading order. This layer is responsible for maintaining the reaction process. Behind the *inner layer* is the oxidation layer of thickness of order ϵ, where CO and H_2 species are oxidized into CO_2 and H_2O.

The flame thickness ℓ_F , that is the total thickness of the three layers, can be estimated by

$$\ell_F = \frac{(\lambda/c_p)\,|_{T^0}}{\rho_u S_L}, \tag{1.1}$$

where λ/c_p is evaluated at the *inner layer* temperature T_0, ρ_u is the density of the unburnt mixture.

The thickness of the *inner layer* ℓ_δ is a fraction δ of the flame thick

$$\ell_\delta = \delta \ell_F, \tag{1.2}$$

while the thickness of the *oxidation layer* is

$$\ell_\epsilon = \epsilon \ell_F, \tag{1.3}$$

and is typically three times larger than ℓ_F [48]. Although perturbations of the *oxidation layer* affect the oxidation of CO, they do not have major consequences for the *inner layer*, because the feedback from the downstream *oxidation layer* to the *inner layer* is weak [49]. Therefore, normally ℓ_ϵ is not used in scaling discussions of turbulent flame structure.

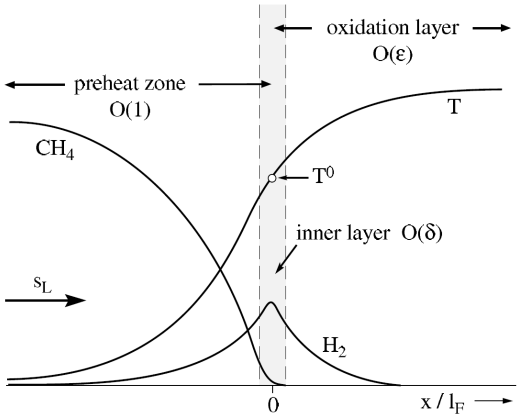

Figure 1.5: Schematic of asymptotic one-dimensional laminar flamelet structure for a methane-air flame (adapted from [47]) versus normalized flame thickness coordinate x/ℓ_F.

Based on S_L and ℓ_F , the flame or chemical time scale t_F can be defined as

$$t_F = \frac{\ell_F}{S_L}. \tag{1.4}$$

Turbulent flame regimes

Figure 1.6 is a regime diagram proposed by Peters [50] based on the following relationships:

$$\frac{v'}{S_L} = Re\left(\frac{\ell_I}{\ell_F}\right)^{-1} = Ka^{2/3}\left(\frac{\ell_I}{\ell_F}\right)^{1/3} = Da^{-1}\left(\frac{\ell_I}{\ell_F}\right). \tag{1.5}$$

where v' is the turbulence intensity, Re the turbulent Reynolds number, ℓ_I is the integral length scale, Da Damköhler number, Ka the turbulent Karlovitz number and the symbol η in Figure 1.6 is used for the Kolmogorov length scale.

The $Re = 1$ line separates the whole domain into a laminar flame regime and a turbulent domain, and the turbulent domain is further divided into four regimes: *wrinkled flamelets*, corrugated flamelets, thin reaction zones and *broken reaction zones*. According to Abraham et al. [51] and Peters [50], the *corrugated flamelets* regime and the *thin reaction zones* regime are of practical interest, especially regarding engine combustion applications.

As seen in Figure 1.6, the *corrugated flamelets* regime satisfies $u' > S_L$ and $\ell_\eta > \ell_F$, and the latter inequality means that the entire laminar flame structure (illustrated in Figure 1.5) is embedded in the Kolmogorov eddies, and is not destroyed by the turbulence. The thin reactions zones regime is bounded by $Re > 1$, $Ka < 1$ and $Ka_\delta > 1$, in which Ka_δ is the Karlovitz number based on the inner layer thickness ℓ_δ (where an approximate relation $\ell_\delta = 0.1\ell_F$ is used in the diagram), which implies that the Kolmogorov eddies are relatively small enough to be able to penetrate into the preheat zone of the laminar flame structure, but still too big to disturb the diffusive-reactive inner layer, where the dominant chemical reactions really occur.

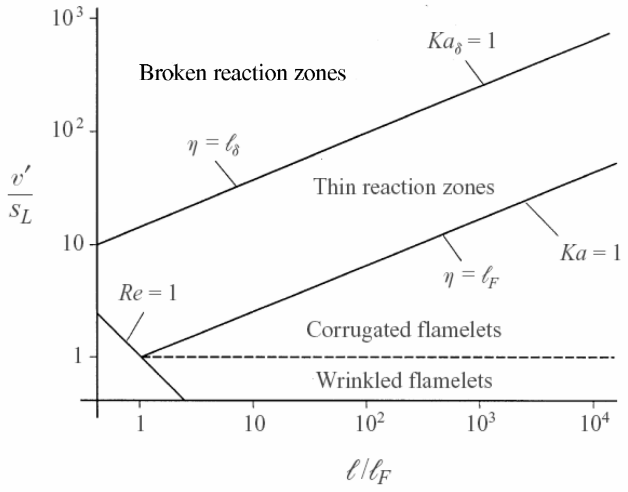

Figure 1.6: Regime diagram for premixed turbulent flames [50].

For the broken reaction zones regime, the inner layer thickness ℓ_δ is large enough so that the Kolmogorov eddies can disturb the chemical processes in this layer. In this case the chemical reaction rates are reduced due to enhanced heat and species losses to he preheat zone, resulting local flame quenching. In conventional homogeneous charge SI engines, normally the inner layer thickness ℓ_δ is small compared to ℓ_η throughout the flame propagation process, so that the flame front maintains its continuous structure, therefore the combustion is not likely to enter the *broken reaction zones* regime. However, in stratified charge DI engines, the inner layer thickness of highly lean or rich premixed flame branches (where the local equivalence ratios are near the flammability limits) may become larger than the sizes of the smallest eddies due to the slow laminar flame speed S_L (cf. Equation 1.1), so that the turbulence/chemistry interactions in the *broken reaction zones* regime explains the local flame quenching and UHC emission formation mechanism in DISI engines.

Turbulent flame structures in SI engines

The combustion process in SI engines always takes place in a turbulent flow field. This flow field is produced by the high shear flows set up during the intake process and modified during compression.

During flame propagation, the whole domain can be divided into three zones as shown in Figure 1.7. The flame front zone is the region where strong coupling between turbulence and chemistry occurs and most of the heat is released. The aero-thermo-chemical process in this zone dominates the flame propagation speeds and therefore the fuel burn rate in SI engines.

Many experiments based on, for example, OH Planar Laser-Induced Fluorescence (PLIF) measurements [53] and Direct Numerical Simulation (DNS) studies using detailed chemical kinetics [54] suggest that the flame front propagation of turbulent premixed flames can be depicted using the flamelet concept.

The premise of *flamelet theory* is that locally, the structure of a turbulent flame is that of a laminar flame subject to the same aero-thermo-chemical conditions. More formally,

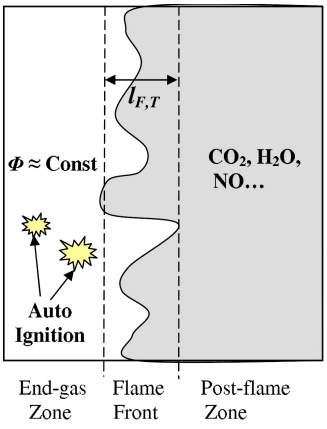

Figure 1.7: Schematic flame structures in SI engines [52]. Φ is the local mixture equivalence ratio and the shaded regions indicate burnt gas regions.

the criteria for flamelet combustion correspond to boundary-layer-like conditions: the dominant spatial gradients must be in a direction normal to the flame front [55]. Based on the flamelet concept, locally, the unburnt mixture is separated from the burnt mixture by a distance equal to laminar flame thickness ℓ_F, where the burnt mixture reaches local and instantaneous chemical equilibrium. Thus, the whole turbulent flame front structure is analogous to a laminar flame structure, with the ℓ_F replaced by a turbulent flame brush thickness $\ell_{F,T}$, which can be defined in terms of the probability of finding the instantaneous flame surface as [56]

$$l_{F,T} = \left[\overline{(x - x_f)^2}\right]^{1/2} = \left[\int_{-\infty}^{+\infty} (x - x_f)^2 P(x) dx\right]^{1/2}, \tag{1.6}$$

where x is the instantaneous flame front position, x_f is the mean flame position, $P(x)$ is the PDF of finding the flame surface at a particular location x within the flame brush.

Within the post-flame zone, relatively slow NO_x formation reactions, CO oxidation reactions and reactions of the H_2-O_2 system dominate the chemical process. In SI engines, the potential auto-ignition of the unburnt mixture ahead of the flame front is of great importance because it can result in severe engine knock under certain conditions [56].

The laminar flame thickness ℓ_F under SI engine conditions is on the order of 0.1 mm for stoichiometric flames and the integral length scale ℓ_I of the turbulence is on the order of 1 cm. Fully developed turbulent flame brush thickness $\ell_{F,T}$ is comparable to the turbulence integral length scale ℓ_I, for example, $\ell_{F,T} = 1.78\ell_I$ was suggested in Ref. [56]. To resolve the flame structure, a very fine mesh is therefore needed in CFD calculations. Thus, it is not realistic to apply the flamelet equation in engine simulations directly. According to Hermann [57], a minimum grid resolution of approximately 6 grid points per turbulent flame brush thickness is needed to resolve the turbulent flame structure. In some SI engines, the flame brush thickness is of the same order of the cell size (2-4mm) in a typical mesh. This means the turbulent flame structure cannot be resolved precisely in the relatively coarse mesh. In the present study, the G-equation model is also adopted to track the mean turbulent flame propagation. By ignoring the detailed flame brush structure, fine numerical resolution is not needed, thus making the models suitable for use in multidimensional modeling of SI engine combustion

Application of detailed chemical kinetics to engine combustion modeling

In recent years, to better understand fundamental engine combustion processes and to further improve the predictability of multidimensional models for engine heat release, emissions, flame quenching, engine knock, etc., attention is being given to models incorporating detailed chemical kinetic mechanisms. Instead of assuming fast chemistry or a global single-step reaction in engine combustion, detailed chemical kinetic mechanisms describe the chemical processes by modeling very detailed reaction pathways and the associated reaction rates. Thus, they are capable of providing more accurate and more insightful information about the real combustion process. For example, the “low temperature chemistry” of hydrocarbon fuels, which is often manifested as a Negative

Temperature Coefficient (NTC) phenomenon could not be accurately captured without the use of detailed chemical kinetics [58].

A large amount of work has been done on developing and validating detailed chemical kinetic mechanisms for hydrocarbon fuel oxidation and pollutant formation [59, 60]. The fuel components studied in the literature cover a broad range of heavy and light molecules, including alkane, alkene, alkyne, aromatics and oxygenates.

Regarding the application to engine combustion, most previous efforts have focused on the predictability of the autoignition delay time, laminar burning velocity, and NO_x and soot emissions of fuel/air mixtures under a wide range of engine operating conditions [61, 62]. In developing detailed chemical kinetic mechanisms, experimental data measured in numerous devices are commonly used for mechanism validation, such as ignition delay time measurements in rapid compression machines and shock tubes [61, 63], and laminar flame speed measurements in constant volume bombs [60, 64]. Further, research on mechanism reduction [62, 65] and parallel computing techniques have made it computationally affordable to incorporate reduced detailed chemical kinetic mechanisms into multidimensional engine simulations.

Multidimensional CFD coupled with detailed chemistry has been successfully applied to conventional diesel combustion and Homogeneous Charge Compression Ignition (HCCI) combustion simulations. For example, Kong et al. [66, 67] incorporated CHEMKIN into the KIVA-3V code by direct integration of detailed chemical kinetics with CFD models, and applied the integrated model (the KIVA-CHEMKIN code) to diesel and HCCI engine simulations. Significant improvements on the prediction of ignition timing, pressure evolution, heat release rate, and NO_x and soot emissions were achieved, compared to simulation results from the standard simplified five-species/eight-reaction "shell" ignition model and the single turbulent time scale CTC combustion model of Kong, Han and Reitz [68]. Recently, Liang [69] focused his work on the application of detailed chemistry to premixed and partially premixed combustion in SI engines.

Although it is still not feasible to resolve the detailed temperature gradients within the turbulent flame front brush due to the limitation of relatively large mesh grid sizes used in practical engine modeling calculations, it is argued that the secondary heat release and pollutant formation, and the low temperature chemistry in the end gas can be better described by using detailed chemical kinetics.

Soot modeling approaches

The chain of events introduced in Section 1.1 presents quite a challenge for the modeller. It should be noted that two domains or levels are encompassed: the molecular system and the particle system.

Soot models developed for the past several decades range from simplistic phenomenological to complicated kinetic models. The detailed review of soot models by Kennedy [42] classified the models as purely empirical correlations, semiempirical correlations, and detailed soot models. Purely empirical correlations are only curve-fits based on experimental data whereas the semiempirical models solve rate equations based on experimental data inputs. Detailed soot models aim to solve rate equations

for soot formation and oxidation and the necessary chemical kinetics leading up to soot inception. Also, the degree of complexity of the semiempirical and detailed soot models varies in the literature.

One of the earliest semiempirical models was developed by Tesner et al. [70] and has been widely used in diffusion flames. The model framework is based on two rate equations, one for the formation rate of soot nuclei and one for the soot number density. Another semidetailed carbon black modeling approach was adopted by Surovikin [71]. In this model, the formation of soot or carbon black was considered to occur in three steps: formation of nuclei, growth of nuclei to a critical diameter termed as incipient particle, and, finally, the growth of those incipient particles to carbon black. Along the lines of the Tesner model, this model also solved two rate equations, one for the formation rate of nuclei and another for the growth of the nuclei diameter.

A two-step soot model based on purely kinetic rates was also proposed by Hiroyasu et al. [72]. The Arrhenius formation and oxidation rates were based on experimental data. The mass rate of soot formation was assumed to be directly proportional to the amount of fuel vapor. The soot formation and oxidation models proposed by Moss et al. [73] for laminar diffusion flames consisted of two rate equations, one for the soot mass fraction, with surface growth and nucleation as the source terms, and one for the soot number density, with nucleation and coagulation as the source and sink terms, respectively.

The choice of precursors for soot formation also varies across the literature. As indicated previously, the Hiroyasu et al. [72] model used the fuel concentration as the precursor for soot formation. However, with the use of reduced or detailed chemistry mechanisms, acetylene (C_2H_2) has been widely used as the soot model precursor species, for example, Leung et al. (1991). The Leung et al. [74] model, first proposed for diffusion flames, took into account soot nucleation through C_2H_2, soot surface growth through C_2H_2, particle agglomeration, and soot oxidation through O_2. Two transport equations for soot species density and soot number density were solved. However, the molecular diffusion terms in the transport equations were replaced by thermophoretic diffusion terms based on the experimental observations of Kent and Wagner [75] on laminar diffusion flames.

A more recent and relatively complex approach for soot modeling has been by the method of moments proposed by Markatou et al. [76]. In this modeling approach, the evolution of soot particles is tracked by three moments, namely, soot number density (M_0), soot volume fraction (M_1), and deviation from the average volume (M_2). For this approach, generally a particle size distribution, for example, a log-normal type distribution is prescribed. Transport equations are solved for the three moments with submodels for particle inception and oxidation. The momentbased approach has been adopted in some studies including flamelet modeling (e.g., Pitsch et al. [77]) and soot modeling in engines using 3-D CFD (e.g., Hong et al. [78]). These types of models also consider the velocity slip between the gas-phase and soot particles (i.e., when the soot particles are in the transition regime between continuum and free molecular flow regimes). Also, thermophoretic diffusion of the soot particles has been considered in this modeling approach. However, the main bottleneck for the application of this soot model for CFD engine simulations is the computational time needed because of the

enhanced model complexities.

Recent works by Celnik et al. [79] and Mosbach et al. [80] focused on a remarkably detailed soot modeling approach applicable to IC engines. The soot model was incorporated in a stochastic reactor model for simulating the engine. The detailed soot model not only provided global soot quantities like mass, number density, volume fraction, and surface area, but also details of soot morphology and chemical composition of the aggregates. A detailed chemical kinetic mechanism incorporating PAH chemistry was included for soot inception through a PAH molecule, such as pyrene (four fused aromatic rings, A4). The model involves soot population balance equations that were solved using Monte Carlo methods. The chemical composition of soot for each aggregate was obtained by monitoring the number of carbon elements, hydrogen elements, and PAHs. Also, for each PAH in the aggregate, the number of armchair, zigzag, free edge, bay sites, and five-membered rings were tracked. The soot submodels included inception stages through pyrene dimerization and pyrene condensation, coagulation, and detailed surface chemistry at the previously mentioned sites for taking into account surface growth and surface oxidation.

In summary, the complexity of soot modeling directly depends on the modeling philosophy. Detailed models are suitable for 0-D or 1-D reactor simulations. However, for 3-D CFD engine simulations the enormous computational demands made by the detailed models allows empirical and semi-empirical approaches to persist. However, semidetailed soot modeling should be formulated in such a way to reduce empiricism so that they can be applied to a wider range of conditions and fuels.

2 Numerical model details

The KIVA-3V code [81–83] developed at the Los Alamos National Laboratory was used for the present modeling work. In particular, the modified version of KIVA-3V developed at the Engine Research Center (ERC) of the University of Wisconsin-Madison was adopted and includes improvements in its ignition, combustion and emission models.

In the next sections a brief description of the main sub-models included in the code is provided.

2.1 CFD code

In the modified version of KIVA-3V developed at the ERC of the University of Wisconsin-Madison, a combustion model based on the level set method (also called the G-equation method) has been implemented into the ERC version KIVA-3V, replacing the standard Characteristic Timescale Combustion (CTC) model, showing better descriptions of premixed and partially premixed turbulent flame propagation [52, 65]. The present work improves and extends the G-equation model by updating the laminar flame speed correlations for several fuels of practical use (Chapter 4) to assure the correct prediction of combustion phasing and in-cylinder pressure evolution.

The multi-dimensional KIVA3v-Release 2 CFD code was coupled with the SpeedCHEM code [84], where KIVA models the fuel preparation, the governing equations for using conservation of mass, momentum and energy, as well as species transport, and SpeedCHEM solves the gas phase fuel chemistry. The chemistry solver is called for each cell and the fuel chemistry is modeled using a kinetic reaction mechanism that contains the species and thermodynamic data for a given fuel, as well as reactions and reaction rate information that describe the oxidation process. Each computational cell is considered to be a well-stirred reactor, and the production rates for each species are calculated and used with the mass fraction, density, and molecular mass to form new species based on the reactions in the mechanism. Species concentration changes are

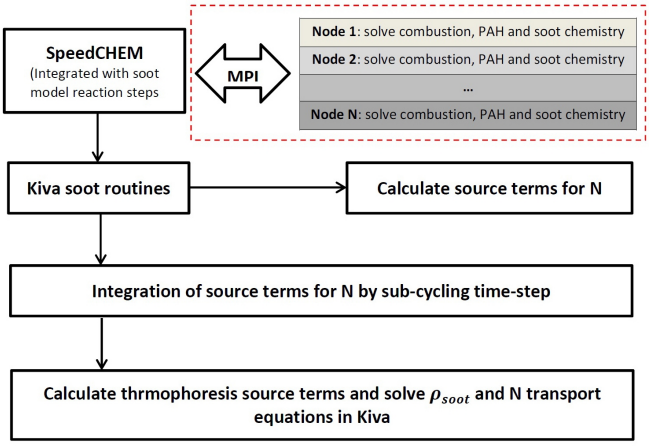

Figure 2.1: Realization of CHEMKIN parallelization of the semi-detailed soot model.

returned to KIVA and these values are used to calculate the energy release at each time step in the calculation [85, 86].

The semi-detailed soot model of Vishwanathan et al. [87] with Jiao and Reitz's improvements [88] is coupled with the Discrete Particle Ignition Kernel model [89] and the G-equation flame propagation model [69, 90] for Spark-Ignition engine simulations and for predictions of soot mass and particulate number density. Other sub-models included in the code are the Generalized RNG (GRNG) turbulence model [91] and the modified wall heat transfer model of Han and Reitz [68], in the modified version by Ra et al. [92] is used to calculate the gas phase wall heat transfer. In addition, a multi-component model, that assumes the fuel to be composed of a finite number of surrogate components which have different properties, is used to represent the actual commercial fuel. The surrogates model both the fuel's physical and chemical properties. The physical properties include density, thermal conductivity, heat capacity, viscosity, surface tension, and volatility. Modeled chemical behavior reproduces the chemical properties such as oxidative stability, ignition temperature, rate of reaction, and sooting behavior.

To save computation time the soot model was parallelized using the Message Passing Interface (MPI) method, as shown in Figure 2.1. In the implementation, it was confirmed that the parallelized semi-detailed soot model predicted exactly the same soot emissions as that from the model working in serial model.

2.2 G-equation Model

The turbulent flame propagation process was modeled by means a method that belongs to the*Flamelet Model* class, a group of widely used methods that are based on tracking a flame front interface either defined by a combustion progress variable, c, or by a non-reacting scalar, G, that divides the flow into burned and unburned portions [56] and which is know as *G-equation model*.

The G-equation method is based on the postulate that the flame propagation is driven by the bulk fluid velocity $\boldsymbol{u}$ of the unburnt mixture ahead of the flame front, and

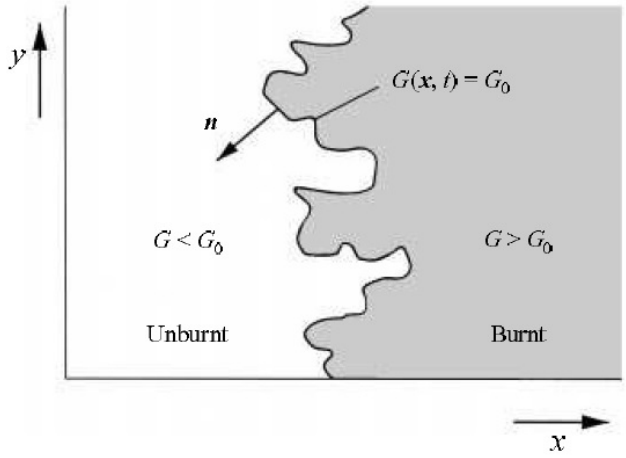

Figure 2.2: Application of G-equation to premixed turbulent flames [56].

the laminar flame speed S_L along the normal direction $\boldsymbol{n}$. The flame front is defined by a $G(\mathbf{x}, t) = G_0$ iso-surface with G_0 taking an arbitrary but fixed value. The flame propagation velocity can be written as:

$$\frac{d\mathbf{x}}{dt} = \mathbf{u} + \mathbf{n}S_L, \tag{2.1}$$

where the normal vector $\boldsymbol{n}$ is defined as

$$\mathbf{n} = -\frac{\nabla G}{|\nabla G|} = -\frac{\nabla G}{\left[(\nabla G)^2\right]^{1/2}}. \tag{2.2}$$

Then the transport equation of G can be derived by differentiating $G(\mathbf{x}, t) = G_0$ with respect to t,

$$\rho\left(\frac{\partial G}{\partial t} + \mathbf{u}\cdot\nabla G\right) = (\rho S_L)\,|\nabla G|. \tag{2.3}$$

Peters [50, 56] subsequently extended Equation 2.3 to the turbulent flame regime. As shown in Figure 2.2, a thin turbulent flame front represented by the $G(\mathbf{x}, t) = G_0$ iso-surface divides the field into an unburnt region where $G < G_0$, and a burnt region where $G > G_0$. The turbulent flame front is regarded as an ensemble of local laminar flamelets with considerations of flame stretch effects on the flame speed S_L. The stretched laminar flame speed S_L can be written as

$$S_L = S_L^0 - \kappa\mathcal{L}S_L^0 - \mathcal{L}S, \tag{2.4}$$

where S_L^0 is the unstretched planar laminar flame speed, $\mathcal{L}$ the Markstein length, κ the flame curvature, and S the strain rate. The flame curvature κ is defined based on G values as

$$\kappa = \nabla\cdot\mathbf{n} = \nabla\cdot\left(-\frac{\nabla G}{|\nabla G|}\right) = -\frac{\nabla^2 G - \mathbf{n}\cdot\nabla(\mathbf{n}\cdot\nabla G)}{|\nabla G|}. \tag{2.5}$$

The strain rate S due to velocity gradients is defined as

$$S = -\mathbf{n} \cdot \nabla \mathbf{n} \cdot \mathbf{n}. \tag{2.6}$$

Based on Equation 2.4, the G-equation is finally written as

$$\rho \frac{\partial G}{\partial t} + \rho \mathbf{u} \cdot \nabla G = \left(\rho S_L^0\right) |\nabla G| - \underbrace{(\rho D_{\mathcal{L}} \kappa)\, |\nabla G|}_{\text{flame curvature}} - \underbrace{(\rho \mathcal{L})\, S |\nabla G|}_{\text{strain rate}}, \tag{2.7}$$

where $D_{\mathcal{L}} = \mathcal{L} S_L^0$.

As discussed in Chapter 1, the average grid length in a typical numerical mesh for current engine simulations is much larger than the laminar flame thickness under engine operating conditions, so the detailed structure of the turbulent flame brush could not be properly resolved. Therefore, the G-equation method is adopted to track the position of the mean turbulent flame front surface [90].

The turbulent G-equation concept has been successfully applied to SI engine combustion simulations by Dekena et al. [93], Tan et al. [90, 94] and Ewald et al. [95]. The present study is built on the G-equation-based multidimensional combustion modeling efforts by Liang et al. [65].

As discussed in Section 1.2 two regimes of practical interest were addressed in the flamelet modeling theory of premixed turbulent combustion by Peters [56]: the *corrugated flamelets regime* where the entire reactive-diffusive flame structure is assumed to be embedded within eddies of the size of the Kolmogorov length scale, l_k; and the *thin reaction zone regime* where the Kolmogorov eddies can penetrate into the chemically inert preheat zone of the reactive-diffusive flame structure, but cannot enter the inner layer where the chemical reactions actually occur.

Equation 2.7 is applicable to the *corrugated flamelets regime* because the local laminar flame structures are undisturbed by the smallest eddies, and the laminar burning velocities are well defined. For the *thin reaction zone regime*, Peters [56] derived another G transport equation with similar form as Equation 2.7 by constructing an equation for the temperature field and making the inner layer temperature iso-surface $T(\mathbf{x}, t) = T_0$ coincide with the iso-surface defined by $G(\mathbf{x}, t) = G_0$. The resulting G-equation for the *thin reaction zone regime* reads

$$\rho \frac{\partial G}{\partial t} + \rho \mathbf{u} \cdot \nabla G = (\rho S_{L,s})\, |\nabla G| - (\rho D \kappa)\, |\nabla G|, \tag{2.8}$$

where $S_{L,s}$ is the displacement speed of the *thin reaction zone* due to normal diffusion and reaction. The differences between Equation 2.7 and Equation 2.8 are the replacements of S_L^0 and $D_{\mathcal{L}}$ in Equation 2.7 by $S_{L,s}$ and D in Equation 2.8, respectively, and the disappearance of the strain term in Equation 2.8. The strain effects is implicitly contained in the displacement velocity $S_{L,s}$ in Equation 2.8. In the corrugated flamelets regime, the strain term is argued to be small compared to other terms in Equation 2.7, and therefore negligible. Based on a dimensional analysis of the order of magnitude of the terms in Equation 2.7 and 2.8, it was shown that $S_{L,s}$ is of the same order of magnitude as the laminar flame speed S_L, and it was also argued that $D_{\mathcal{L}}$ approaches D by neglecting Lewis-number effects (cf. [56]). Consequently, Peters [56] came up with a G-transport equation valid in both regimes:

$$\rho\frac{\partial G}{\partial t}+\rho\mathbf{u}\cdot\nabla G=\left(\rho S_L^0\right)\sigma-\left(\rho D\right)\kappa\sigma, \tag{2.9}$$

where σ is the turbulent to laminar flame surface area ratio or equivalently the flame speed ratio, i.e.,

$$\sigma=\frac{A_T}{A_L}=\frac{S_T^0}{S_L^0}=1+\frac{S_T^0-S_L^0}{S_L^0}=|\nabla\tilde{G}|+\sigma_T, \tag{2.10}$$

and σ_T accounts for the turbulent contribution to the flame surface area ratio σ.

Based on Equation 2.9, a set of Favre-averaged level set equations applicable to both regimes was derived in Ref. [56], including the equations for the Favre mean, $\tilde{G}$ e, and its variance, $\widetilde{G''^2}$, and a model equation for the flame surface area ratio σ_T. These equations, together with the Reynolds averaged Navier-Stokes equations and the $k-\epsilon$ turbulence modeling equations, form a complete set to describe premixed turbulent flame front propagation [56].

Considering the Arbitrary Lagrangian-Eulerian (ALE) numerical method used in the KIVA code, Tan [52] modified the convection term of the $\tilde{G}$ transport equation to account for the change of $\tilde{G}$ value due to the velocity of the moving vertex, $\mathbf{u}_{vertex}$. Thus, the equation set suitable for KIVA implementation is

$$\frac{\partial\tilde{G}}{\partial t}+(\tilde{\mathbf{u}}-\mathbf{u}_{vertex})\cdot\nabla\tilde{G}=\frac{\bar{\rho}_u}{\bar{\rho}}S_T^0|\nabla\tilde{G}|-D_T\tilde{\kappa}|\nabla\tilde{G}|, \tag{2.11}$$

$$\frac{\partial\widetilde{G''^2}}{\partial t}+\tilde{\mathbf{u}}\cdot\nabla\widetilde{G''^2}=\nabla_{\|}\cdot\left(\frac{\bar{\rho}_u}{\bar{\rho}}D_T\nabla_{\|}\widetilde{G''^2}\right)+2D_T(\nabla\tilde{G})^2-c_s\frac{\tilde{\varepsilon}}{\tilde{k}}\widetilde{G''^2} \tag{2.12}$$

$$\bar{\rho}\frac{\partial\bar{\sigma}_T}{\partial t}+\bar{\rho}\tilde{\mathbf{u}}\cdot\nabla\bar{\sigma}_T=\nabla_{\|}\cdot\left(\bar{\rho}D_T\nabla_{\|}\bar{\sigma}_T\right)+c_0\bar{\rho}\frac{\left(-\widetilde{\mathbf{u}''\mathbf{u}''}\right):\nabla\tilde{\mathbf{u}}}{\tilde{k}}\bar{\sigma}_T+ c_1\bar{\rho}\frac{D_T(\nabla\tilde{G})^2}{\widetilde{G''^2}}\bar{\sigma}_T-c_2\bar{\rho}\frac{S_L^0\bar{\sigma}_T^2}{\left(\widetilde{G''^2}\right)^{1/2}}-c_3\bar{\rho}\frac{D\bar{\sigma}_T^3}{\widetilde{G''^2}}, \tag{2.13}$$

where $\nabla_{\|}$ is the tangential gradient operator, $\mathbf{u}$ the fluid velocity, $\mathbf{u}''$ the turbulence intensity, D_T the turbulent diffusivity, and c_s, c_0, c_1, c_2, and c_3 are modeling constants (cf. Ref. [56]), $\tilde{k}$ and $\tilde{\varepsilon}$ are the Favre mean turbulent kinetic energy and its dissipation rate from the RNG $k-\varepsilon$ model [96]. $\tilde{\kappa}$ is the Favre mean flame front curvature defined as

$$\tilde{\kappa}=\nabla\cdot\left(\frac{\nabla\tilde{G}}{|\nabla\tilde{G}|}\right). \tag{2.14}$$

In Equation 2.12, the terms on the l.h.s. describe the local rate of change and convection. The three terms on the r.h.s. account for the change of the Favre variance $\widetilde{G''^2}$ due to turbulent diffusive transport, turbulent production and turbulent dissipation, respectively. In Equation 2.13, the rate of change and convection terms are on the l.h.s.,

the first term on the r.h.s. represents turbulent diffusion transport in the tangential direction, the second term models the production of the flame surface area due to mean velocity gradients, the last three terms describe turbulent production, kinematic restoration, and scalar dissipation of $\bar{\sigma}_T$, respectively [56]. It is noted that the transport equations of $\widetilde{G''^2}$ and $\bar{\sigma}_T$, i.e., Equation 2.12 and 2.13 are not numerically solved in the KIVA framework, instead, they are simplified and used for deriving an explicit expression for the turbulent flame speed S_T^0, which serves as a source term in solving Equation 2.11. Therefore, the convection terms in Equation 2.12 and 2.13) are not affected by the ALE scheme in KIVA.

One significant advantage of the G-equation formulation of turbulent premixed flames is the absence of chemistry source terms in the G transport equation (Equation 2.11). As a consequence, the turbulent flame speed S_T^0 plays a crucial role as a predetermined input.

For steady-state planar turbulent flames, by assuming a uniform turbulence profile which leads to the disappearance of the convection and turbulent diffusion terms in Equation 2.13, and by identifying the production term due to velocity gradients (the second term on the r.h.s. in Equation 2.13 to be relatively small and negligible, Equation 2.13 can be reduced to a quadratic algebraic equation [56]:

$$c_1 \frac{D_T}{\widetilde{G''^2}} - c_2 \frac{S_L^0}{\left(\widetilde{G''^2}\right)^{1/2}} \frac{\bar{\sigma}_T}{|\nabla \tilde{G}|} - c_3 \frac{D}{\widetilde{G''^2}} \frac{\bar{\sigma}_T^2}{|\nabla \tilde{G}|^2} = 0. \tag{2.15}$$

In Ref. [56], the turbulent flame brush thickness $\ell_{F,T}$ was defined as the square root of the Favre variance $\widetilde{G''^2}$,

$$\ell_{F,T} = \left. \frac{\left(\widetilde{G''^2}\right)^{1/2}}{|\nabla \tilde{G}|} \right|_{\bar{G}=G_0} \tag{2.16}$$

and the relation $\ell_{F,T} = 1.78\ell_I$ was derived. This relation together with other analysis on the relations among the turbulence and chemical parameters lead to further reduction of Equation 2.15 to the following form [56]:

$$\frac{\bar{\sigma}_T^2}{|\nabla \tilde{G}|^2} + \frac{a_4 b_3^2}{b_1} \frac{\ell_I}{\ell_F} \frac{\bar{\sigma}_T}{|\nabla \tilde{G}|} - a_4 b_3^2 \frac{u' \ell_I}{S_L^0 \ell_F} = 0. \tag{2.17}$$

Solving Equation 2.17 leads to a turbulent flame speed correlation for planar and fully-developed turbulent premixed flames,

$$\frac{S_T^0}{S_L^0} = 1 - \frac{a_4 b_3^2}{b_1} \frac{\ell_I}{\ell_F} + \left[\left(\frac{a_4 b_3^2}{b_1} \frac{\ell_I}{\ell_F} \right)^2 + a_4 b_3^2 \frac{u' \ell_I}{S_L^0 \ell_F} \right]^{1/2} \tag{2.18}$$

where a_4, b_1, and b_3 are constants from turbulence models, experimental data or DNS study (cf. Ref. [56]), ℓ_I is the turbulence integral length scale, ℓ_F is the laminar flame thickness defined by Equation 1.1. In Equation 1.1, λ/c_p as a function of temperature for air can be approximated by [97]

$$\lambda/c_p = 2.58 \cdot 10^{-5} \left(\frac{T}{298} \right)^{0.7} \qquad \left[\frac{kg}{m \cdot sec} \right]. \tag{2.19}$$

According to Ref. [98], the inner layer temperature T_0 within the laminar flame structure is physically interpreted as the critical temperature at which chemistry is turned on, and is assumed to be a function of pressure only, as given by the relation:

$$T_0 = \frac{E}{ln\,(B/p)}. \tag{2.20}$$

where B and E are fuel type dependent coefficients and are given in Ref. [99] for several $C_1 - C_8$ level fuels.

In spark ignition engines, flame is initiated as a point-source ignition kernel that is not significantly disturbed by the turbulence, therefore the growing rate of the kernel flame radius can not be described by the fully developed value from Equation 2.18 where a linear relation between the turbulent brush thickness and the turbulence integral length scale, i.e., $\ell_{F,T} = b_2 \ell_I = .78 \ell_I$ is used. In the present model, an exponentially increasing term is introduced into Equation 2.18 to account for the laminar to turbulent evolution of the spark kernel flame [69]. The modified turbulent flame speed correlation is written as

$$\frac{S_T^0}{S_L^0} = 1 + I_P \left\{ -\frac{a_4 b_3^2}{b_1} \frac{\ell_I}{\ell_F} + \left[\left(\frac{a_4 b_3^2}{b_1} \frac{\ell_I}{\ell_F} \right)^2 + a_4 b_3^2 \frac{u' \ell_I}{S_L^0 \ell_F} \right]^{1/2} I_P \right\}. \tag{2.21}$$

The term I_P , called a progress variable in the present study, takes the form

$$I_P = \left[1 - e^{\left(-c_{m2} \frac{t - t_0}{\tau} \right)} \right]^{1/2}, \tag{2.22}$$

and now the relation between $\ell_{F,T}$ and ℓ_I becomes

$$\ell_{F,T} = b_2 I_P \ell_I = b_2 \left[1 - e^{\left(-c_{m2} \frac{t - t_0}{\tau} \right)} \right]^{1/2} \ell_I, \tag{2.23}$$

where cm_2 is a model constant. Physically, the progress variable I_P models the increasingly disturbing effect of the surrounding eddies on the flame front surface as the ignition kernel grows from the laminar flame stage into the fully developed turbulent stage. It was shown in Ref. [56] that this progress variable I_P can be obtained by solving Equation 2.12) for an unsteady solution of $\ell_{F,T}$ by assuming that the turbulence quantities D_T , $\tilde{k}$,, and $\tilde{\varepsilon}$ to be constant, and by assuming a uniform turbulence profile. Based on these assumptions, the convection and diffusion terms which include the gradient of $\widetilde{G''^2}$ all vanish in Equation 2.12, and Equation 2.12 can be simplified to an ordinary differential equation:

$$\frac{d\ell_{F,T}}{d\,(t/\tau)} = b_2^2 c_s \ell_I^2 - c_s \ell_{F,T}^2, \tag{2.24}$$

where $\tau = \tilde{k}/\tilde{\varepsilon}$ is used as a non-dimensional time scale. Considering that the laminar flame thickness ℓ_F is normally orders of magnitude less than the turbulent integral

length scale ℓ_I under engine conditions, it is appropriate to choose $\ell_{F,T} = 0$ as the initial condition at spark timing ($t = t_0$). Thus the solution of Equation 2.24 is written as

$$\ell_{F,T} = b_2 \left[1 - e^{\left(-c_s \frac{t-t_0}{\tau}\right)} \right]^{1/2}, \tag{2.25}$$

where $c_s = 2.0$ is a constant coming from spectral closure, according to Ref. [56]. In practical engine simulations, uncertainties associated with other sub-models or even mesh resolution could result in difficulties in matching experimental data. Therefore, the progress variable in Equation 2.23 was selected to be tunable in the present study by introducing a model constant, c_{m2}, to replace c_s in Equation 2.23, while keeping the same scaling relations. However, for a specific engine, c_{m2} is fixed over all operating conditions in the present work.

2.3 Discrete Particle Ignition Kernel Model

The ignition process plays an important role in an SI engine. Ignition can be described in three phases: breakdown, arc and glow discharge [100]. An electrically conductive column is created between the spark plug electrodes during the breakdown phase, where the temperature and pressure is high. Then a shock wave is created that propagates away from the plug. The duration of the initial breakdown phase is very short (∼10 ns) with high-energy transfer efficiency between the electrical energy supplied and the plasma (about 94%). During the early stage (0 to 5 μs), the plasma kernel expands violently and the mass and energy transfer processes are much dominated by the pressure wave. Chemical reaction contributes little to the kernel growth during the early period. Subsequently, the contribution of chemical energy release becomes significant [101]. Although the early stage of ignition is important, it is not practical to resolve the process in detail in engine CFD simulations, because the typical grid-size and time step used is larger than that needed to describe this early stage of ignition precisely. Thus, a relatively simple sub-grid scale model is needed to simulate the early ignition process. In the present work, the growth of the ignition kernel is tracked by using the so-called Discrete Particle Ignition Kernel (DPIK) model developed by of Fan et al. [89] and improved by Tan and Reitz [90].

By assuming a spherical-shaped kernel, the flame front position is marked by Lagrangian particles, and the flame surface density is obtained from the number density of particles in each computational cell, as shown in Figure 2.3. When the kernel grows, the particles move outwards radially from the spark plug electrodes. Assuming the temperature inside the kernel to be uniform, the kernel growth rate is:

$$\frac{dr_{ker}}{dt} = \frac{\rho_u}{\rho_{ker}} \left(S_{plasma} + S_T \right), \tag{2.26}$$

where r_{ker} is the kernel radius, ρ_u is the local unburnt gas density, and ρ_{ker} is the gas density inside the kernel region.

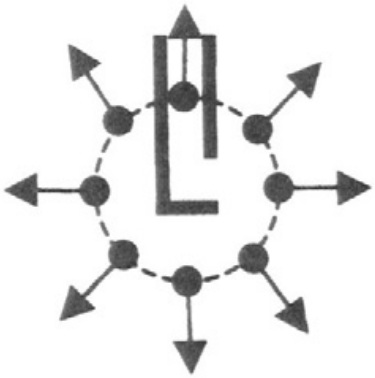

Figure 2.3: Discrete Particle Ignition Kernel model.

Based on the energy balance analysis of the ignition kernel thermodynamic system, the plasma velocity S_{plasma} is given as [90]:

$$S_{plasma} = \frac{\dot{Q}_{spk}\eta_{eff}}{4\pi r_{ker}^2 \left[\rho_u \left(u_{ker} - h_u\right) + p\frac{\rho_u}{\rho_{ker}}\right]}, \tag{2.27}$$

where $\dot{Q}_{spk}$ is the electrical energy discharge rate, η_{eff} is the electrical energy transfer efficiency due to heat loss to the spark plug. $\eta_{eff} = 0.3$, as suggested by Heywood [100] is used in this study. ρ_u and h_u are the density and specific enthalpy of the unburnt mixture, respectively. ρ_{ker} and u_{ker} are the density and internal energy of the mixture inside the kernel.

To account for turbulent strain and curvature effects on the kernel flame, the unstretched laminar flame speed S_L^0 was multiplied by a stretch factor I_0 in Equation 2.21, and the modified correlation is used for calculating the turbulent flame speed, S_T . The stretch factor I_0 takes the following form according to Herweg et al. [102]:

$$I_0 = 1 - \left(\frac{\ell_F}{15\ell}\right)^{1/2}\left(\frac{u'}{S_L^0}\right)^{3/2} - 2\frac{\ell_F}{r_{ker}}\frac{\rho_u}{\rho_{ker}} \tag{2.28}$$

where the second and third terms on the right hand side represent the contributions due to turbulent strain and due to the geometrical curvature of the kernel, respectively. Note that the mean curvature effects are also considered in the G-equation combustion model by the last term of Equation 2.11.

For the cells that do not contain the kernel flame particles, the chemical source terms are calculated by detailed chemistry based on the WSR assumption, using the same treatment as in the G-equation combustion model. Although the transport equation of $\tilde{G}$, Equation 2.11, is not solved in the kernel stage, the $\tilde{G}$ field is constructed based on the positions of the kernel particles for every time step, thus providing the necessary information for classifying the chemical heat release calculations.

The transition from the kernel model to the turbulent G-equation combustion model follows the same criterion as the one used in the previous work by Tan and Reitz [90], namely the transition is controlled by a comparison of the kernel radius with a critical

size which is proportional to the locally averaged turbulence integral length scale, viz.,

$$r_k \geq c_{m1}\ell = c_{m1}0.16\frac{k^{3/2}}{\varepsilon} \tag{2.29}$$

where c_{m1} is a model constant. Compared to the previous work by Tan and Reitz [90], where two different turbulent flame speed correlations were applied in the kernel model and in the G-equation combustion model, c_{m1} is no longer as crucial in the model calibration since the turbulent flame speed correlations used in the kernel model and the G-equation combustion model are essentially consistent [69].

2.4 Heat Transfer Model

In SI engines, heat transfer between the unburnt gas and the chamber walls not only influences the unburnt gas temperature and therefore the flame propagation speed, but also influences the onset of knock, power and efficiency. Therefore, accurate modeling of wall heat transfer is not only necessary for better understanding of heat loss mechanisms, but also important for improving the overall accuracy of engine combustion simulations.

The heat flux is due to gas-phase convection and high temperature gas and soot radiation, and in SI engines, gas phase convective heat transfer is the dominant factor [100]. In the current multidimensional computations, velocity and temperature wall functions (or temperature profiles) are used to solve the near-wall shear stress and heat transfer since the boundary layer of an engine in-cylinder flow is usually thin relative to practical computational grid size. In this study, the wall heat transfer model by Han and Reitz [68] with improvements proposed by Ra et al. [69] was used to calculate the gas phase wall heat transfer.

It is assumed that the mixture within the mean flame brush tends to local and instantaneous thermodynamic equilibrium after the flame front has passed. Tan and Reitz [90] suggested a method for calculating the species density change in the cells containing the flame front by assuming only seven species in their study. Later, Liang and Reitz [69] suggested a new method based on the *sub-grid scale unburnt/burnt volumes* of the flame-containing cells so that a large number of intermediate species could be included (originally developed for 45 species chemistry mechanism).

In the method, it is assumed that the mean flame front surface cuts every flame containing cell into two parts, an unburnt volume (V_u) and a burnt volume (V_b), as shown in Figure 2.4. As the mean flame front sweeps forward, the mixture within the swept volume tends to local equilibrium following a constant pressure and constant enthalpy process. The sub-grid scale volumes are tracked for every time step based on the coordinate information of the cell vertices and the flame surface piercing points.

The species density conversion rate is expressed as:

$$\frac{d\rho_i}{dt} = \rho_u \left(Y_{i,u} - Y_{i,b}\right) \frac{A_{f,i4}}{V_{i4}} S_T^0, \tag{2.30}$$

Where ρ_i is the density of species i, ρ_u is the unburnt gas density, $Y_{i,u}$ and $Y_{i,b}$ are the mass fraction of species in the unburnt and burnt mixtures, respectively. A_f is the

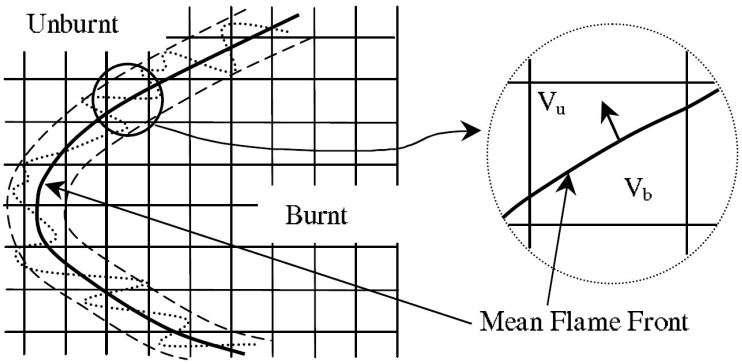

Figure 2.4: Numerical description of the turbulent flame structure and the flame containing cells [69].

mean flame front area and V is the cell volume, $i4$ is the cell index used in the code. S_T^0 is the turbulent burning velocity.

In addition, in the present work, detailed hydrocarbon oxidation chemical kinetic mechanisms are applied to simulate the post-flame reactions and heat release.

2.5 Semi-detailed Soot Model

The soot model used in this work is based on the semi-detailed approach of Vishwanathan and Reitz [87], with Jiao and Reitz's improvements [103] regarding PAH assisted surface growth of soot.

Figure 2.5 shows a schematic diagram for the current model. Multi-component real fuel physical surrogates are applied. On the chemistry side of the diagram (right hand side of red dotted line), the arrows show steps to form soot in the work of Vishwanathan and Reitz [87]. The red arrows show the steps which were added in the modified version of Jiao and Reitz [103].

The main steps for soot formation and oxidation are here reported:

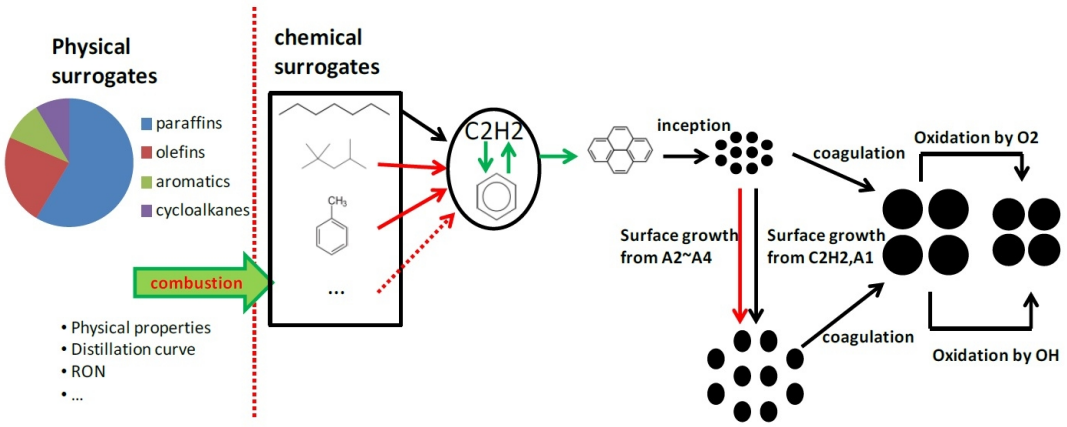

Figure 2.5: Schematic of the soot model with multi-component fuel vaporization and chemistry models.

Particle inception through pyrene (A_4)

The soot particles, $C_{(s)}$, are assumed to be formed from the PAH species pyrene (A_4) via the reaction

$$C_{16}H_{10}(A_4) \xrightarrow{\dot{\omega}_1} 16C_{(s)} + 5H_2, \qquad \dot{\omega}_1 = k_1[A_4], \quad k_1 = 2000, \tag{2.31}$$

where $[A_4]$ represents the concentration of A_4 in mol/cm^3, and k_1 has units of $[1/s]$.

C_2H_2 assisted surface growth

Once formed, the particles grow via the *Hydrogen Abstraction-C_2H_2 Addition* (HACA) mechanism:

$$C_{(s)} + C_2H_2 \xrightarrow{\dot{\omega}_2} 3C_{(s)} + H_2, \qquad \dot{\omega}_2 = k_2[C_2H_2], \tag{2.32}$$

where

$$k_2 = 9.0 \cdot 10^4 e^{-12100/T} \cdot \sqrt{S}, \tag{2.33}$$

and $S = \pi d_p^2 N$, where S is the soot surface area per unit volume in $[1/cm]$, d_p is the particle diameter, and N is the soot number density in $particles/cm^3$.

For each computational cell, the model predicts a unique value for the soot species density and soot particle number density, and therefore a soot particle diameter can be determined for each cell. In this way, the model is locally mono-disperse (on a cell basis) but the soot diameter can vary from one computational cell to the next.

The soot species density can be correlated with soot particle number density based on mass conservation in each computational cell, via.,

$$\left(\frac{\pi}{6} d_d^3 \rho_{C_{(s)}}\right) n = Y_{C_{(s)}} \rho \forall, \tag{2.34}$$

where $n = N\forall$, is the number of particles in a cell, and is the volume of the cell $\forall$. $\rho_{C_{(s)}}$ is the soot density for which the density of graphite ($2.0 g/cm^3$) is used throughout this study, and ρ is the ambient density, Y_{C_s} is the soot mass fraction.

PAH assisted surface growth

In addition, soot growth is modeled via PAH condensation from

$$C_s + PAH_{k,j} \rightarrow C_{(s+k)} + \frac{j}{2} H_2. \tag{2.35}$$

PAHs up to four rings ($A_1 \sim A_4$) are included in the current chemistry mechanism, and they also participate in the soot surface growth. The reaction rates for the condensation of $A_1 \sim A_4$ are $\dot{\omega}_3, \dot{\omega}_7, \dot{\omega}_8, \dot{\omega}_4$, respectively.

Soot coagulation

The soot nucleation process gives rise to a source term in the number density transport equation to be discussed later. A decrease of particle number density is

assumed to occurring during particle coagulation processes, which is modeled using the normal square dependence. The soot particles coagulate following:

$$nC_s \xrightarrow{\dot{\omega}_3} C_{(s)_n}, \tag{2.36}$$

with

$$\dot{\omega}_3 = k_3 \left[\frac{\rho Y_{C_{(s)}}}{M_{C_{(s)}}}\right] [N]^{11/6} \tag{2.37}$$

and

$$k_3 = 2C_a \left(\frac{6M_{C_{(s)}}}{\pi \rho_{C_{(s)}}}\right)^{1/6} \left(\frac{6k_b T}{\rho_{C_{(s)}}}\right)^{1/2}, \tag{2.38}$$

where $M_{C_{(s)}}$ is the molecular weight of carbon, C_a the constant is the agglomeration constant with the value of 9.0 suggested by Leung et al. [104] used in this work. Generally, this step reduces the soot number density. k_b is Boltzmann's constant ($1.38054 \cdot 10^{-16}\ erg/K$).

It can be observed from Equations 2.37 and 2.38 that the soot coagulation rate depends on particle number density and the temperature in each CFD computational cell.

Soot oxidation by O_2 and OH

Oxidation occurs by O_2 and OH following:

$$\begin{aligned} C_{(s)} + \frac{1}{2}O_2 &\xrightarrow{\dot{\omega}_5} CO \\ C_{(s)} + OH &\xrightarrow{\dot{\omega}_6} CO + \frac{1}{2}H_2 \end{aligned} \tag{2.39}$$

where the reaction rates of O_2 and OH oxidation are $\dot{\omega}_5$ and $\dot{\omega}_6$, respectively.

Transport equations for soot species and number density

The soot species density and soot number density are treated as passive species in the model, and their transport equations can the represented as:

$$\frac{\partial M}{\partial t} = -\nabla \cdot (M \cdot v) + \nabla \cdot \left(\frac{\mu}{SC} \cdot \nabla \left(\frac{M}{\rho}\right) + \zeta M \frac{\mu}{\rho} \frac{\nabla T}{T}\right) + \dot{S}_M, \tag{2.40}$$

where M stands for either soot species density ($Y_{C_{(s)}}$) in $[g/cm^3]$ or soot number density (N) in $[particles/cm^3]$. v is the CFD gas-phase velocity, SC is the Schmidt number, μ is the fluid viscosity, and $\dot{S}_M$ represents source terms[1]. However, in the current soot model source terms for $A_2 \sim A_4$ PAH surface growth assisted steps are also included in the soot species density source terms.

Among all steps shown above, the C_2H_2 and A_1 assisted surface growth processes have been found to be the most sensitive reactions for the soot formation process, and OH oxidation process plays a significant role in the soot oxidation process [103].

[1]Details of the source terms for both soot species density and soot number density are described by Vishwanathan [87].

Criteria for soot particle sizes calculation

The soot particles are assumed to be spherical and locally monodisperse in each computational cell, but the soot diameter can vary from one computational cell to the next. Accordingly, Jiao and Reitz [103] introduced separate criteria to calculate soot particle sizes. The primary particle number density is assumed to be $1e^{-10}$ of the regulated PN ($2.83e^{10}\,particles/cm^3$) for CARB 2017 (i.e., $2.83\,particles/cm^3$). This condition actually only occurs during the inception process of soot formation when few particles are produced. Once particle number density is higher than the proposed primary particle number density, soot particle size is then calculated based on soot mass conservation in Equation 2.34, and soot surface growth is the only pathway to increase particle size.

The aim was to avoid that particles suddenly increase from the initial nucleated particle size of 1.25 nm to the maximum particle size (500 nm) assumed in the model, and then dramatically decreases due to oxidation from OH, followed by a gradually increase resulting from the surface growth process. In the updated soot model, starting from low soot levels of particles with size of 1.25 nm and once the soot mass exceeds the criterion the soot particles increase in size gradually. After that they decrease due to soot oxidation promoted by OH presence at high temperature.

3 Preliminary Results

In this Chapter, 3-D CFD simulations of one of the four cylinders of the engine used during the Master's Thesis experimental campaign (cf. Introduction) are provided, as a first step. In particular, the numerical results were compared to Particle Size Distributions (PSDs) derived from the experimental measurements carried out in stationary conditions. In this way the influences of engine load and regime on PSD were determined and the results were helpful to provide some initial analysis on particulate formation processes and on the complex phenomena occurring in-cylinder.

3.1 Numerical set-up

Four different engine conditions were considered in order to compare soot granulometric distributions. In the experiments, exhaust samples were acquired by sampling with the DMS500 from the exhaust flow before the turbine. Size distribution taken from the cylinder at EVO obtained by using the numerical model described in Chapter 2.

The list of the stationary conditions and the more important engine settings used for each of the simulations are reported in Table 3.1. The computational mesh of the engine whose geometry is reported in Table 3.2, contains around 100,000 cells at bottom dead center (BDC) and it is shown in Figure 3.1. The spark plug is located at the center of the cylinder head. The initial in-cylinder mixture was assumed to be completely homogeneous, and the simulations started from intake valve closure (IVC) and ended at exhaust valve opening (EVO).

The numerical PSDs at the end of the simulation were compared with the experimental measurements, where the latter consisted in samples of 100 seconds, which started some seconds later when the engine reached the specific stationary condition.

The specifications for the natural gas used for the simulation are reported in Table 3.3. In the fuel modeling the two main components of the natural gas used in the experiments were considered, in conjunction with the relative amounts of nitrogen and

Table 3.1: Operating condition specifications.

Load [%]	**Engine speed** [rpm]	**Spark Advance** CA ° ATDC
0 (idle)	800	-5.0
80	2000	-18.0
	2500	-16.4
	3000	-19.0

Table 3.2: Main specification of tested CNG engine.

Name	**Units**	**Value**
Displacement	cm^3	2998 cc
Bore	mm	95.8 mm
Stroke	mm	104.0 mm
Compression ratio	None	12.5:1
IVC	CA °	24° ABDC
EVO	CA °	68° BBDC

Table 3.3: Composition of the fuel considered in the simulations.

Species	**Fraction**
CO_2	1.419
N_2	2.439
CH_4	89.304
C_2H_6	6.115

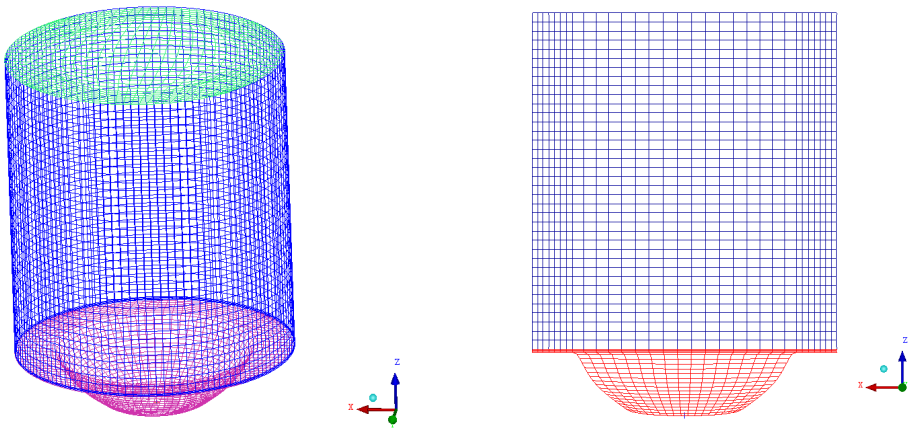

(a) **(b)**

Figure 3.1: Computational mesh of the SI engine, containing 100,000 cells at BDC. Perspective view (a); x-z section (b).

carbon dioxide. No external EGR is used on the engine. In the calculation of the initial mixture composition, a computed value of 5% of internal EGR was also considered.

3.2 Results and discussion

Figure 3.2(a) shows predicted in-cylinder pressure traces for the 4 different engine operating conditions chosen for this analysis. Unfortunately experimental measurements were not available. However, comparisons with in-cylinder preassure measurements are provided for the investigations reported in Chapter 4 and Chapter 5. In Figure 3.2(b) computed in-cylinder soot mass histories are reported for each case. From the results it is seen that soot formation dominates first and then soot oxidation begins to play an important role in the net soot emissions during the expansion stroke for all operating conditions. This trend is more evident for the lowest engine speed. Although the engine load is very low and the ignition occurs later, the soot peak for this case is comparable with the other cases. Because of the low engine speed, there is more time available for combustion and therefore for heat release, so higher temperatures (more appropriate for soot formation) are recorded before the front flame reaches the cylinder walls. However, after the entire cylinder has been swept by the flame front there is more residence time

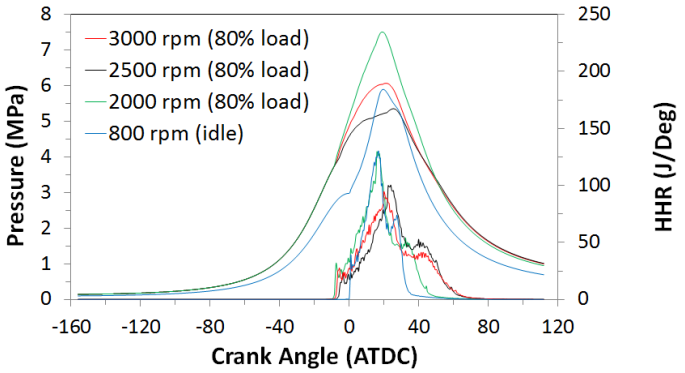

(a)

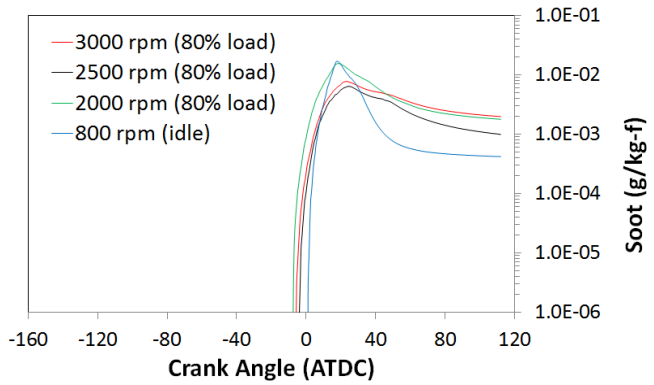

(b)

Figure 3.2: Predicted in-cylinder pressure and HHR traces (a) and soot mass evolution (b) computed for each operating condition of Table 3.3.

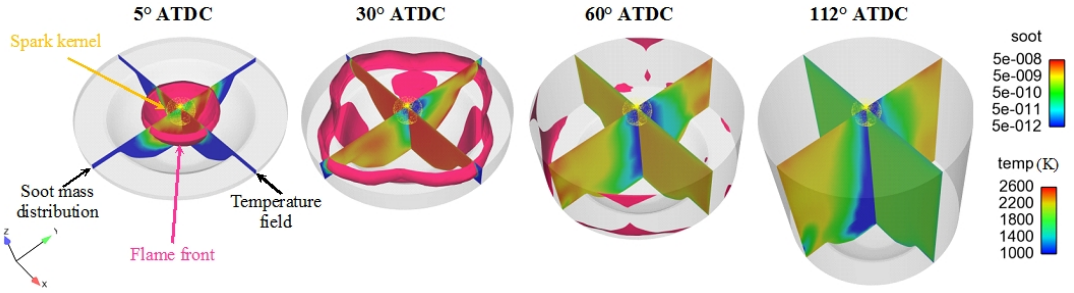

Figure 3.3: Evolution of in-cylinder temperature field (plane x-z) and soot mass fraction distribution (plane y-z) for 2500 rpm and 80% load case during the expansion stroke in the simulations. Yellow particles: spark kernel surface. Pink surface: flame front.

available to oxidize the newly formed soot, so the level of soot per kilogram of fuel at EVO crank, is almost one order of magnitude less than for the highest speed cases.

The start-of-ignition time is close for the 2000 and 3000 rpm cases, but higher values of temperature, pressure and heat released are reached at 2000 rpm due to the lower engine speed. This explains why the soot mass peak reached at 2000 rpm is higher than that calculated for 3000 rpm and why at the end of the simulations the levels are instead very close.

For the intermediate speed case of 2500 rpm, the ignition takes place later, so the soot mass peak becomes comparable with the higher speed case and then, due the more residence time available for soot oxidation, a stronger level of decrease is observed.

For this 2500 rpm and 80% load case (black line in Figure 3.2) the predicted in-cylinder distributions of temperature and soot mass fraction are shown in Figure 3.3. The simulations results are reported at four different crank angles during combustion.

In Figure 3.3 on the cut section belonging to the y-z plane the temperature field is depicted, while the soot mass fraction distribution is plotted on the cross section along the x-z plane. Yellow particles in the center are used to represent the kernel surface and the pink surface represents the flame front surface after the transition from the kernel growth model to the turbulent flame propagation model. The 3-dimensional flame front propagates radially towards cylinder wall with a quasi-spherical shape.

Higher soot mass fractions are seen near the flame front regions, where the in-cylinder temperature exceeds 2600 K after five degrees after TDC, while in the burnt regions in the center of the cylinder oxidation processes by OH radicals start to take place, and thus the soot mass fraction is reduced.

At 30° ATDC the front flame reaches the squish region. This produced the slightly more rapid pressure increased showed in Figure 10 at that crank angle for the case under investigation (black line). At this point high soot mass fractions are still detectable in the cylinder due to the high temperatures still reigning in the combustion chamber.

When the entire cylinder has been swept by the flame front the peak temperature reaches above 2400 K by 60° ATDC. The temperature is slightly lower (1900 K) near the cylinder walls due to wall heat transfer. The soot mass fraction decreases after this crank angle, since sufficient residence time at high temperatures is available for oxidation due to OH and since the flame front that produces the species responsible for soot inception and soot surface growth has reached the cylinder walls, and none of

those species are available. Soot is mainly found near the cylinder walls because of less residence time at sufficient high temperature available for oxidization of newly formed soot in previous flame front regions and due to the lack of species for soot inception and surface growth.

The in-cylinder temperature then continuously decreases to a temperature of less than 1800 K, which is reached at 112° ATDC when exhaust valve is opened. These conditions are not appropriate for soot formation. The temperature near the walls is even lower, around 1400 K and is not appropriate for both soot formation and oxidation. It is also found that soot left near the walls has also been notably reduced, and negligible soot is left in the center of the cylinder.

It was of interest to compare the PSDs between the experimental data and the simulations. In the experiments, the engine-out exhaust sample was taken from the exhaust stream upstream the turbine, via the DMS500. The measurements consisted of samples of 100 seconds and started some seconds later when the engine reached the specific stationary condition.

Number weighted PSD functions calculated in-cylinder at 112° ATDC (at EVO) were taken from the simulations for comparison to the corresponding measurements in the engine exhaust and the comparison is plotted in Figure 3.4.

The 95% confidence intervals for each empirical measurement are also made available. In the experiments, the PSDs show similar trends for the three high load conditions as the graphs (b), (c) and (d) of Figure 3.4 report: a predomination of particles having a dimension between 50 and 100 nm (accumulation mode) is observable; for particle sizes larger than 100 nm the Particle Number (PN) starts to consistently decrease with particle size increase; whereas the number of particles with dimensions lower that 50 nm (nucleation mode) remains noticeable, though lower than the number of the smallest particles attributable to the accumulation mode.

When the engine is idling it was seen that the PN decreases in comparison to higher load conditions, with a slight tendency to reduce with increased size. That highlights the increasing importance of the accumulation mode with engine load and speed. This trend was already pointed out when the granulometric distribution reported in Figure 8 was discussed.

Numerical results for cases (b), (c) and (d) of Figure 3.4 seem to well capture the trend detected for the particles falling in the accumulation mode, while the calculated values greatly exceed the measured ones for particles with an equivalent diameter smaller than 50 nm.

In the case (a) of Figure 3.4, the PN is generally overestimated by the numerical model. However the behavior of the PSD in response to an increase of load and speed is captured by the model.

It is necessary to underline that we are comparing experimental data from the exhaust pipe with in-cylinder quantities computed by the simulation at exhaust valve opening. Therefore oxidation that could occur in the exhaust, as well as physical soot transformation, i.e., due to the discharge process of the gasses from the combustion chamber to the exhaust pipe, or due to temperature conditions changing along the exhaust line or within the instrument sample probe are not considered. These have strong effect on nucleation mode particles that can be detected by the DMS500. It

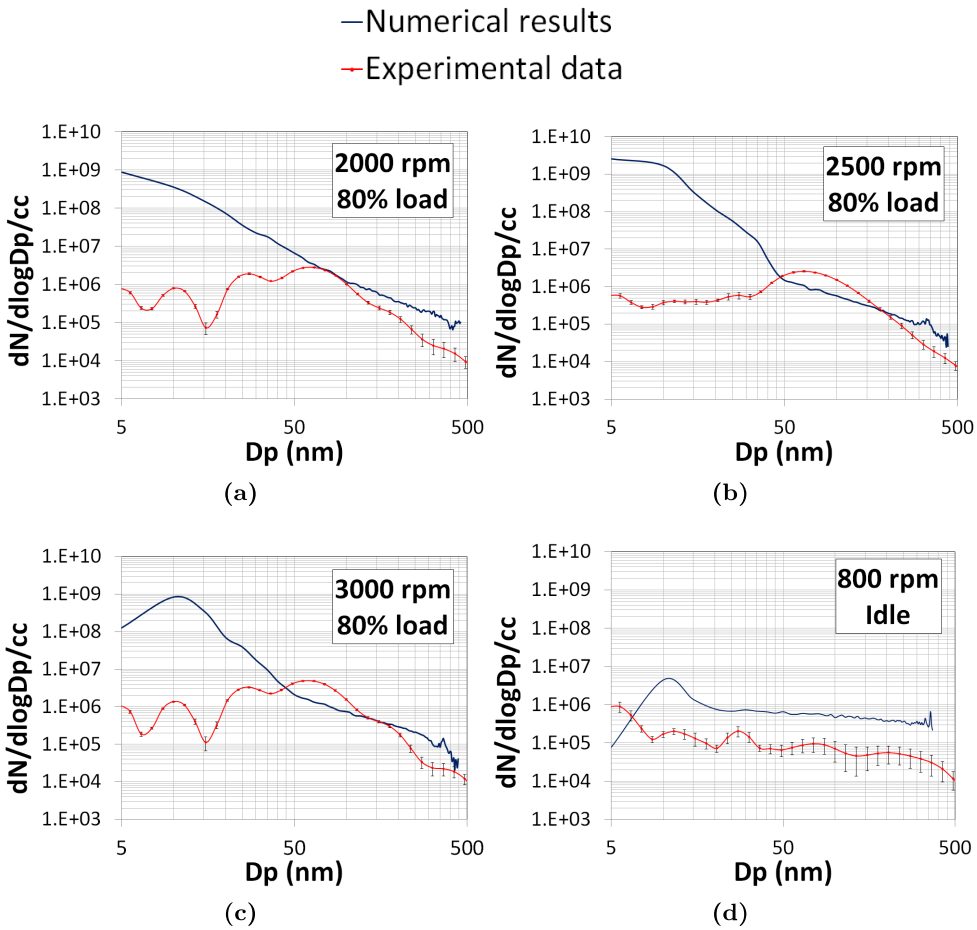

Figure 3.4: PSDs measured and computed, for each operating condition.

is well known how hard it is correctly capture particle physics below certain particle sizes. For these reasons for the future studies it is planned to use a more accurate engine mesh which includes both intake and exhaust pipes. This should provide more confidence in the comparison between experiments and simulations, allowing more accurate consideration about the performance of the numerical model.

Figure 3.5 displays the total PN per kWh within the cylinder at the end of each simulation, compared with calculated values obtained from experimental measurements for each engine operating condition. In Figures 3.5(b) and 3.5(c) is also reported the corresponding percentage composition in terms of nucleation (particle with size between 5 and 50 nm) and accumulation mode (particle with size between 50 and 500 nm), respectively, for the numerical simulations and experiments.

Figure 3.6 depicts the mass of soot per kilogram of fuel obtained from simulations in comparison with the values derived by calculation of mass from experimental number-size spectra, by using the standard "spherical calibration" of the sampler device and assuming unit density, as recommended by the DMS500 manufacture.

In each case the experimentally derived value of the particle mass is higher than the numerical simulation prediction. It may imply that other possible sources could affect soot formation besides the fuel combustion.

From the PN global trend, shown in Figure 3.5, it is possible to see that the high load and speed engine conditions produce a larger amount of particles per kWh in comparison with the number of particles detectable when the engine operates at idle. This was confirmed by both the experimental measurements and numerical simulations.

From Figure 3.4 it was seen that the numerical model overestimates the number of nucleation mode particles and this helps to explain the differences between the predicted and measured PN values. In particular, from Figures 3.5(b) and 3.5(c), it is seen that the numerical PN in high load and speed operating conditions is practically totally composed by only nucleation mode particles. This because although the accumulation

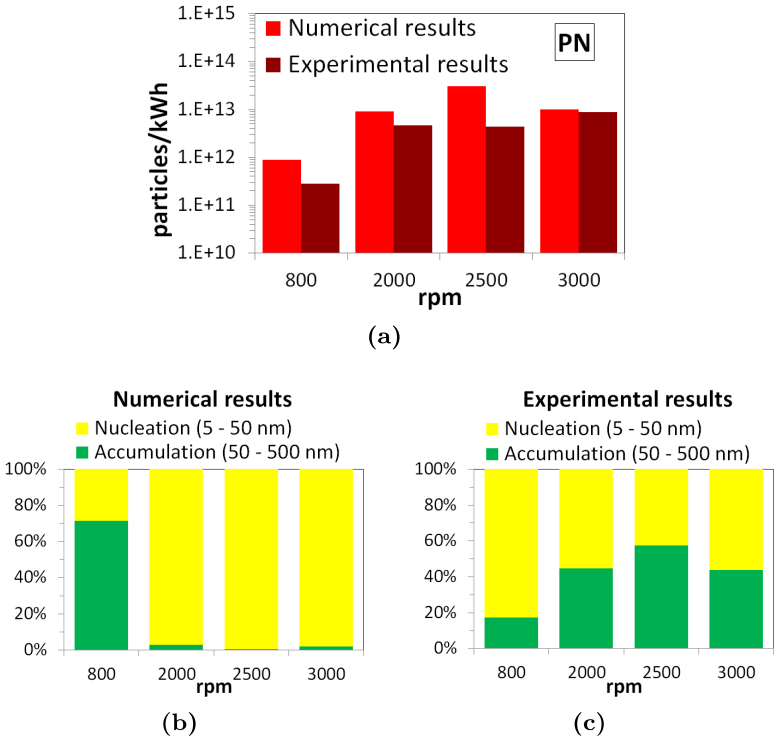

Figure 3.5: Measured and predicted PN per kWh (a) with corresponding percentage composition in terms of nucleation and accumulation mode detectable in simulations (b) and in experiments (c), for each operating condition.

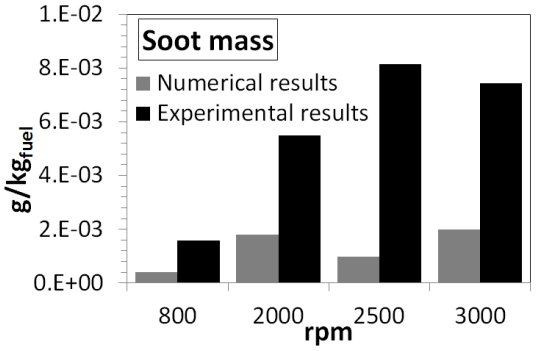

Figure 3.6: Soot mass per kilogram fuel from simulations and experiments for each operating condition.

mode levels are comparable with the corresponding empirically measured values, the number of nucleation particles computed by the simulation overtakes the experimental values by three orders of magnitude.

It is also interesting to notice that for the 2500 rpm case the experimentally recorded PN is very similar to the 2000 rpm case, but the soot mass value per kilogram of fuel is higher for 2000 rpm. This can be explained by examining the composition of the particles: at 2500 rpm a higher accumulation mode fraction was measured and since a spherical shape of particles in the DMS500 "spherical calibration" is assumed, more mass in calculated for this case. This last observation underlines once again that the nucleation mode particles influence is weak on soot mass, but is strong on PN.

3.3 Conclusions

In this preliminary Chapter, 3-D Computational Fluid Dynamics (CFD) simulations helped to explain the reasons for the observed soot PSDs measured in the experimental campaign carried out during the Master's Thesis work, in which, as previously reported in the Introduction an EURO-VI, heavy-duty, stoichiometric SI engine fueled with compressed natural gas was tested.

Four different stationary operative conditions were used to compare the measurement results with 3-D Computational Fluid Dynamics (CFD) simulations of one of the four engine cylinders. The simulations generally depicted a realistic phenomenological scenario of the soot formation and evolution as a function of the operating conditions.

It was noted that before the flame front reaches the cylinder walls, soot is mainly produced within the flame region, and soot residing in the burnt regions is reduced with sufficient residence time at high temperatures by oxidation. Soot oxidation was favored when the flame front reached the cylinder walls and no more species for soot inception and surface growth were left after the combustion. Therefore, in the center of the cylinder where the local temperatures are high enough, stronger oxidization due to high OH concentration was seen. To the same way, high soot levels were observed near the cylinder walls because of the shorter residence time and lower temperature.

Computational results concerning PSD functions are compared with the measured at the exhaust by the DMS500, for the same engine and fuel. In the experiments, at high load, a predomination of particles having a dimensions between 50 and 100 nm (accumulation mode) was observable. For particle sizes larger than 100 nm the PN started to consistently decrease with increased particle size. Although the number of particles with dimensions lower that 50 nm (nucleation mode) was noticeable, they were lower than the number of the smallest particles attributable to the accumulation mode.

When the engine was run at idle it was seen that the PN generally decreased in comparison to higher load conditions, with a slight tendency to reduce with size increase. This highlights the rising importance of the accumulation mode with engine load and speed.

At high load the model well captured the trend detected for the particles falling in the accumulation mode. However, the number of particles within the range 5-50 nm

was higher than that detected in the engine exhaust. At idle both the nucleation and accumulation PN was overestimated by numerical model.

The model demonstrated sensitivity to the variation of operating conditions in qualitative agreement with corresponding calculations from measured variables. Considering that further oxidation as well as physical soot transformations could occur in the exhaust pipes the agreement was considered to be satisfactory.

The predicted soot particle mass was lower than the experimentally derived value. This suggests that other possible sources which can affect soot formation need to be taken into consideration as well as fuel combustion.

Laminar Flame Speed Correlations for Spark-Ignition Engine Simulations

4

As already observed in Section 2.2, the laminar flame speed plays an important role for the reliability of many multidimensional combustion models for spark-ignition engines simulations is represented by the laminar flame speed estimation, which is essential for the accurate prediction of the turbulent burning velocity of the fuel-air mixture [11, 69, 90, 94, 105] and, hence, for an adequate representation of the whole combustion process taking place within the engine. Analytical correlations that allow it to be calculated have been developed, and are used in engine simulations. They are usually preferred to detailed chemical kinetic models for saving computational time. Therefore, an accurate as possible formulation for such expressions is needed for successful simulations. However, many previous empirical correlations have been based on a limited set of experimental measurements, often carried out over a limited range of operating conditions and still they need to be validated against other experimental data. In this study, measurements of laminar flame speeds obtained by several workers are collected, compared and critically analyzed with the aim to develop more accurate empirical correlations for laminar flame speeds as a function of equivalence ratio and unburned mixture temperature and pressure over a wide range of operating conditions, namely $\phi = 0.6 \div 1.7$, $p_u = 1 \div 50$ atm and $T_u = 298 \div 800$ K. The purpose is to provide simple and workable expressions for modeling the laminar flame speed of practical fuels used in spark-ignition engines. Pure compounds, such as methane and propane and binary mixtures of methane/ethane and methane/propane, as well as more complex fuels including natural gas and gasoline are considered. A comparison with available empirical correlations in literature is also provided.

4.1 Introduction

Flame propagation in spark-ignition engines involves time and spatial scales which cannot be typically captured with practical finite volume methods [69, 90, 106]. There-

fore, several dedicated numerical models have been implemented to evaluate the turbulent burning velocity once the spark has been triggered [107–109]. These models rely on empirical or semi-empirical correlations of laminar flame speeds which are derived from experimental measurements [69, 105, 110].

Several combustion phenomena depend on the laminar flame speed, such as the turbulent flame structure and speed, various modes of flame front instabilities, flame extinction through heat loss and stretch and flame stabilization [111]. In addition to engine applications, it plays a primary role in many other combustion applications, such as in the design of burners and in the prediction of explosions [107, 109]. For these reasons, it has long been the subject of extensive experimental and theoretical investigation, over a wide range of operating conditions [111].

In an internal combustion engine the laminar burning velocity influences the ignition delay, which affects the spark advance and cycle-to-cycle fluctuations, the thickness of wall quench layers (which are the primary source of unburned hydrocarbons), as well as the minimum energy to ignite the charge, which affects the range of equivalence ratio over which an engine can operate [112].

The laminar flame speed is an intrinsic property that is a function of the unburnt mixture composition, temperature, and pressure. Although encouraging progress has been made in developing detailed chemical kinetic models for its prediction, such models are still extremely complex and require significant computational effort for solving the mass, species and energy conservation equations coupled with chemistry [69, 113]. In addition, they can fail outside the range in which they have been validated against experimental data, or if the grid resolution chosen for the simulation is not appropriate for the specific case [114].

Thus, analytical correlations of the laminar flame speeds as a function of equivalence ratio, pressure and temperature are preferred in engine practical simulations. Moreover, they are more easily implemented in CFD codes than tabulated data. Their use in spark-ignition engine simulations still allows the use of detailed chemical kinetics for modeling the post-flame chemistry and the end-gas chemistry, which does not require high resolution, thus saving computational time [69, 90, 106].

In order that an analytical formulation (as well as a chemical kinetics mechanism) can be considered reliable for many possible conditions, it must be validated against a large body of data. Thus, in this work, experimental measurements of laminar flame speeds, carried out by several workers are compared and critically evaluated. Furthermore, attention is also focused on recent experimental studies. As Ranzi et al. [111] pointed out when summarized the experimental laminar burning velocities of methane/air mixtures for the previous sixty years, it was not until the mid-1980s that Wu and Law [115] noted the importance of the stretch effects in the experimental determination of laminar flame speeds and proposed a rational approach towards their elimination. In addition, published predictions of empirical correlations derived by other workers have also been considered and compared with those proposed in this work for a more exhaustive analysis.

In the present study, empirical correlations are presented for laminar flame speeds as functions of equivalence ratio and unburned mixture temperature and pressure over a wide range of operating conditions. The fuels considered include promising cleaner

alternatives to gasoline for the future, including natural gas. However, since pure compounds represent a good starting point, correlations for methane and propane are also provided. Then, together with natural gas, binary mixtures of methane/ethane and methane/propane are also considered. Finally, an empirical correlation for gasoline is provided too. The aim is to offer a simple, but accurate method for determining the laminar burning velocity for a wide range of equivalence ratios, temperatures and pressures that it is suitable for engine simulation applications.

4.2 Overview of empirical correlations available in literature

In the last sixty years, various forms of empirical and semi-empirical functional relationships have been proposed for the laminar burning velocity. These semi-empirical relationships are based either on the thermal flame propagation theory of Zel'dovich/Frank-Kamenetsky/Semenov [64, 112, 116–121] or on the active species diffusion theory [122–125]. Wholly empirical correlations are instead exclusively derived from the interpolation of experimental measurements within the operating range over which they were carried out.

The "Arrhenius form", upon which many semi-empirical formulations are based, is very sensitive to the adiabatic flame temperature, which is in turn sensitive to the thermodynamic model used to calculate it [64]. In addition, it seems that the Arrhenius parameters do not depend consistently on the equivalence ratio, but rather they vary erratically with it [64]. As a consequence, sometimes the interpolation and extrapolation process can be very difficult, with a possible inability to produce smooth variations with equivalence ratio or temperature [64, 110].

The simplest alternative and the most widely used form of the wholly empirical correlation is the so-called "power law" formula, adopted by many Investigators [22, 64, 110, 112–114, 119, 126–131]:

$$S_L\left(\phi, T_u, p_u\right) = \; S_{L0}\left(\frac{T_u}{T_0}\right)^{\alpha}\left(\frac{p_u}{p_0}\right)^{\beta}, \tag{4.1}$$

where S_{L0} is the velocity measured at $T_u = T_0$ and $p_u = p_0$ for a given equivalence ratio ϕ, and α and β are constants or mixture strength-dependent terms.

One of the most known studies in which such a form was employed is the work by Metghalchi et al. [64]. It was derived from measurements carried out in a constant volume vessel for fuel-air equivalence ratios $\varphi = 0.8 \div 1.5$, over pressure and temperature ranges of $p_u = 0.4 \; \div 50 \; atm$ and $T_u = 298 \; \div 750 \; K$. After testing their correlation against experimental measurements of the laminar burning velocity of methanol, propane, isooctane and indolene they concluded that the temperature and pressure exponents α and β were independent of fuel type within their estimated experimental error and could be represented by the expressions:

$$\begin{aligned} \alpha\left(\phi\right) &= 2.18 - 0.8(\phi - 1) \\ \beta\left(\phi\right) &= 0.16 \; + \; 0.22\left(\phi - 1\right). \end{aligned} \tag{4.2}$$

Table 4.1: Coefficients of Equation (4.3) proposed by Metghalchi et al. [64] for propane/air mixtures.

Fuel	**T** [**K**]	**p** [**atm**]	$\boldsymbol{\Phi_m}$	$\boldsymbol{B_m}$ [**cm/s**]	$\boldsymbol{B_2}$ [**cm/s**]
C_3H_8	298	1	1.08	34.22	-138.65
	$350 \div 700$	$1 \div 50$	1.08	40.11	-186.48

In addition, they found that the reference velocities S_{L0} were a weak function of fuel type and could be fit by a second-order polynomial of the form:

$$S_{L0}(\phi) = B_m + B_2(\phi - \phi_m)^2. \tag{4.3}$$

where the parameters B_m, B_2 and ϕ_m are given in Table 4.1 for propane, which is also of interest in the present study. In Equation (6.1) they considered $p_0 = 1\ atm$ and $T_0 = 298\ K$, and recommended expressions for application in the ranges: $p_u = 1 \div 50\ atm$ and $T_u = 350 \div 700\ K$. However, at room temperature that interpolation underestimated burning velocities. Therefore, they proposed different and more appropriate values for coefficients B_m and B_2 for room conditions, which are reported as well in Table 4.1.

Beside the fact that two sets of coefficients must be provided for each fuel, another major limitation is that Equation (6.2) predicts negative flame speeds for very lean or very rich mixtures. It is acceptable for simulations of premixed flames near stoichiometric conditions, but is not applicable for stratified charge combustion in direct injection spark-ignition engines with gasoline or gaseous fuels, i.e., natural gas [5, 132–134].

An alternative formulation for evaluating the term $S_{L0}(\phi)$ of Equation (6.1) was derived by Elia et al. [127]. They developed a correlation by fitting their experimental data of the laminar burning velocity of methane/air mixtures, obtained using a spherical constant volume combustion vessel with fuel-to-air ratio varying from 0.8 to 1.2, as:

$$S_{L0}(\phi) = S_{u0}\left(\alpha_0 + \alpha_1\phi + \alpha_2\phi^2\right), \tag{4.4}$$

where $S_{u0} = 37.5 cm/s$, $\alpha_0 = -5.883$, $\alpha_1 = 14.003$, $\alpha_2 = -7.115$. In the same study, after analyzing measurements in which the unburned gas pressure was varied from 0.75 to 70 atm and the temperature from 298 to 550 K, they suggested the use of a fixed value for the coefficients α and β, namely 1.857 and -0.435, respectively. The results appeared to be in good agreement with their experimental data, but some discrepancies with other works have been recorded. In addition, it is widely recognized that the exponents α and β vary with equivalence ratio and a possible dependence on pressure and the temperature could exist too [110, 128, 135, 136]. Therefore, for a more appropriate formulation, expressions for α and β, at least as functions of only ϕ, are also needed. Furthermore, the correlation proposed by Elia et al. [127] for S_{L0} shows a problem similar to that highlighted for Metghalchi et al. [64] regarding the generation of negative values outside the tested equivalence ratio range.

Another work in which the power law formulation was employed coming from measurements of laminar spherical expanding flames of methane/air mixtures is the

Table 4.2: Coefficients for Equation (6.1) by Gu et al. [119] for methane/air mixtures in the ranges of 300÷400 K and 1÷10 atm for three different equivalence ratios, namely Φ =0.8,1.0 and 1.2.

ϕ	S_{u0}[cm/s]	α	β
0.8	25.9	2.105	-0.504
1.0	36.0	1.612	-0.374
1.2	31.4	2.000	-0.438

work carried out by Gu et al. [119], where reference values of $p_0 = 1\ atm$ and $T_0 = 300\ K$ were also assumed. What the authors of this study suggested were three expressions for Equation (6.1) in which the parameters S_{u0}, α and β were optimized in the ranges of $300 \div 400\ K$ and $1 \div 10\ atm$ for three different equivalence ratios, namely $\phi = 0.8,\ \ 1.0$ and 1.2. The values that they proposed are reported in Table 4.2.

Other researchers developed correlations for stochiometric mixtures, including Han et al. [128] and more recently Hu et al. [113]. The first [128] used a preheated cylindrical combustion chamber to measure the laminar burning velocity of methane/air mixtures in the range of initial temperatures from 298 K to 498 K and initial pressures from 1 atm to 5 atm. The derived empirical formulation was:

$$S_L = \ 36.11\left(\frac{T_u}{T_0}\right)^{\alpha}\left(\frac{p_u}{p_0}\right)^{-0.37}, \tag{4.5}$$

Where $p_0 = 1\ atm$ and $T_0 = 300\ K$ and the temperature exponent α depends on pressure as:

$$\alpha\left(p_u\right) = 1.5365 + 0.1165 p_u. \tag{4.6}$$

Hu et al. [113] quantified the laminar flame speed dependence upon pressure and temperature as:

$$\begin{aligned} S_L\left(p_u\right) &= \ 0.133(p_u)^{-0.461}, \quad T_u = 300\ K, \quad 1\ atm \leq p_u \leq 60\ atm \\ S_L\left(T_u\right) &= \ 325e^{\left(-\frac{9439}{T_u+1089}\right)}, \quad p_u = 1\ atm, \quad 300\ K \leq T_u \leq 700\ K. \end{aligned} \tag{4.7}$$

In addition, they found that the exponent α increased linearly with increase of initial temperature, while the exponent β decreased exponentially whit increase of initial pressure. Consequently, they formulated the follows correlations for the two exponents, as:

$$\begin{aligned} \alpha\left(T_u\right) &= 1.39 + 0.0006 T_u, \quad 300\ K \ \leq \ T_u \leq 700\ K \\ \beta\left(p_u\right) &= 0.226e^{-\frac{p_u}{0.841}} - 0.511, 1atm \leq p_u \leq 60\ atm. \end{aligned} \tag{4.8}$$

The last expressions were validated by Hu et al. [113] at high temperatures and pressures by comparison with numerical simulations.

A similar strategy was adopted by Ouimette et al. [129] who calculated numerically the laminar flame speed for both methane and a synthetic gas using PREMIX. For both fuels, they provided a correlation in the form of Equation (6.1) exclusively based on the

Table 4.3: Coefficients for Gülder's exponential formulation for different fuels.

Authors	**Year**	**Ref.**	**Fuel**	Z	W $[cm/s]$	η	ξ	σ
Gülder	1984	[110]	CH_4	1	42.2	0.15	5.18	1.075
			C_3H_8	1	44.6	0.12	4.95	1.075
Dirrenberger et al.	2011	[22]	CH_4	1	38.638	-0.15	6.2706	1.1
			C_3H_8	1	42.2012	-0.3104	5.1455	1.1
Coppens et al.	2007	[137]	CH_4	1	39.0542	-0.4333	6.0157	1.1

calculations. Although the calculations were performed at different equivalence ratios and pressures and the explored range of the initial mixture temperatures is the largest available in literature ($300 \div 850\ K$), the technique used for the numerical simulations was validated by means of comparisons with experimental data for methane only for the room pressure case and for two different unburnt temperatures, namely 300 and 400 K. The following expressions for calculating methane's laminar flame speed, based on work by Liao et al. [130] (which is discussed later in this section) was suggested:

$$\begin{aligned} S_{L0}(\phi) &= -204.6\phi^3 + 428.9\phi^2 - 220.2\phi + 33.3 \\ \alpha(\phi) &= 4.3\phi^2 - 9.0\phi + 6.6 \\ \beta(\phi) &= -0.7\phi^2 + 1.4\phi - 1.1 \end{aligned} \tag{4.9}$$

A completely different approach for determining the term $S_{L0}(\phi)$ in Equation (6.1), which represents a practical solution to the intrinsic problem of polynomial forms, was proposed by Gülder [110], who chose the following empirical expression to represent the room temperature burning velocity of methane, propane and other fuels considered in his work:

$$S_{L0}(\phi) = Z\ W\ \phi^{\eta}\ e^{-\xi(\phi-\sigma)^2}, \tag{4.10}$$

where W, η and ξ are constants for a given fuel, and $Z = 1$ for single constituent fuels. The constants for methane/air and propane/air mixtures proposed in [110] are listed in Table 4.3. In such work, the power law dependence of the laminar burning velocity on the unburnt mixture pressure and temperature was used, but a practical analytical expression for the exponents α and β, as functions of the equivalence ratio, was not proposed. Instead, constant values for α and β were proposed, namely, respectively, 2 and -0.5 for methane and 1.77 and -0.2 for propane.

Gülder's formulation for the evaluation of S_{L0} has also been adopted in the correlations proposed in the present work, since it appears to be the most promising expression among all the analyzed solutions. The power law formula is then chosen for taking into account the influence of pressure and temperature.

Recently, Dirrenberger et al. [22] adopted such a formulation for the prediction of the laminar flame velocity of the components of natural gas, methane, ethane, propane and n-butane, as well as for binary and tertiary mixtures of these compounds, which had been proposed as surrogates for natural gas. In that study, the measurements

were performed by using the heat flux method at atmospheric conditions. The mixture strength covered the largest range available in literature, namely from 0.6 to 2.1. The values of the parameters that they proposed for pure methane and propane are given in Table 4.3. For the methane case their parameters were far from those previously proposed by Gülder, are but very close to those found by other researchers, i.e., Coppens et al. [40], which are reported as well in Table 4.3. They proposed a correlation valid for a natural gas surrogate mixture of methane, ethane and propane. This ternary mixture correlation was a combination of the expressions obtained for binary methane/ethane and methane/propane mixtures, which used the correlation, derived from Coppens et al. [137]:

$$S_{L0}(\phi,\chi) = (1+\nu\chi^{\tau})\ W\ \phi^{\eta}\ e^{-\xi(\phi-\sigma-\Omega\chi)^2}. \tag{4.11}$$

The term Z, present in Gülder's formulation (Equation (4.10)), assumes the value $(1+\nu\chi^{\tau})$ to take into account the presence of other compounds in methane. χ is the amount of the other gas in the fuel mixture. The additional term $\Omega\chi$ in the exponent, allows to reproduce the shift of the maximum of the laminar flame velocity's dependence with the additional gas concentration. When χ is zero, the original Gülder's formulation for pure compounds is obtained. The coefficients ν, τ, and Ω derived from the experimental data interpolation are reported in Table 4.4. Good agreement was found for lean and rich mixtures, but the correlation overestimated flame velocities near stoichiometry.

By combining these results, they formulated the following correlation for ternary mixtures:

$$S_{L0}(\phi,\chi_1,\chi_2) = (1+\nu_1\chi_1^{\tau_1})(1+\nu_2\chi_2^{\tau_2})\ W\ \phi^{\eta}\ e^{-\xi(\phi-\sigma-\Omega_1\chi_1-\Omega_2\chi_2)^2}, \tag{4.12}$$

where the subscript 1 refers to parameters calculated for one component, i.e. ethane, and subscript 2 to the other one, i.e., propane. Once again, if $\chi_1 = \chi_2 = 0$ the correlation for pure fuels is obtained. If either $\chi_1 = 0$ or $\chi_2 = 0$, then the previous binary mixtures formulation is derived.

Liao et al. [130] studied the dependence of the exponents α and β upon the equivalence ratio of a Chinese Natural Gas (from the north of Shannxi Province), when the mixture strength was varied from 0.6 to 1.4, in the case of spherically expanding flames of natural gas/air mixtures. Initial pressures of 0.05, 0.1 and 0.15 MPa, and preheat temperatures ranging from 300 to 400 K were considered. They proposed the following second-order polynomial form:

$$\alpha(\phi) = 5.75\phi^2 - 12.15\phi + 7.98\beta(\phi) = -0.905\phi^2 + 2\phi - 1.473. \tag{4.13}$$

A simple third-order polynomial expression was used to fit their data at ambient conditions ($T_u = T_0 = 300\ K$ and $p_u = p_0 = 1atm$), namely

$$S_{L0}(\phi) = -177.43\phi^3 + 340.77\phi^2 - 123.66\phi - 0.2297, \tag{4.14}$$

which does not consider the influence of the natural gas composition, since was not varied during the tests.

Table 4.4: Coefficients proposed by Dirrenberger et al. [22] for binary mixtures.

Fuel	ν	τ	Ω
CH_4/ C_2H_6	0.2103	0.545	-0.0191
CH_4/ C_3H_8	0.2129	0.8312	-0.0439

The expressions provided by Liao et al. [130] for the exponentials α and β appear to be the most convincing among the forms analyzed so far, since they can well reproduce influence of pressure and temperature on the lean and rich sides, in comparison to the stochiometric case. This is appreciable from Figure 4.1, in which the various solutions proposed for the calculation of α and β developed by Metghalchi et al. [64], Gu et al. [119] and Liao et al. [130] are compared. The results by Gu et al. [119] and Liao et al. [130] look very close to each other (the natural gas investigated by Liao et al. [130] was composed of 96.16% of methane).

Metghalchi et al.'s expression [64] was derived for propane and therefore, no direct comparisons can be done with the other two. However, the expression proposed by Metghalchi et al. [64] has a linear form, since it was derived by considering only three different equivalence ratios near stoichiometric conditions. Thus, the temperature influence is overestimated for rich and lean mixtures and underestimated for near-stochiometric conditions (Figure 4.1(a)). For the same reason, the opposite is true for the pressure influence (Figure 4.1(b)).

The laminar burning velocity of gasoline, similarly to natural gas, has not been investigated as extensively as other pure compounds. Gasoline is a complex fuel mixture, with large variations in compositions between different commercial gasolines. As result, there is no fixed laminar burning velocity. This also explains why it is currently not possible to represent the complex chemistry of gasoline in a chemical kinetic model and surrogates are usually used [114, 138]. However, Sileghem et al. [114] recently measured the laminar burning velocities for a gasoline (Exxon 708629-60) using the heat flux method on a flat flame adiabatic burner and they found good agreement both with the data of Dirrenberger et al. [139], who used the same method to measure the laminar

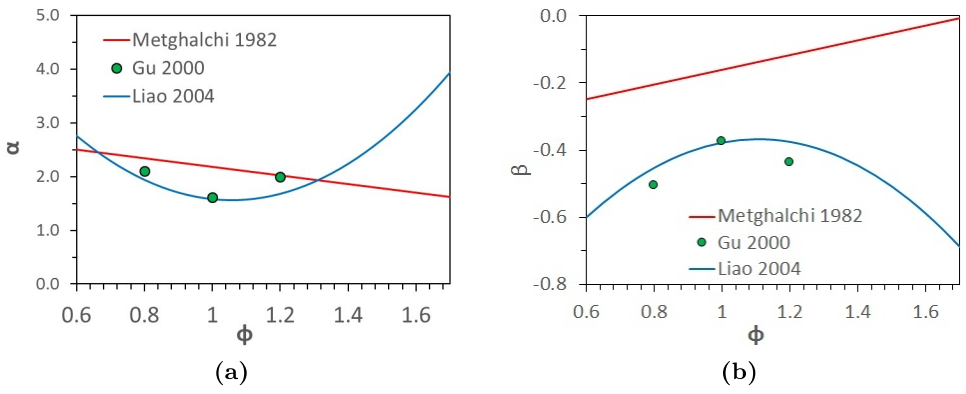

Figure 4.1: Dependence of exponents α and β upon equivalence ratio ϕ.

burning velocity, and with Zhao et al. [140] (at 353 K) who used the stagnation jet-wall flame configuration and Particle Image Velocimetry.

In the same study, the temperature dependence of the laminar burning velocity was also shown for gasoline, for equivalence ratios varying from 0.7 to 1.3 and for temperatures between 298 K and 358 K. The temperature dependence of gasoline was compared to the empirical formulations by Gülder [110] and Metghalchi et al. [64] and a correlation implemented in GT-Power based on the publication by Takashi et al. [141]. The result was that none of the correlations captured the temperature dependence of gasoline. A second-order polynomial, as in Liao et al. [130] (Equation (4.13)) was then suggested to represent the power exponent α:

$$\alpha(\phi) = 3.28\phi^2 - 7.52\phi + 5.93. \tag{4.15}$$

Unfortunately, no correlation for $S_{L0}(\phi)$, or for pressure dependence was provided. Experimental measurements of laminar flame speeds obtained by various workers are compared and analyzed next for each of the fuels considered in this study. A comparison with the above discussed empirical correlations is then reported.

4.3 Results and comparisons

The empirical correlations developed for pure methane and propane, methane/ethane and methane propane mixtures, as well as for natural gas and gasoline are discussed next.

Results for the considered studies are listed in tables, together with the method that was used, the range of the equivalence ratios, pressures and temperatures that were explored, and the fuels that were considered in the specific study.

As previously mentioned, all the correlations proposed in this work have the "power law" form of Equation (6.1), with $p_0 = 1\ atm$ and $T_0 = 298\ K$. For all the fuels considered, the $S_{L0}(\phi)$ term is represented by using the "Gülder's exponential formulation" of Equation (4.10), while the exponents α and β were considered to be functions of the mixture strength ϕ and the second-order polynomial fitting proposed by Liao et al. [130] (Equation (4.13)) is considered:

$$\begin{aligned} \alpha(\phi) &= a_2\phi^2 - a_1\phi + a_0 \\ \beta(\phi) &= -b_2\phi^2 + b_1\phi - b_0. \end{aligned} \tag{4.16}$$

Methane

Methane is often considered as a reference gas for combustion studies and it has been studied for a large range of conditions. However, the data start to become scarce at high pressures and temperatures, due to experimental difficulties.

The literature experiments and empirical correlations for methane are listed in Table 4.5. Figure 4.2 shows the results of curve fitting for the methane laminar flame speed at 1 atm and 298 K, for equivalence ratio ranging from 0.6 to 1.7. The black solid line represents $S_{L0}(\phi)$ when the coefficients proposed in Table 4.6 are adopted.

Figure 4.2 also compares with other empirical correlations. Gülder [110] ad Dirrenberger et al. [22] used the same form that is considered in the present study (Equation (4.10)), but with different coefficients (listed in Table 4.3). The correlation proposed by Elia et al. [127] (Equation (4.4)) does not reproduce the trend in a satisfactory way, while that proposed by Ouimette et al. [129] (Equation (4.9)) is closer to the best fit, although it overestimates the flame speed on the rich side and does not follow the trend for equivalence ratios larger than 1.3 (above 1.4 it gives negative results, which must be avoided).

Figure 4.3 summarizes pressure effects over the range of equivalence ratios considered. The obtained coefficients for the exponents α and β in Equation (4.16) are listed in Table 4.7. Figure 4.3(a) shows good agreement with the various experiments and with pressures ranging from 1 to 20 atm. Figures 4.3(a) and 4.3(b) depict the above-mentioned limitations shown by Elia and Ouimette's correlations. In addition, the latter overestimates the laminar burning velocity for all equivalence ratios at higher pressures.

Figure 4.4(a) summarizes the effect of the pressure for the stochiometric case. In this case it was also possible to compare the result with the correlations proposed by Han et al. [29] (Equations (4.5) and (4.6)), Gu et al. [19] (Table 4.2) and Hu et al. [113] (Equations (4.8) and (4.9)). The results appear to be close for ambient temperature conditions. Han, Gu and Ouimette's correlations underestimate the pressure influence, while Hu's correlation overestimates it in the low-pressure range. More problems arise when the correlations are compared with available data at higher initial temperatures. Han's correlation is not able to match the trend anymore, while Ouimette's formulation produces too high values at all considered initial pressures and highlights the limits of a correlation exclusively based on numerical results. Elia's correlation shows good agreement with their own data, but some discrepancies with other experiments start to appear.

In Figure 4.4(b) results for the case of $\phi = 1.2$ are shown. This case is one of the most studied at high pressure, as can be inferred from Table 4.5. Analogous conclusions to those derived for the stochiometric case regarding the correlations proposed by Gu and Ouimette, can be made and Elia's correlation produces too low values at lower pressures.

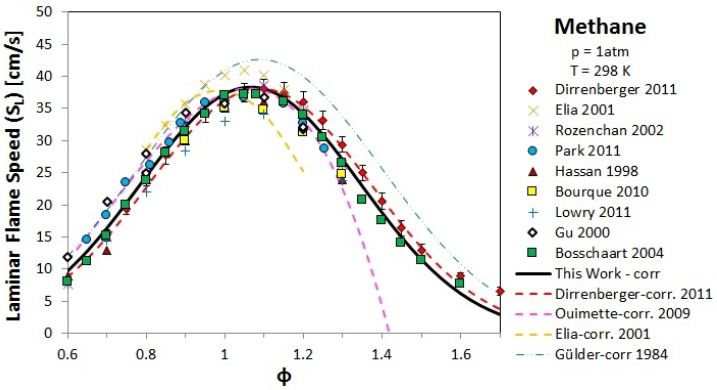

Figure 4.2: Methane laminar flame speed at room conditions. Marks: experimental data; dashed lines: correlations available in literature; solid line: empirical correlation proposed in this work

Table 4.5: Literature considered for methane.

Ref.	Authors	Year	Fuels	Φ	T_u [K]	p_u [atm]	Method
[117]	Ryan	1980	Methane, n-Heptane, Methanol and Propane	0.8-1	470-570	1-20	Constant-volume bomb
[110]	Gülder	1984	Methane, Propane, Isooctane, Methanol, Ethanol, Alcohol/Isooctane and Alcohol/water	0.7-1.4	298-800	1-20	Constant-volume bomb, Correlations / Correlations
[142]	Hassan	1998	Methane	0.6-1.35	298	0.5-4	Outwardly spherical bomb
[119]	Gu	2000	Methane	0.8, 1 and 1.2	300-400	1-10	Constant-pressure spherical comb. chamber / Correlations
[127]	Elia	2001	Methane, Methane/diluent mixtures	0.8-1.2	298-550	0.75-70	Spherical vessel / Correlations
[143]	Rozenchan	2002	Methane, Methane/Oxygen, Methane/Oxygen/Helium	0.6-1.4	298	1-60	Constant-pressure combustion chamber
[144]	Bosschaart	2004	Methane, Ethane, Propane, n-Butane	0.6-1.6	293-360	1	Heat flux
[128]	Han	2006	Methane, Methane/Hydrogen/Carbon monoxide mixtures	1	298-498	1-5	Cylindrical bomb / Correlations
[137]	Coppens	2007	Methane/Hydrogen/Nitrogen mixtures	0.7-1.5	300	1	Heat flux
[129]	Ouimette	2009	Methane, Wood Syngas	0.5-1.5	300-850	1-15.2	Burner for Syngas Numerical simulations for CH_4 / Correlations
[145]	Bourque	2010	Methane, Natural gas	0.7-1.3	298	1-4	Cylindrical bomb with Schlieren setup
[146]	Park	2011	Methane, C_1-C_4/Hydrogen/CO mixtures	0.5-1.3	298 (423)	1-4	Counter flow
[147]	Lowry	2011	Methane, Ethane, Propane, Methane/Ethane and Methane/Propane mixtures	0.7-1.3	298	1-10	Constant-volume vessel with Schlieren optical setup
[22]	Dirrenberger	2011	Methane, Ethane, Propane, n-Butane Methane/Ethane and Methane/Propane mixtures, Natural Gas	0.6-2.1	298	1	Heat flux method with flame adiabatic burner / Correlations
[113]	Hu	2015	Methane	0.7-1.4	298-443	1-5	Constant-volume bomb / Correlations
[148]	Li	2015	Methane/n-Heptane mixtures	0.7-1.5	358-428	1	outwardly cylindrical constant-volume combustion chamber

Table 4.6: Coefficients proposed for the term $S_{L0}(\phi)$ in Equation (4.10) for methane, propane and gasoline.

Fuel	Z	W $[cm/s]$	η	ξ	σ
CH_4	1	38.85	-0.20	6.45	1.08
C_3H_8	1	42.11	-0.25	5.24	1.10
Gasoline	1	36.82	-0.22	4.86	1.11

Table 4.7: Coefficients proposed for exponents α and β in Equation (4.16) for methane, propane, natural gas and gasoline.

Fuel	a_2	a_1	a_0	b_2	b_1	b_0
CH_4	4.9199	10.287	6.9258	1.3712	2.6808	1.7492
C_3H_8	2.7620	5.8808	4.9221	0.9250	2.0000	1.3560
Natural Gas	5.7500	12.150	7.9800	0.9250	2.0000	1.3650
Gasoline	3.2800	7.5200	5.9300	0.9250	2.0120	1.3650

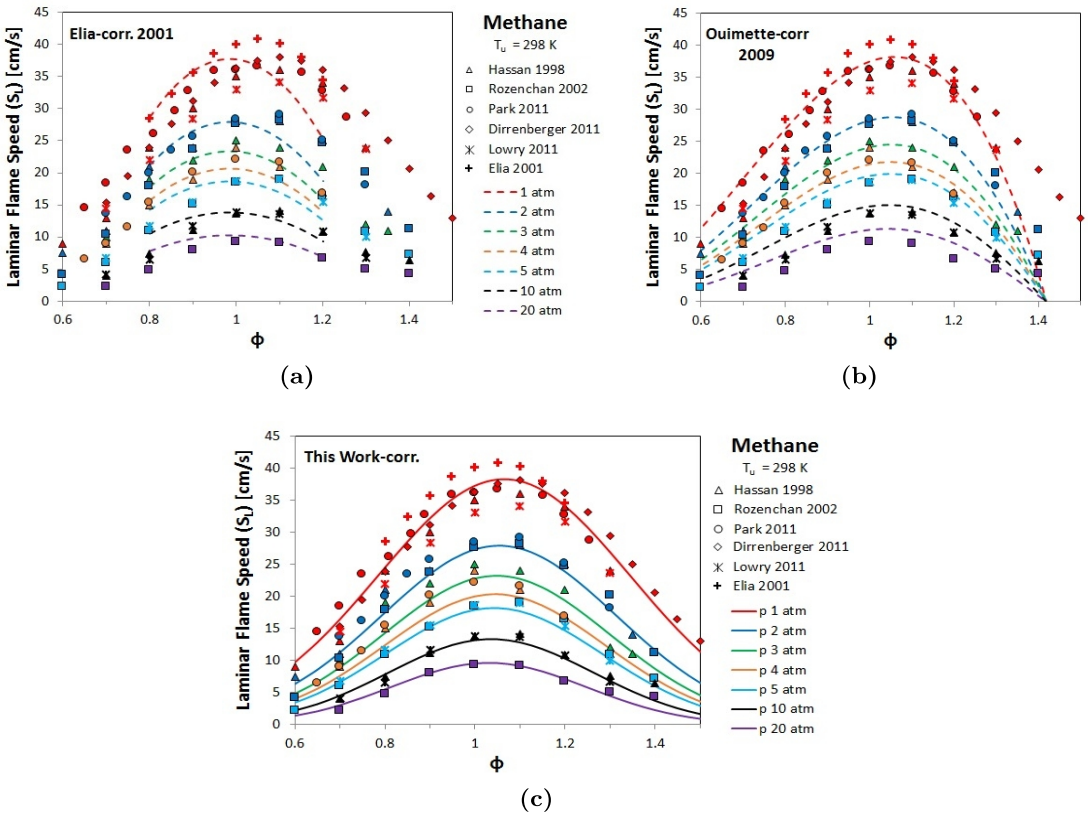

Figure 4.3: Methane laminar flame speed at room temperature and different pressures. Correlation in this work (a) and correlations of Elia et al. [127] (b) and Ouimette et al. [129] (c). Marks: experimental data; solid line: empirical correlation proposed in this work; dashed lines: other correlations.

Figure 4.5 reports the effects of an increase of unburnt mixture temperature, considering different initial pressures. For the case of room pressure (Figure 4.5(a))), a comparison with Ouimette's correlation is also reported, which is not able to reproduce the pressure influence in any of the equivalence ratios considered. However, the present correlation shows good agreement in all considered cases.

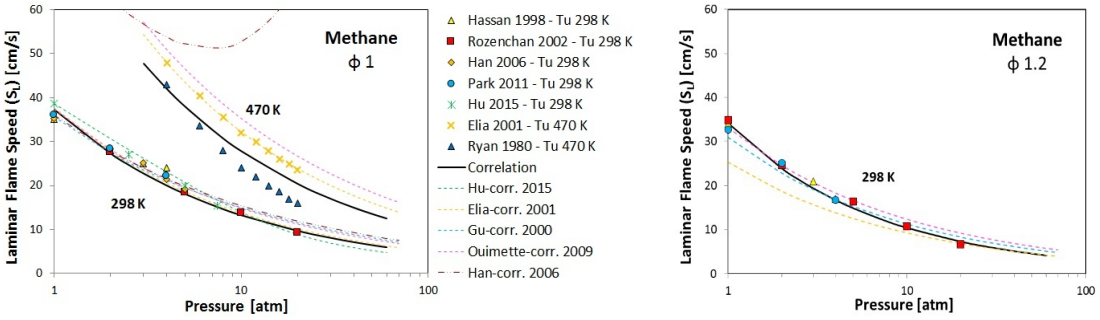

(a) (b)

Figure 4.4: Initial pressure influence on methane laminar flame speed, considering an equivalence ratio equal to 1 (a) and 1.2 (b). Marks: experimental data; dashed lines: correlations available in literature; solid line: empirical correlation proposed in this work.

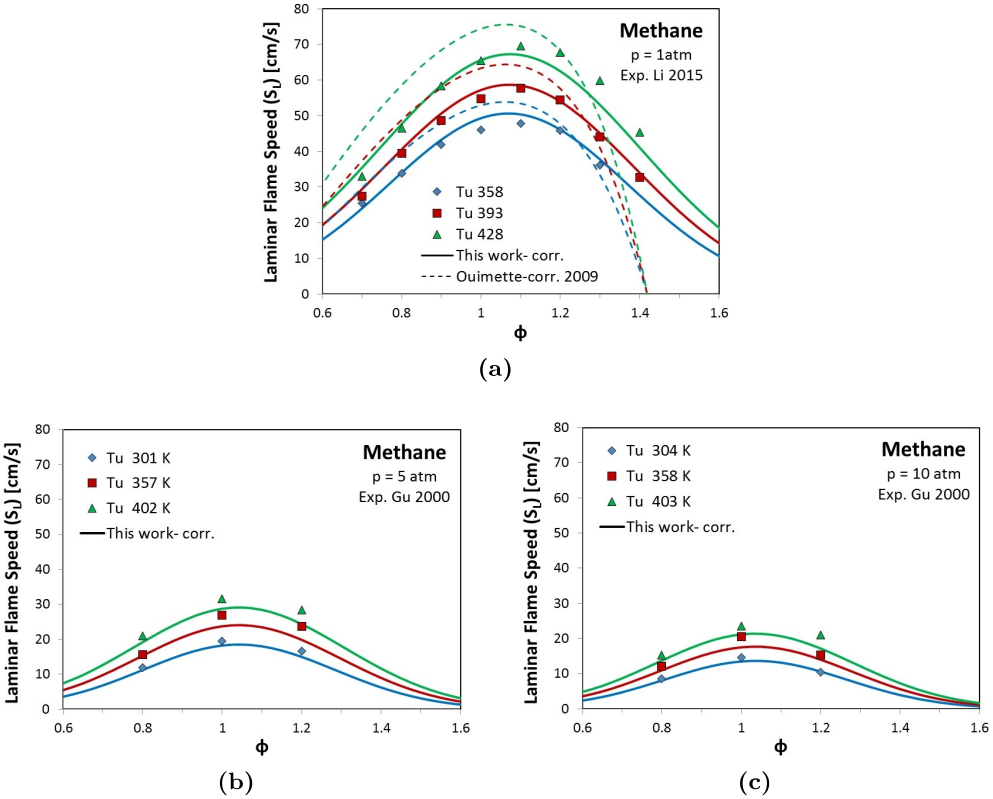

(a) (b) (c)

Figure 4.5: Methane laminar flame speed at high temperatures and pressures at different equivalence ratios. Comparisons with experimental data available at 1 (a), 5 (b) and 10 (c) atm. Marks: experimental data; dashed lines: correlations available in literature; solid line: empirical correlation proposed in this work.

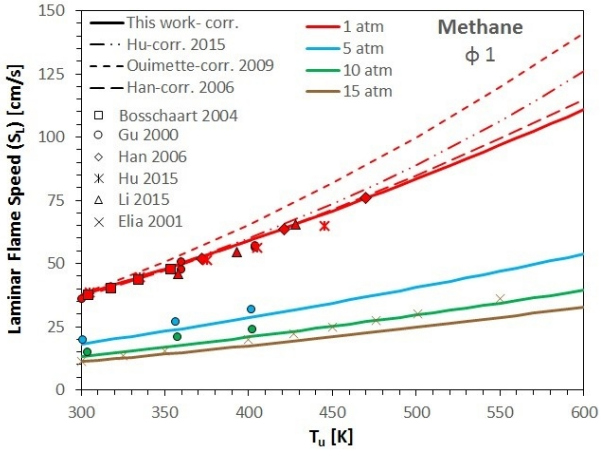

Figure 4.6: Methane laminar flame speed at high temperatures and pressures at different equivalence ratios. Comparisons with experimental data available at 1 (a), 5 (b) and 10 (c) atm. Marks: experimental data; dashed lines: correlations available in literature; solid line: empirical correlation proposed in this work.

The initial temperature effects are summarized for the stochiometric case in Figure 4.6. Different unburnt mixture pressures are considered as well. At room pressure, the agreement with the experimental data is good, while the other empirical correlations considered tend to overestimate the temperature influence. At higher pressures, the agreement can be considered satisfactory.

However, the data become even scarce when lean and rich mixtures are considered. Therefore, measurements that consider high initial pressures and temperatures are needed for a deeper analysis.

Propane

Propane is usually used in many applications, e.g., laboratory studies of oxidation processes and internal combustion engines. Unlike hydrocarbons fuel with simple structures such as methane and ethane, the thermochemical and combustion properties of propane are similar in many ways to those of a more complex practical fuel [110]. For this reason, a considerable body of studies have been focused on the measurement of its laminar burning velocity. As for methane, the literature considered in the present work is summarized and listed in Table 4.8.

The result of the curve fitting for propane at 1 atm and 298 K is reported in Figure 4.7 and the coefficients for propane are listed in Table 4.6. Some of the empirical correlations available in literature are also plotted. Similar findings as those for methane are seen for the correlations proposed by Gülder [110] ad Dirrenberger et al. [22]. The well-known Metghalchi's correlation (Equation (4.3)) is not far from the best fit, but cannot be adopted for equivalence ratios lower than 0.8 and larger than 1.5 due to its second-order polynomial form. The correlation proposed by Huzayyin et al. [131] consisted of a fourth-order polynomial expression for $S_{L0}(\phi)$ and although it shows reasonable agreement with the measurements from which it was developed, a large

discrepancy appears when it is compared with all the other data considered, since their experimental measurements gave values considerably higher than all the others.

The effects of initial pressure are provided in Figure 4.8. The obtained coefficients for the exponents α and β in Equation (4.16) are listed in Table 4.7. Figure 4.8 shows good agreement with all the various literature experiments in which the pressure was varied for 1 to 5 atm. Since Gülder [110] proposed constant values for both α and β, that correlation is not able to reproduce pressure effects at different equivalence ratios, as shown in Figure 4.8(a). Metghalchi et al. [64] proposed a linear expression for both α and β, and the comparison with experimental data (Figure 4.8(a)) makes visible the above-discussed limitations of such an expression.

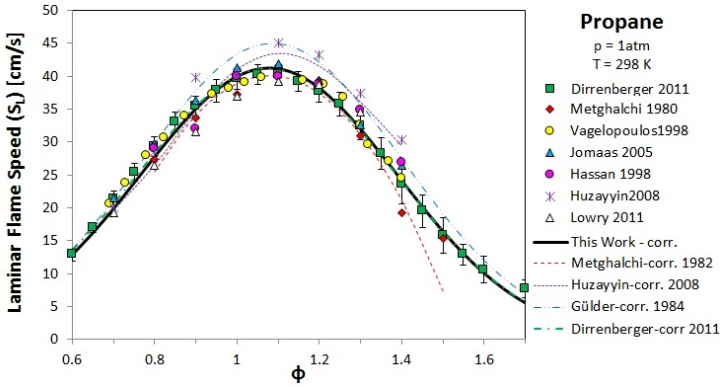

Figure 4.7: Propane laminar flame speed at room conditions. Marks: experimental data; dashed lines: correlations available in literature; solid line: empirical correlation proposed in this work.

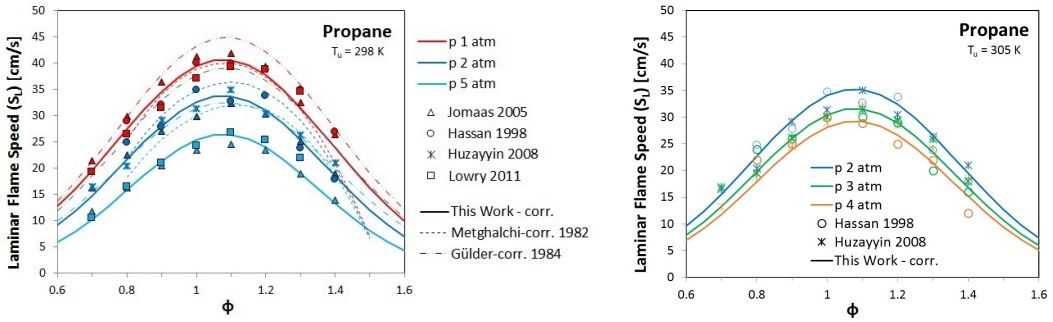

(a) (b)

Figure 4.8: Initial pressure influence on propane laminar flame speed at room temperature (a) and 305 K (b). Marks: experimental data; solid line: empirical correlation proposed in this work; dashed lines: other correlations.

Table 4.8: Literature considered for propane.

Ref.	Authors	year	Fuels	Φ	T_u [K]	p_u[atm]	Method
[118]	Dugger	1952	Methane, Propane, Ethylene	0.7-1.5	200-617	1-11	Burner with total area of outer edge of the cone shadow
[149]	Kuehl	1961	Propane	0.7-1.7	311-866.5	0.23-1	Modified slot burner with square burner tube
[150]	Agnew	1961	Methane, Propane, Ethylene, Acetylene, Hydrogen	1	298	0.2-20	Constant-volume bomb
[151]	Chase	1963	Acetylene, Propane	0.8 and 1	280-520	0.5-2.3	Burner
[112]	Metghalchi	1980	Propane	0.8-1.5	298-750	0.4-40	Spherical bomb
[64]	Metghalchi	1982	Methanol, Isooctane, Indolene	0.8-1.5	298-700	0.4-50	Constant-volume bomb / Correlations
[110]	Gülder	1984	Methane, Propane, Isooctane, Methanol, Ethanol, Alcohol/Isooctane, Alcohol/water	0.7-1.4	298-800	1-20	Constant-volume bomb / Correlations
[152]	Vagelopoulos	1998	Methane, Ethane, Propane	0.6-1.5	298	1	Counter flow, opposed-jet technique
[128]	Hassan	1998	Ethane, Ethylene, Propane	0.8-1.6	298	0.5-4	Outwardly spherical bomb
[153]	Jomaas	2005	Acetylene, Ethylene, Ethane, Propylene, Propane	0.6-2	298	1-5	Spherical bomb
[154]	Tang	2008	Propane/Hydrogen	0.8 and 1.2	300-440	1-50	Spherical vessel
[131]	Huzayyin	2008	LPG, Propane	0.7-2.2	295-400	0.5-4	Cylindrical bomb / Correlations
[155]	Razus	2010	Propane	vol.% 2.50-6.20	298-423	0.3-1.2	Spherical vessel
[147]	Lowry	2011	Methane, Ethane, Propane Methane/Ethane, Methane/Propane	0.7-1.3	298	1-10	Constant-volume vessel with Schlieren optical setup
[22]	Dirrenberger	2011	Methane, Ethane, Propane, n-Butane, Methane/Ethane, Methane/Propane, Natural Gas	0.6-2.1	298	1	Heat flux method with flame adiabatic burner / Correlations

Table 4.9: Coefficients of Equation (4.18) for binary mixtures.

Fuel	ν	τ	ε	Ω
CH_4/ C_2H_6	0.20	1.50	0.95	0.09
CH_4/ C_3H_8	0.10	1.50	1.30	0.20

Figure 4.9 summarizes the effect of pressure for stochiometric propane. Experiments carried out before the 80s give a faster laminar burning, since they did not consider stretch effects. In addition, Figure 4.9 shows that the value chosen by Gülder [110] for exponent β, which was in perfect agreement with his experiments, gives the fastest laminar flame speed among those that are proposed in this study. Conversely, the linear form by Metghalchi et al. [64] tends to underestimate the pressure effects in stochiometric conditions.

Figure 4.10(a) depicts the effects of an increase of unburnt mixture temperature, for initial pressure equal to 1 atm. In Figure 4.10(b) the effects are summarized for three different equivalence ratios, namely 0.8, 1 and 1.5, and good agreement is obtained by the present correlation. The Gülder [110] value for β is inappropriate when the initial temperature is increased, and with the linear form of Metghalchi et al. [64] the temperature influence is overestimated for rich mixtures and underestimated for near-stochiometric and slightly lean conditions.

Methane/ethane and methane/propane mixtures

A study of binary mixtures of methane with ethane and propane allows the development of empirical correlations to reproduce the laminar flame speed of different types of natural gas, since the methane fraction can vary between 55.8% and 98.1%, ethane can vary between 0.5% and 13.3%, and propane can vary between 0% and 23.7% [61].

Dirrenberger et al. [22] proposed a modified version of Gülder's expression to take into account the presence of another compound with methane. They found that their correlation reproduced well the experimental results for lean and rich mixtures, but overestimated flame velocities near stoichiometry. This because their modifications considered only the influence on the peak amplitude and position. From their experimental data, it seems that the lean and the rich side are more sensitive to the addition of another compound. Therefore, in order to take into account such behavior the coefficient η in Equation (4.11) has been multiplied by the term $(1-\chi)^{\varepsilon}$, resulting in the following expression:

$$S_{L0}(\phi,\chi) = (1+\nu\chi^{\tau})\ W\ \phi^{\eta(1-\chi)^{\varepsilon}}\ e^{-\xi(\phi-\sigma-\Omega\chi)^2}, \tag{4.17}$$

The coefficients ν, τ, ε and Ω derived in this study for methane/ethane and methane/propane mixtures are reported in Table 4.9. The terms W, η, ξ and σ refer to pure methane (Table 4.6).

The works that were considered for the analysis are reported in Table 4.10. Figure 4.11 shows the results for different fractions of ethane in methane, while Figure 4.12a refers to methane/propane mixtures. From Figures 4.11(a) and 4.12(a) it is seen that

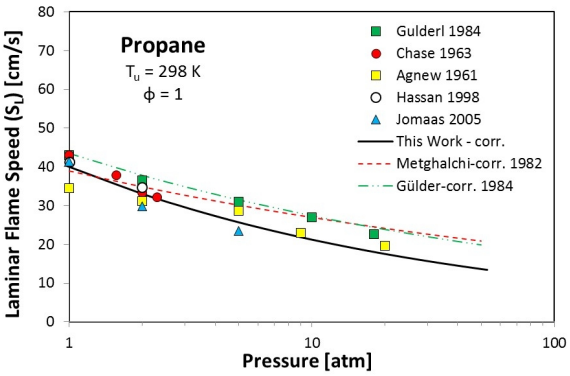

Figure 4.9: Initial pressure influence on propane laminar flame speed at stochiometric conditions. Marks: experimental data; dashed lines: correlations available in literature; solid line: empirical correlation proposed in this work.

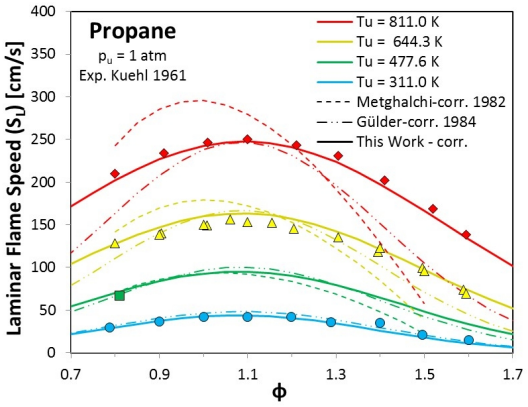

(a)

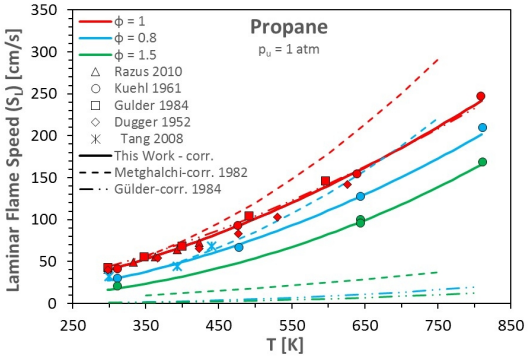

(b)

Figure 4.10: Initial temperature influence on propane laminar flame speed at room pressure, considering an equivalence ratio ranging from 0.7 to 1.7 (a). Comparison with other available data for equivalence ratio equal to 0.8, 1 and 1.5 (b). Marks: experimental data; solid line: empirical correlation proposed in this work; dashed lines: other correlations.

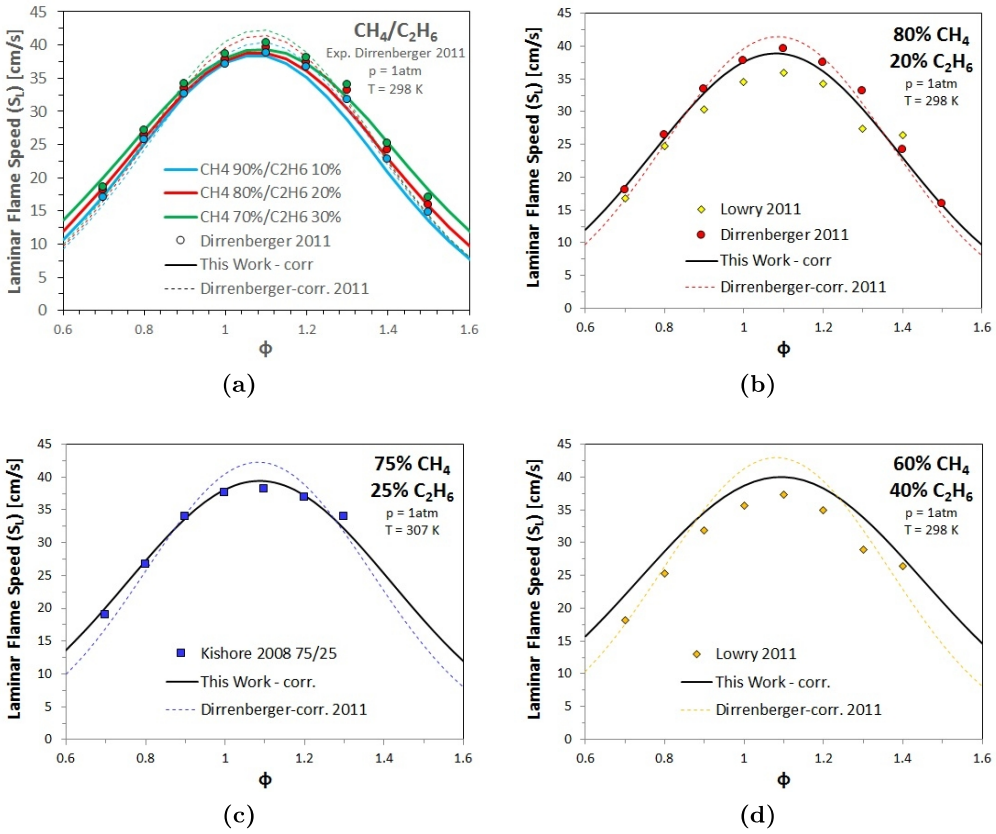

Figure 4.11: Laminar flame speed of methane/ethane mixtures at room conditions, considering different ethane content in methane. Marks: experimental data; dashed lines: correlations proposed by Dirrenberger et al. [22]; solid line: empirical correlation proposed in this work.

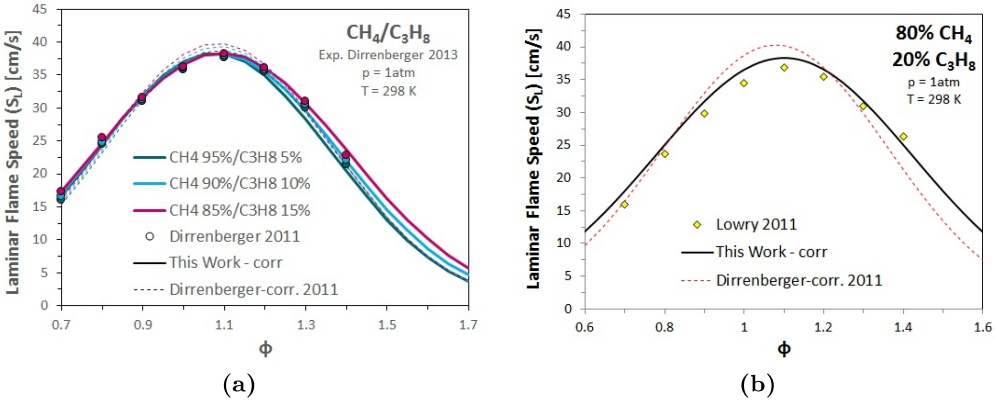

Figure 4.12: Laminar flame speed of methane/propane mixtures at room conditions, considering different ethane content in methane. Marks: experimental data; dashed lines: correlations available in literature; solid line: empirical correlation proposed in this work.

the proposed correlation reproduces the experimental trends better than the formulation proposed by Dirrenberger et al. [22], for all equivalence ratios considered. It captures the greater sensitivity to the addition of other compounds in methane for lean and rich mixtures.

Figures 4.11(b), 4.11(c) and 4.11(d) offer a comparison with other experimental measurements for methane/ethane, and Figure 4.12(b) compares methane/propane mixtures. The overall agreement can be considered satisfactory.

Natural Gas

Natural gas is increasingly used as an alternative to petroleum fuels in internal combustion engines and industrial power plants [14, 156] because of its smaller environmental effects compared to diesel and gasoline [11, 14, 16, 157], as well as for economic reasons [158]. New combustion techniques [5, 6] are related to the use of natural gas, as well as their control strategies [7–9],

Dirrenberger et al. [22] proposed a correlation valid for a natural gas surrogate mixture of methane, ethane and propane, which was obtained by combining the expressions derived for binary methane/ethane and methane/propane mixtures. The same approach has been adopted in this study, resulting in the following expression:

$$S_{L0}\left(\phi,\chi_1,\chi_2\right) = \left(1+\nu{\chi_1}^{\tau_1}\right)\left(1+\nu{\chi_2}^{\tau_2}\right)\ W\ \phi^{\eta(1-\chi_1)^{\varepsilon_1}(1-\chi_2)^{\varepsilon_2}}\ \ e^{-\xi(\phi-\sigma-\Omega_1\chi_1-\Omega_2\chi_2)^2}, \tag{4.18}$$

In which the terms W, η, ξ and σ refer to pure methane (Table 4.6), while the coefficients ν, τ, ε and Ω for ethane and propane are the same as derived in the previous section, and are reported in Table 4.10. The works considered are listed in Table 4.11.

Dirrenberger et al. [22] studied three surrogate mixtures with compositions close to those of three representative natural gases: Indonesia, Abu Dhabi and Pittsburgh, and Table 4.12 shows their exact composition of these natural gases. In such study, they were represented by the following mixtures: 90% CH_4, 6% C_2H_6, and 4% C_3H_8 Indonesia, 82% CH_4, 16% C_2H_6, and 2% C_3H_8 Abu Dhabi and 85% CH_4 and 15% C_2H_6 Pittsburgh. The results for each natural gas are reported in Figure 4.13, together with a comparison with the empirical correlation proposed by Dirrenberger et al. [22] (Equation (4.12)). The dependence upon the equivalence ratio and the fuel composition is well captured by the present proposed correlation and it shows better agreement, especially near stoichiometry.

Table 4.12 also reports the composition of the two natural gas mixtures that were the focus of the study by Bourque et al. [145]. they were represented by the following mixtures: 85% CH_4, 10% C_2H_6, and 5% C_3H_8 for NG2, 70% CH_4, 20% C_2H_6, and 10% C_3H_8 for NG3. The results for each natural gas are reported in Figure 4.14(a). The Dirrenberger et al. correlation [22] overestimates the maximum flame speed, but the correlation proposed in this study shows an overall better agreement with the experiments. In addition, it is able to capture the influence of the composition far from stoichiometry.

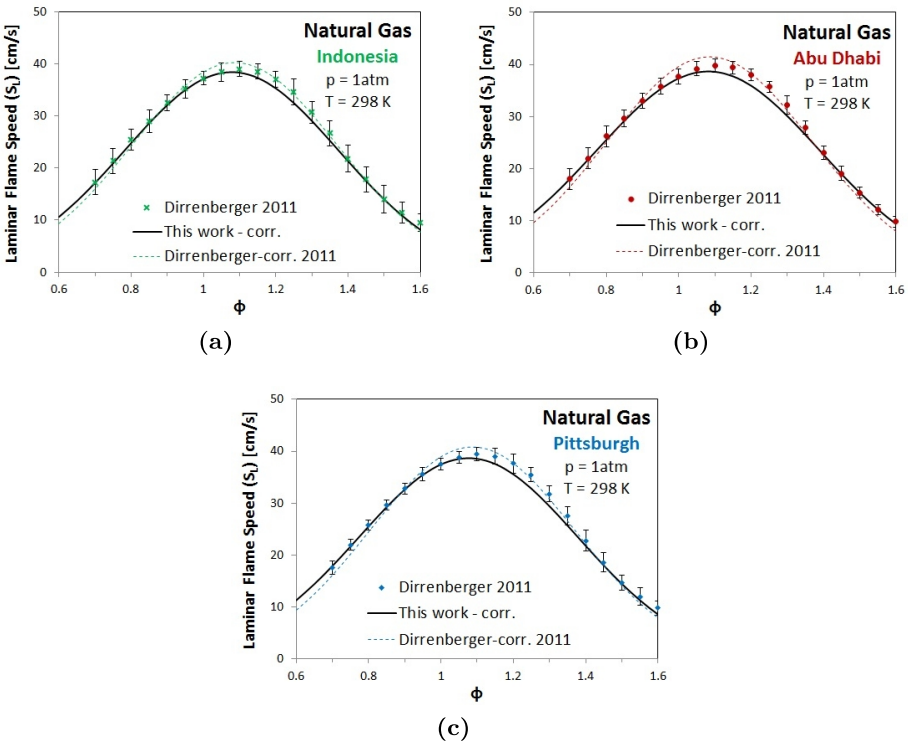

Figure 4.13: Laminar flame speeds of different natural gases at room conditions. Marks: experimental data; dashed lines: correlations proposed by Dirrenberger et al. [22]; solid line: empirical correlation proposed in this work.

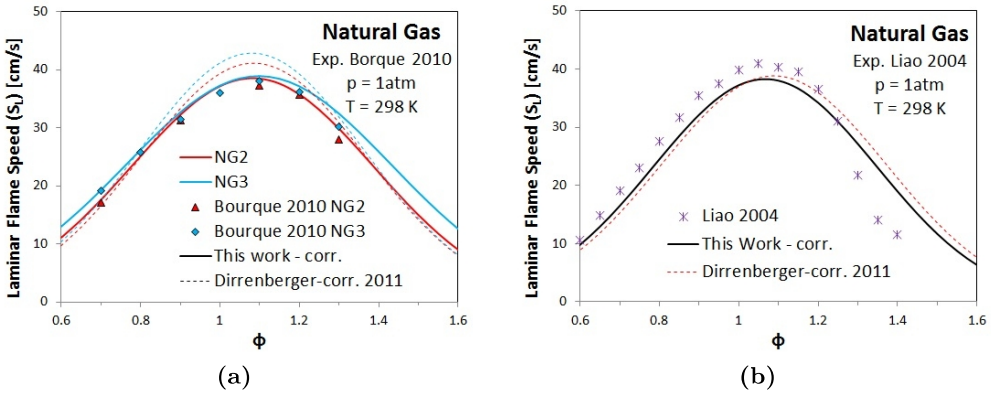

Figure 4.14: Laminar flame speed of different natural gases measured by Bourque et al. [145] (a) and Liao et al. [130] at room conditions. Marks: experimental data; dashed lines: correlations proposed by Dirrenberger et al. [22]; solid line: empirical correlation proposed in this work.

Table 4.10: Literature considered for methane/ethane and methane/propane mixtures.

Ref.	Authors	year	Fuels	Phi	T_u [K]	p_u [atm]	Method
[159]	Kishore	2008	Methane, Ethane, Methane/Ethane mixtures	0.7-1.3	307	1	Heat flux
[147]	Lowry	2011	Methane, Ethane, Propane Methane/Ethane, Methane/Propane	0.7-1.3	298	1-10	Constant-volume vessel with schlieren optical setup
[22]	Dirrenberger	2011	Methane, Ethane, Propane, n-Butane, Methane/Ethane, Methane/Propane, Natural Gas	0.6-2.1	298	1	Heat flux method with flame adiabatic burner / Correlations

Table 4.11: Literature considered for natural gas.

Ref.	Authors	year	Fuels	Phi	T_u [K]	p_u [atm]	Method
[130]	Liao	2004	Shannxi Natural Gas	0.6-1.4	300-400	0.5-1.5	Spherical bomb
[145]	Bourque	2010	Methane, Natural gas	0.7-1.3	298	1-4	Cylindrical bomb with Schlieren setup
[22]	Dirrenberger	2011	Methane, Ethane, Propane, Butane, Methane/Ethane, Methane/Propane, Natural Gas	0.6-2.1	298	1	Heat flux method with flame adiabatic burner / Correlations

Table 4.12: Composition of different natural gases (% Volume) considered.

Ref.	Authors	year	Fuels	CH_4	C_2H_6	C_3H_8	i-C_4H_{10}	n- C_4H_{10}	i-C_5H_{12}	n-C_5H_{12}	CO_2	N_2	others
[130]	Liao	2004	Shannxi	96.16	1.096	-	-	-	-	-	-	-	2.74
[145]	Bourque	2010	NG2	81.25	10.0	5.0	-	2.50	-	1.25	-	-	-
			NG3	62.50	20.0	10.0	-	5.00	-	2.50	-	-	-
[22]	Dirrenberger	2011	Indonesia	89.91	5.44	3.16	1	0.75	0.03	-	-	0.04	-
			Abu Dhabi	82.07	15.86	1.89	-	0.06	-	-	-	0.05	-
			Pittsburgh	85.00	14.0	-	-	-	-	-	-	1.00	-

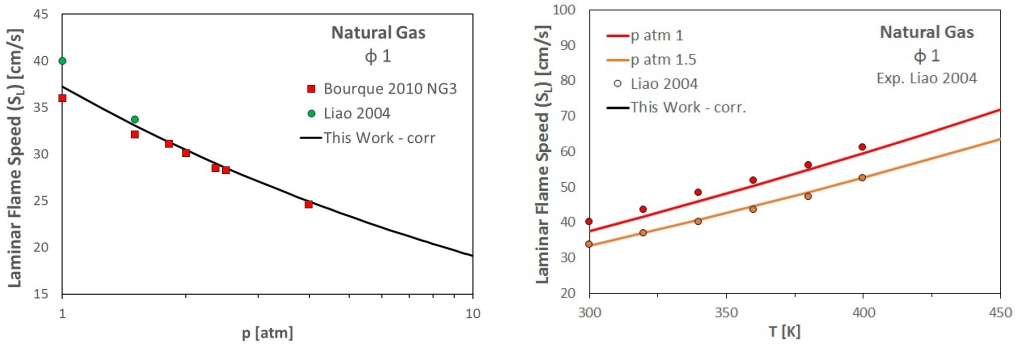

(a) (b)

Figure 4.15: Initial pressure (a) and temperature (b) influence on natural gas laminar flame speed at stoichiometric conditions. Marks: experimental data; solid lines: empirical correlation proposed in this work.

Figure 4.14(b) reports results for the natural gas investigated by Liao et al. [130]. Its composition is reported in Table 4.12 as well. It was represented by considering 98.9% $CH_4$and 1.1% C_2H_6. The values of the laminar flame speed reported in this study appear to be higher than those of the cases previously investigated, even though the natural gas was composed almost exclusively of methane. These experimental measurements report values that are higher than those presented previously for pure methane. Therefore, it is hard to judge the results shown in Figure 4.14(b).

Very few works have investigated the influence of initial pressure and temperature on natural gas laminar flame speed. Figure 4.15(a) shows results for different initial pressures and Figure 4.15(b) different initial temperatures. Only the stochiometric case has been investigated. The derived values for the coefficients of exponents α and β in Equation (4.16) are listed in Table 4.7. Liao et al. [130] investigated the temperature influence (the coefficients of exponent α are the same proposed by Liao et al. [130]).

Gasoline

As for natural gas mixtures, much less data than for methane and propane are available for fuels with low vapor pressure. Laminar flame speed data of commercial gasoline are summarized in Table 4.13.

For gasoline, the term $S_{L0}(\phi, \chi)$ is modeled in the same way as for methane and propane. This because variations in the composition of gasoline have not been taken into account in any flame speed measurements. Figure 4.16 compares the results obtained by using the coefficients reported in Table 4.6 for gasoline, with experimental measurements carried out at 358 and 353 K and room pressure found in literature.

Sileghem et al. [114] investigated the influence of the initial temperature from 298 to 358 K, at room pressure. Their experimental data are reported in Figure 4.17(a). They used the same second-order polynomial form for the exponents α and β of Equation (4.16) for fitting the data. However, different coefficients from those suggested by Sileghem et al. [114] are proposed here, since additional experimental measurements are considerate in this analysis, as reported in Figure 4.17(b).

Table 4.13: Literature considered for gasoline.

Ref.	Authors	year	Fuels	Phi	T [K]	p [atm]	Method
[140]	Zhao	2003	Gasoline (CR-87)	0.6-1.4	353 & 500	1	Single jet-wall stagnation flame
[160]	Jerzembeck	2009	n-Heptane, Isooctane, PRF 87, Gasoline	0.7-1.2	373	10-25	Constant volume bomb
[161]	Tian	2010	2,5-Dimethylfuran, Ethanol, Gasoline (EN228)	0.6-2.0	323-373	1	Constant volume vessel and high speed schlieren visualization
[114]	Sileghem	2013	Isooctane, n-Heptane, Toluene, TRF, Gasoline (Exxon 708629-60)	0.7-1.3	298-358	1	Heat flux method on a flat flame adiabatic burner
[139]	Dirrenberger	2014	iso-octane/n-heptane/ toluene mixture Gasoline (TAE7000)	0.6-1.5	358	1	Heat flux method

Jerzembeck et al. [160] carried out measurements for unburnt mixture pressures higher than 1 atm, as reported in Figure 4.17(c). Measurements were available at three equivalence ratios and at an initial temperature of 373 K, and the resulting coefficients for exponents α and β are reported in Table 4.7.

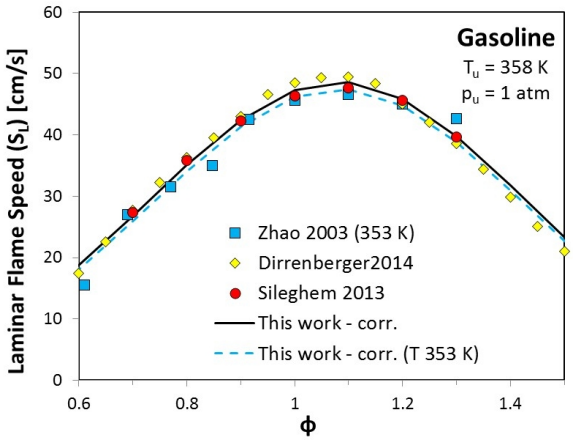

Figure 4.16: Gasoline laminar flame speed at room pressure and at two different temperatures. Marks: experimental data; lines: empirical correlation proposed in this work.

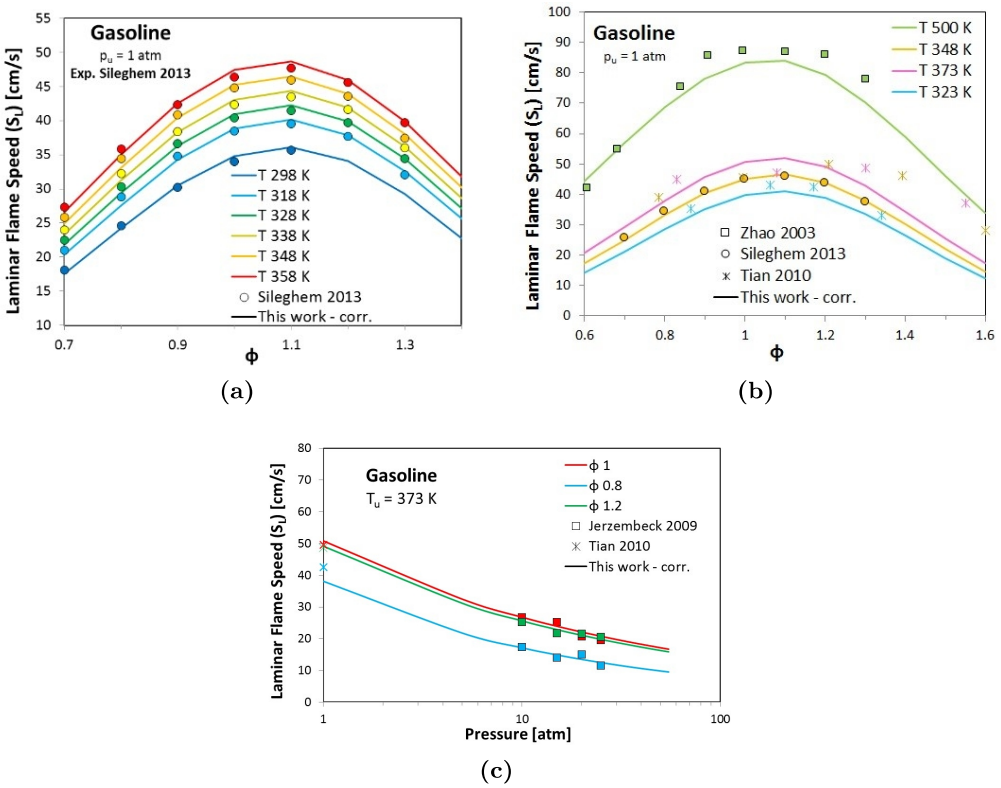

Figure 4.17: Initial temperature influence on gasoline laminar flame speed at room pressure (a) and (b). Initial pressure influence at three different equivalence ratios and at an initial temperature of 373 K (c). Marks: experimental data; lines: empirical correlation proposed in this work.

4.4 Conclusions

The present study provides simple and workable expressions, suitable for spark-ignition engine simulations, that allow laminar flame speed calculations of some practical fuels. Pure compounds, such as methane and propane, binary mixtures of methane/ethane and methane/propane, as well as more complex fuels like natural gas and gasoline were considered. Knowing the behavior of the laminar flame speed as a function of the unburnt mixture strength, temperature and pressure is essential for an efficient and reliable simulation of the combustion process that occurs in a spark-ignition engine.

Measurements of laminar flame speeds in literature were collected and used to develop empirical correlations for the laminar flame speed for equivalence ratios from 0.6 to 1.7, pressures between 1 and 50 atm and temperature from 298 to 800 K.

The correlations proposed in this work have the "power law" form (Equation (4.10)), with $p_0 = 1\ atm$ and $T_0 = 298\ K$. $S_{L0}(\phi)$ term is represented using "Gülder's exponential formulation" (Equation (4.10)), while the exponents α and β were functions of mixture strength ϕ and a second-order polynomial fitting was considered (Equation (4.16)).

Empirical correlations available in literature generally were not able to give good agreement with recent experimental data. This because many of them were based on a single set of measurements and fail outside the considered experimental range.

For binary and ternary mixtures, it was shown that the influence that the amount of the secondary compounds has on the mixture laminar flame speed is different at different equivalence ratios which has not been considered in previous formulations. Therefore, a modified expression for the term $S_{L0}(\phi)$ was proposed (Equation (4.18)), and better overall agreements with all the experimental data was obtained.

An improved formulation was developed for calculating the laminar flame speed of natural gas, which was modeled as a ternary mixture of methane, ethane and propane. Comparisons with experimental data on natural gases having different compositions confirmed the obtained improvements.

Gasoline was treated as a single component fuel. However, the proposed correlation resulted in agreement with all the available data taken from the literature and for the unburnt mixture pressure and temperature ranges considered.

Soot Formation and Oxidation in Gasoline-Oxygenated Combustion

5

Oxygenated fuels are often added to gasoline in order to achieve more efficient combustion. However, Chemical mechanisms are still uncertain and ambiguous results can be produced when the effect of oxygenated fuels on gasoline engine combustion is considered. This Chapter reports the results deriving from 3-D CFD simulations and experimental measurements, in which, to avoid the uncertainties associated with chemistry models, load increases in stoichiometric SI engine combustion were achieved by pure oxygen addition to provide basic information on soot formation and oxidation mechanics. 5% and 10% by volume of additional oxygen (with respect to air) was mixed with gasoline within the intake manifold of a small single-cylinder Port Fuel Injection SI engine.

5.1 Introduction

The gasoline direct injection strategy has attracted great interest due to its capability to improve fuel economy and reduce gaseous emissions [162]. However, its development is much harder to implement due to the complexity of physics within the engine, which include intake air charge motion and air-fuel mixture formation from liquid fuel injection to spray atomization, and affects combustion and emissions [10, 162].

Oxygenated fuels represent an interesting alternative choice and they are often added to gasoline in order to achieve more efficient combustion. For example, alcohols, such as ethanol, butanol, and their blends with gasoline are considered as valid alternative fuels and have been studied extensively by many researchers [10, 25–28]. In particular, ethanol has become an additive of choice for oxygenated fuels in many places around the world [10, 26, 27, 163]. However, a number of other chemical compounds could be added to the fuel to produce the desired effects [164]. For example, the use of gasoline containing 3 to 10 vol% of bioethanol is being promoted in many parts of the world [165]. Ethanol has the potential to improve engine efficiency and to reduce harmful emissions

when used as the fuel in a spark-ignited engine [26, 28]. Kim et al. [27] highlighted that in order to fully utilize the merits of ethanol, the fuel-blending ratio should be changed according to the engine operating conditions. Other advantages include its high octane number and its self-sustainability, since it is obtained from renewable energy sources [28]. However, the effect on particulate emissions is not well understood.

Chemical mechanisms are still uncertain for practical fuels, and ambiguous results can be produced when the effect of oxygenated fuels on gasoline engine combustion is considered [29–31]. To better assess the influence on engine performance and emissions, it is necessary to developed well validated detailed kinetic models for combustion and oxidation of the components of biofuels. In addition, as Tran et al.[29] highlighted when they reviewed the major detailed kinetic models already proposed in the literature, some of the most recent mechanisms can be very large in terms of the species and reactions involved: for instance, the model of Harper et al. [166] for the oxidation of n-butanol consists of 263 species and 3381 reactions and that of Herbinet et al. [167] for the oxidation of methyl palmytate includes 30425 reactions and 4442 species.

In the present study, in order to provide additional basic information and, at the same time to avoid uncertainties from chemistry models, load increases in stoichiometric SI engine combustion were achieved by pure oxygen addition as a first step. 3-D Computational Fluid Dynamics simulations were performed and the numerical results were compared with experimental measurements, in which 5% and 10% by volume of additional oxygen (with respect to air) was mixed with gasoline within the intake manifold of a small single-cylinder Port Fuel Injection Spark-Ignition engine. Different engine operating conditions were also considered for a more exhaustive analysis.

Two different engine speeds were considered, namely 2000 and 4000 rev/min, which were assumed to be representative respectively of low and high engine speed regimes. For the low-speed case, the results are further analyzed to provided in-cylinder soot distributions and to better understand the reasons for the observed soot particle size distributions.

5.2 Experimental Method

Apparatus

The investigation was carried out on a 4-stroke single cylinder SI engine. The engine specifications are shown in Table 5.1. The engine was equipped with a Three-Way Catalyst (TWC) and it was water cooled.

A three-hole commercial low pressure injector was used for the gasoline injection. The oxygen was supplied within the intake manifold just before the intake runner to have enough time for the mixing. The purity of oxygen was 99.995% mol, the bottle capacity 50 l and the storage pressure 200 bar. A flow-control valve was used to control the oxygen flow rate. The gasoline chemical and physical properties are listed in Table 5.2.

The gasoline flow was measured by means of an oval gear meter operating in the range from 0.005 to 1.75 l/min. A linear lambda sensor Bosch LSU 4.9 installed at the exhaust was used to measure the air fuel ratio. A programmable electronic control unit

Table 5.1: Engine specifications.

Name	Units	Value
Cylinder volume	cm^3	250
Bore	mm	72
Stroke	mm	60
Compression ratio	None	10.5
Max power	kW	16 at 8000 rpm
Max torque	Nm	20 at 5500 rpm

Table 5.2: Chemical and physical properties of gasoline.

Name	Units	Value
Carbon	mass%	86.12
Hydrogen	mass%	13.25
Oxygen	mass%	0.63
Aromatic content	%v/v	35.00
Density - at 15 °C -	kg/l	0.75
Viscosity - at 20 °C -	mPa*s	0.39
LHV	MJ/l	32.00
Stoichiometric air/fuel	None	14.70
Motor Octane number	Rating	84.20
Research Octane number	Rating	94.50

(PECU) allowed the management of the injection timing as well as the ignition timing. The Duration Of Injection (DOI) was properly adjusted by closed loop control on the lambda value to obtain stoichiometric conditions.

The in-cylinder pressure was measured by means of a quartz pressure transducer flush-mounted in the region between the intake and exhaust valves. It measures the in-cylinder pressure with a sensitivity of 16.2 pC/bar and a natural frequency of 130 kHz. The sensor signal was recorded by a flexible data acquisition system equipped with 8 high speed analogue inputs.

PN concentrations and sizes were measured in the range from 5 to 560 nm by means of a TSI Engine Exhaust Particle Sizer. The exhausts were sampled and diluted by means of the Dekati Engine Exhaust Diluter, according to the Particle Measurement Programme (PMP) [168]. The dilution ratio was fixed at 1:79. A 1.5 m heated line was used for sampling the engine exhausts in order to avoid condensation of combustion water. The sample is first diluted with air heated above 150 °C. Then, the sample passes through an evaporation chamber at a temperature above 300 °C for removing volatile particles. This system allows to measure the solid particles defined by the PMP as particles that can survive passing through an Evaporation Tube with a wall temperature of 300–400 °C. Samples for the particle characterization were taken directly from the exhausts, shortly after leaving the cylinder.

Table 5.3: Operating condition specifications.

Engine speed [rpm]	**O_2 [%vol]**	**Spark Advance [CAD ATDC]**
2000	0	-22.0
	5	-12.5
	10	-12.5
4000	0	-24.0
	5	-24.0
	10	-24.0

Experimental procedure

The present tests focused on the analysis of the effect of a load increase in stoichiometric SI engine combustion, by means pure oxygen addition. In particular, 5% and 10% in volume of additional oxygen was mixed with gasoline within the intake manifold to explore loads higher than the wide open throttle case. All the tests were performed at steady state conditions and two engine speeds were investigated, namely 2000 and 4000 rpm.

The gasoline was injected at 3.5 bar and the end of injection was set at 230° BTDC. The Start of Spark (SOS) corresponded to the maximum brake torque timing, and at 2000 rpm it was properly modified to avoid knock occurrence when oxygen was added.

To ensure proper operation, the engine was first warmed up and the data were recorded only after engine conditions were stabilized. Tests were repeated three times in order to provide good statistics of the measurements and each test was averaged over 300 consecutive cycles.

The list of the conditions and important engine settings considered in the tests is reported in Table 5.3.

5.3 Numerical setup

Figure 5.1 shows the 3D computational mesh of the engine whose geometry is reported in Table 5.1. The computational mesh contains around 100,000 cells at bottom dead center (BDC), including the intake and exhaust manifolds and cylinder. Additional details are provided in Appendix A. The initial in-cylinder mixture was assumed to be completely homogeneous, and the simulations started from intake valve closure (IVC). The fuel was modeled as a surrogate mixture of ten components [88, 103] and the relative mole fractions are reported in Table 5.4.

A newly developed analytical Jacobian sparse matrix solver, SpeedCHEM [84], was also coupled with the current models to reduce the computation time for chemistry. This allows realistic modellingof the engine, together with multi-component fuel chemistry surrogates.

In-cilynder pressure and HRR traces obtained from the simulations were compared with the experimental measurements in order to validate the numerical results. Then

Table 5.4: Composition of the surrogate mixture of ten components used to model gasoline in the simulations.

Component	**Mole fraction**
nC_7H_{16}	0.055399
$nC_{10}H_{22}$	0.039687
$C_{10}H_{22}$	0.019337
iC_5H_{12}	0.411976
iC_7H_{16}	0.130568
iC_8H_{18}	0.074380
C_7H_8	0.101062
mxylene	0.062182
mcymene	0.073237
C_6H_{12}	0.032171

the results were further analyzed to provide in-cylinder soot distributions and to better understand the reasons for the observed soot particle size distributions.

5.4 Results and discussion

Figure 5.2 reports the in-cylinder pressure and HRR for the two engine speeds considered and illustrates that the effect of oxygen addition was to speed up the combustion process. At 4000 rpm the effects are more evident since these cases have similar the combustion phasing. As previously mentioned, at 2000 rpm, it was necessary

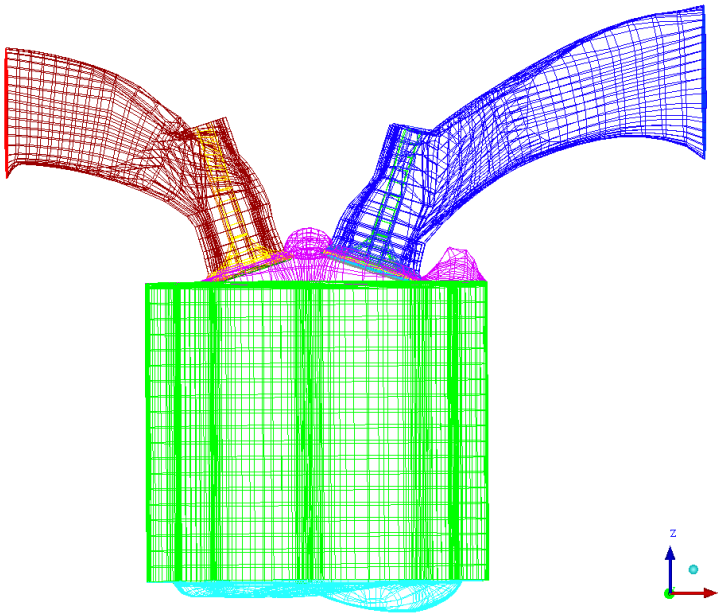

Figure 5.1: Computational mesh of the SI engine with pent-roof and bowl piston. 100,000 cells at BDC including intake and exhaust manifolds and valves.

to delay the ignition timing to avoid the onset of knocking phenomena. The faster combustion is ascribable to the higher burning velocity due to oxygen addition [169]. Moreover, the lower N_2 content (which is an inert that lowers the flame temperature by absorbing heat but does not contribute to the combustion), results in a higher local oxygen availability, contributing to the formation of a more homogeneous mixture that enhances the ignition as well as the flame propagation process.

Figure 5.2 also reports comparisons with the numerical simulations. The overall results can be considered more than satisfactory. Very good agreement was obtained for the low speed case (Figure 5.2a), while some slight discrepancies were found for the high speed case (Figure 5.2b) and that can be probably attributed to the absence of a crevice model. In real conditions, a significant amount of unburned gas ahead of the flame flows into the top-land crevice and it has been calculated that the crevice flow reduces the instantaneous in-cylinder charge mass by as much as 6% [170]. About 80% of this trapped mass (about 5% of the total cylinder mass) eventually returns to the chamber and is burned during the later stages of combustion, when the temperature is much lower [170]. In the simulations, the absence of this zone (i.e., a model that simulates this phenomenon) has the result that all the in-cylinder fuel survives far the flame propagation and is oxidized at higher temperatures, resulting in a sudden increase of pressure, as it is clearly observed from the baseline case at 4000 rpm (left-hand plot in Figure 5.2b, which shows a pressure bump after the main peak and a faster HRR at the conclusion of the combustion phase. At lower speeds this behavior is less relevant and therefore the simulations show better agreement.

Figure 5.3 points out that for all conditions the effect of oxygen addition is to

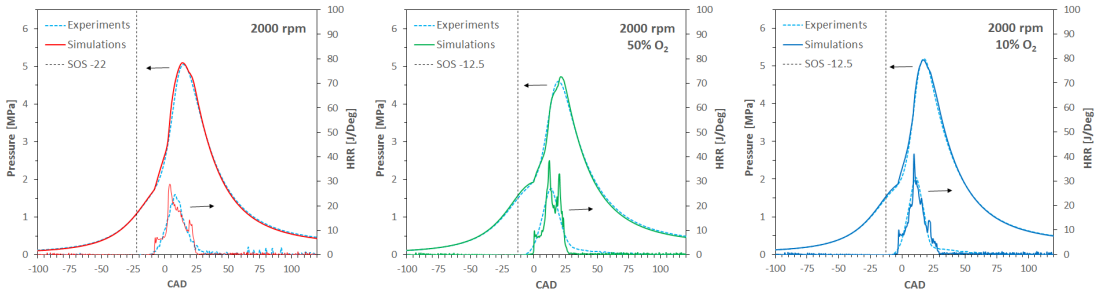

(a) 2000 rpm

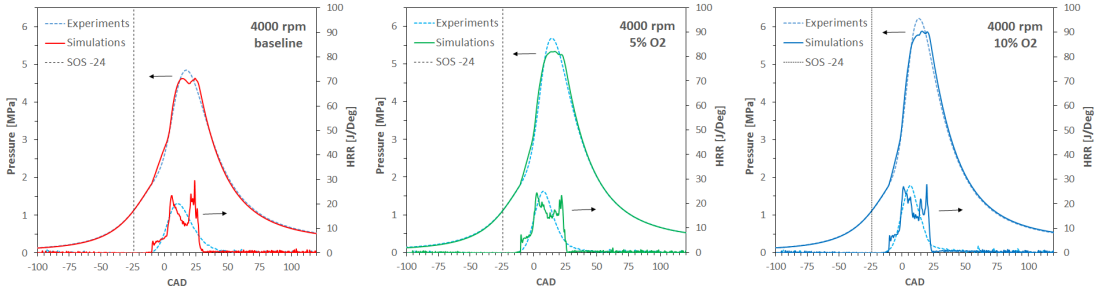

(b) 4000 rpm

Figure 5.2: In-cylinder pressure and HRR traces at 2000 (a) and 4000 (b) rpm. Dashed lines: experiments; solid lines: simulations; vertical dashed lines: Spark Advance.

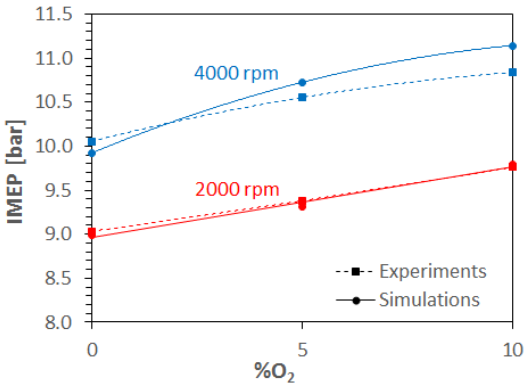

Figure 5.3: Load increase due to oxygen addition.

increase the IMEP. The increment is almost linear, namely adding 10% of oxygen results in a load increase of roughly 10% and this trend is well captured by the numerical model, especially for the low speed conditions. At 4000 rpm the IMEP increase is slightly overestimated due to the above-described crevice flow reasons. It must be noticed that stoichiometric conditions were kept during the experimental tests and therefore the increased IMEP values are ascribed to the larger amount of fuel that was injected, as is inferable from the larger fuel consumption that was recorded for the cases with oxygen addition.

The numerical model can be considered to have been successfully validated against the experimental data and can be used for a deeper analysis of the results relating to particle emission processes. In particular, the low-speed case, which showed the best agreement, was chosen for further investigation on the combustion and soot mechanics formation processes that are taking place within the engine. For sake of brevity, the two extreme cases, namely 0 and 10% of oxygen, are compared.

Figure 5.4 illustrates the propagation of the flame front location as represented by the G=0 (pink) surface after the transition from the kernel growth model to the turbulent flame propagation model, as well as the temperature distributions (cross section on x-z plane). The results indicate that combustion is due to flame propagation and that no auto-ignition (knock) is observed. The burnt regions swept by the flame surface can be easily distinguished from the unburnt regions. The red particles in the center were used to represent the kernel surface. The Spark Advance was delayed to avoid knock (Table 5.3) and therefore the turbulent flame with 10% oxygen (right-hand side of Figure 5.4) starts to propagate later than the baseline case. In the latter case, at -5°ATDC the transition from kernel growth to flame propagation has already occurred, while in the higher-load case the kernel is still growing. At TDC, in both cases, the turbulent flame is completely formed and it propagates radially towards the cylinder walls with a quasi-spherical shape. The fastest flame speed was found with oxygen addition, as can be inferred from the fact that at 10° ATDC the flame front position is practically the same, even though the spark was triggered 9 CAD later in the oxygen-enriched case. The two flames reach the cylinder wall simultaneously at about 20° ATDC. Slightly higher temperatures in the burned region are reached in a shorter time with oxygen addition, and in both cases the lowest temperature is recorded near

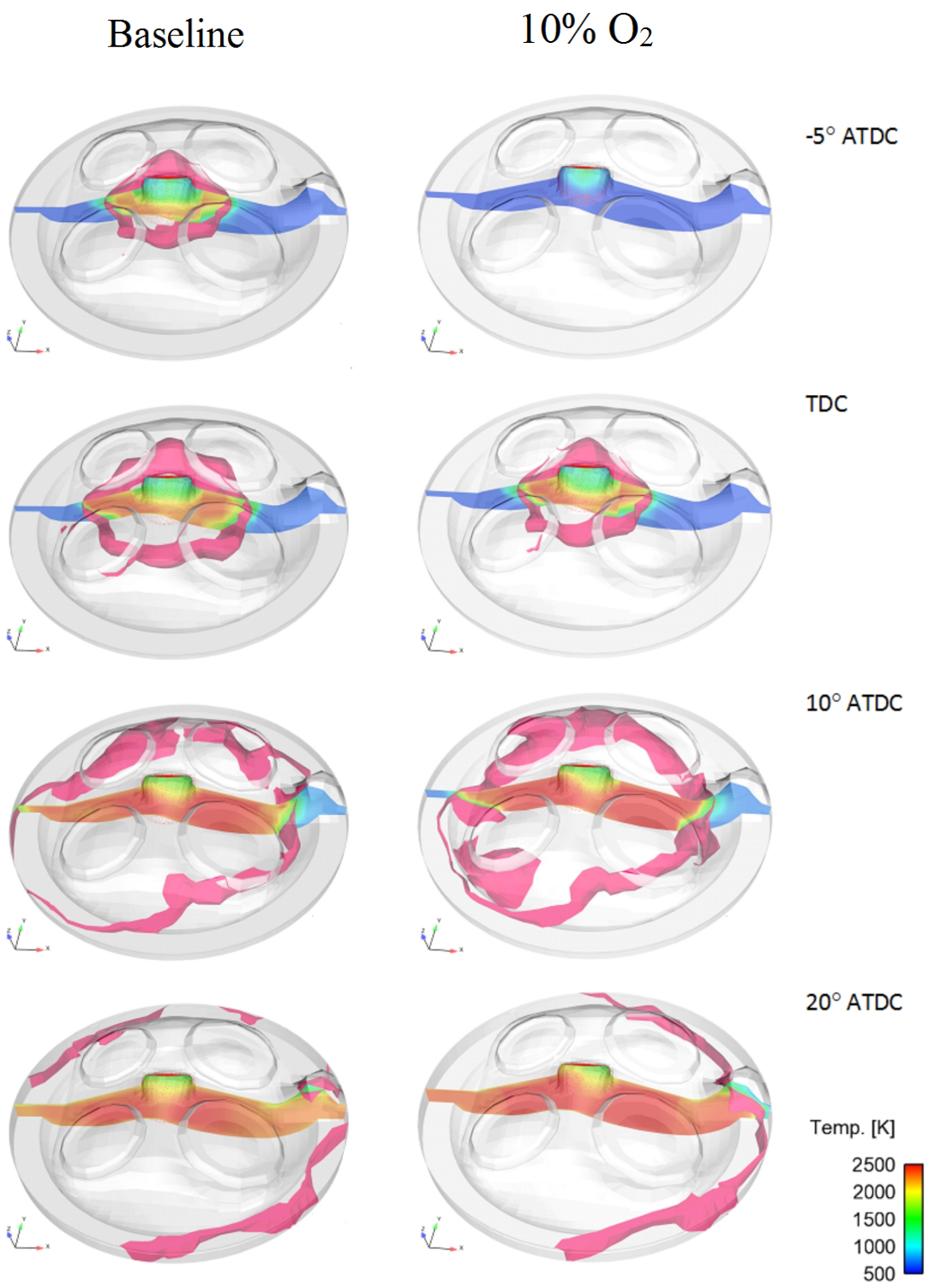

Figure 5.4: Evolution of in-cylinder turbulent flame and temperature field (plane x-z) for 2000 rpm case in the simulations. Red particles: kernel surface; pink surface: flame front.

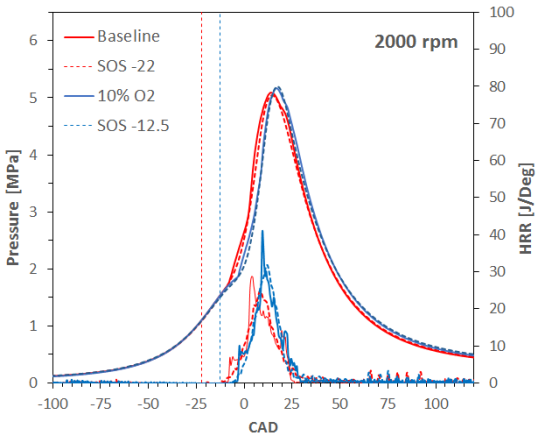

(a)

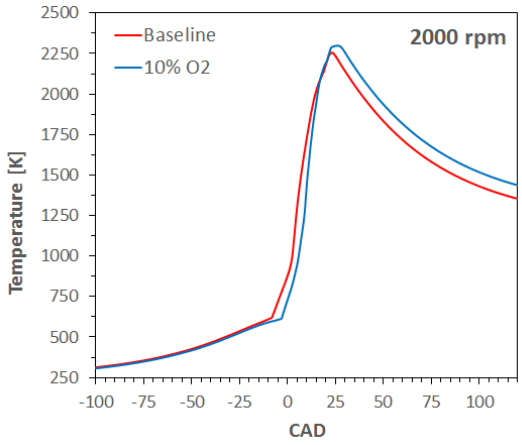

(b)

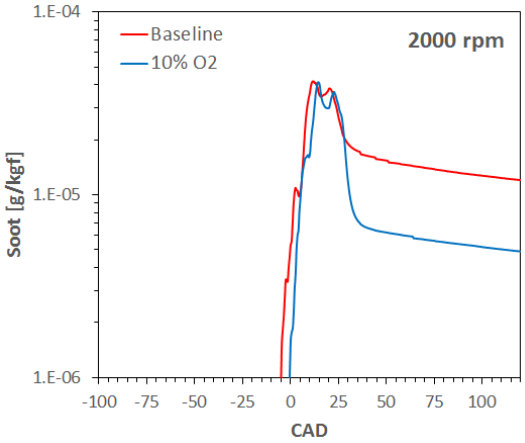

(c)

Figure 5.5: In-cylinder time evolution of pressure and HRR traces (a). Temperature (b) and specific soot mass (c) in the simulations of the 2000 rpm cases. Dashed lines: experiments; solid lines: simulations; vertical dashed lines: Spark Advance.

the spark-plug location, due to the particular cylinder-head shape.

The average in-cylinder temperature evolution is reported in Figure 5.5(b), which summarizes the results discussed in the previous figures and allows a comparison with the average in-cylinder pressure and HRR traces (Figure 5.5(a)). Figure 5.5(c) shows the time evolution of the soot mass per kg of fuel. When combustion begins, soot starts to increase and the highest peak is recorded in correspondence with the higher in-cylinder pressures and temperatures, just before the front flame reaches the wall. After that, soot decreases and oxygen addition produces a lower specific value of soot mass at EVO.

In the next six figures the distributions of six variables of interest, i.e., mass fractions of OH, C_2H_2, A_4, and soot, soot number density (PN) and particle size (D_p) are reported to analyze the causes of the observed soot emission trends.

Figure 5.6 shows that the in-cylinder OH concentration increases in the region behind the front flame and then start to decrease once the flame has reached the wall and the temperatures are falling. In the central region, near the spark-plug location, low OH concentration levels can be observed during the entire combustion process. At 20° ATDC, when the flame has reached the in-cylinder wall, the OH concentration is larger for the high-load case of 10% of oxygen.

The OH concentration is crucial for the soot oxidation process, while soot inception and surface growth depend on the in-cylinder concentration and distribution of the soot precursors. In Figure 5.7 and Figure 5.8 is therefore reported the time evolution of the mass fraction distributions of C_2H_2 and A_4, respectively, which are the most abundant gaseous hydrocarbon species detectable in regions where soot is formed. The highest values of their concentrations are recorded in the burned region, near the flame front and where the temperatures are lower, namely near the spark-plug location, in both cases. The mass fraction of these two species decreases after the flame, which is responsible for their production, reaches the cylinder wall and sufficient residence time at high temperatures is available in regions rich of OH radicals. In fact, at exhaust valve opening time (120° ATDC) these precursor species are mainly found near the center of the cylinder head due to the lack of OH radicals and the lower temperatures (Figure 5.7(c) and Figure 5.8(c)). With oxygen addition, a slightly larger amount of C_2H_2 and A_4 can be detected.

A competition between the increased concentration of species responsible for soot generation and, at the same time, of OH radicals, which contribute to its oxidation, explains the time evolution of the soot mass fraction reported in Figure 5.9. In other words, higher soot mass fractions are seen near the flame front regions, where the in-cylinder temperatures are higher and there is abundance of C_2H_2 and A_4, while in the burnt regions, the oxidation process by OH radicals starts to take place, and thus the soot mass fraction is reduced (Figure 5.9(a) and Figure 5.9(b)). Oxygen addition enhances this aspect, increasing the production rates of both OH radicals and soot precursor species and therefore, at 120° ATDC, the in-cylinder soot mass distribution obtained with oxygen addition is comparable to the baseline case. Since stoichiometric conditions were considered in both cases the soot mass per kg of fuel is lower for the oxygenated combustion case, as previously shown in Figure 5.5(c).

From Figure 5.10 and Figure 5.11 it is also possible to observe that at TDC, soot

particles with larger sizes are located near the front flame (Figure 5.11(a)), where the C_2H_2 and A_4 concentrations are higher, but the highest number density levels are recorded near the spark-plug location (Figure 5.10(a)), where the temperatures are not high enough for a fast soot inception and growth process. At 120° ATDC the largest part of the formed soot is composed of very fine particles.

These results are in perfect agreement with the experimental measured PSDs, shown in Figure 5.12(a) and which pointed out that the load increase obtained by oxygen addition did not affect the granulometric distribution of the particles emitted from the engine at 2000 rpm. Computed PSDs are reported in Figure 5.12(a). The agreement with the experiments can be considered to be very good for particles with sizes larger than 10 nm. The number of the finest particles is overestimated by the numerical model, but, as previously mentioned in Chapter 3, it must be considered that oxidation, which could occur in the exhaust, as well as physical soot transformation, i.e., due to the discharge process of the gases from the combustion chamber into the exhaust pipe, or due to temperature conditions changing along the exhaust line or within the instrument can have strong effect on nucleation mode particles. This may explain the lower value detected by the particle sampler device within the exhaust pipe [11].

5.5 Conclusions

The present study analyzed the effect of a load increase on gasoline SI engine combustion, by means pure oxygen addition. In particular, 5% and 10% by volume of additional oxygen was inducted with gasoline within the intake manifold to explore loads higher than the wide open throttle case. All the tests were performed at stoichiometric and steady state conditions and two engine speeds were investigated, namely 2000 and 4000 rpm.

In particular, 3-D Computational Fluid Dynamics simulations were performed and the numerical results were compared with experimental measurements. Such an approach provides additional basic information about oxygenated fuels and combustion, while avoiding still existing uncertainties relating to chemistry models.

The effect of oxygen addition was to speed up the combustion process and the induced increase in load was roughly linear with increased oxygen content. At 4000 rpm the effects were more evident than at 2000 rpm, because in the latter case it was necessary to delay the ignition timing to avoid knock in the experiments. Very good agreement was obtained for the low speed case, while some discrepancies, which are attributed to the absence of a crevice model, were found for the high speed case.

Further investigation on the combustion and soot formation processes was provided at 2000 rpm. Oxygen addition produced a faster burning velocity and higher in-cylinder temperatures. During the initial combustion stages, higher soot mass fractions were seen near the fame front regions, where the in-cylinder temperatures were higher and there was abundance of C_2H_2 and A_4. Afterwards, the oxidation process by OH radicals started to take place, and thus the soot mass fraction was reduced. At EVO (120° ATDC) soot was mainly found in the center of the cylinder head due to the lack of OH radicals and the lower temperatures that characterized this region. Oxygen addition

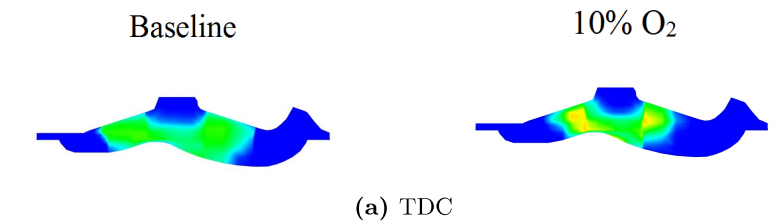

(a) TDC

(b) 20 CAD ATDC

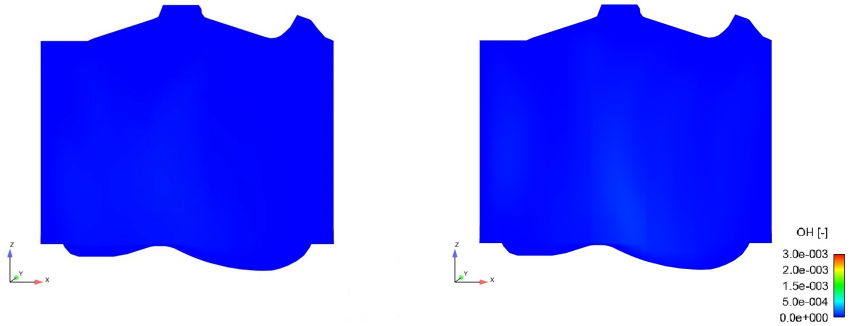

(c) 120 CAD ATDC

Figure 5.6: Time evolution of mass fraction distribution of OH radicals.

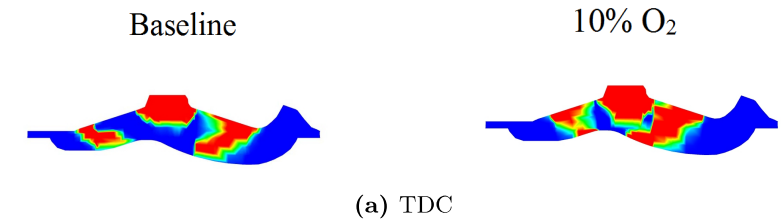

(a) TDC

(b) 20 CAD ATDC

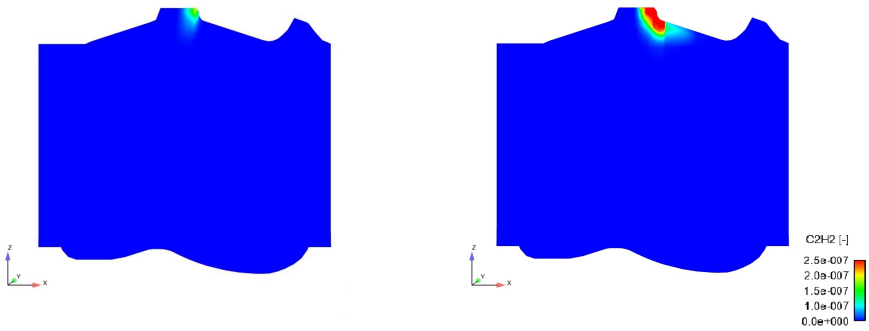

(c) 120 CAD ATDC

Figure 5.7: Time evolution of mass fraction distribution of C_2H_2.

(a) TDC

(b) 20 CAD ATDC

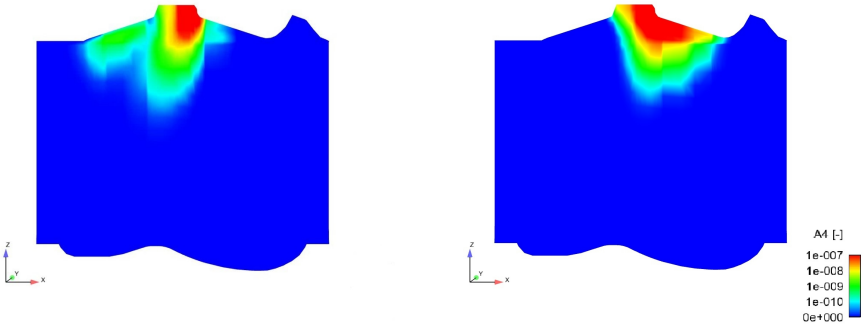

(c) 120 CAD ATDC

Figure 5.8: Time evolution of mass fraction distribution of A_4.

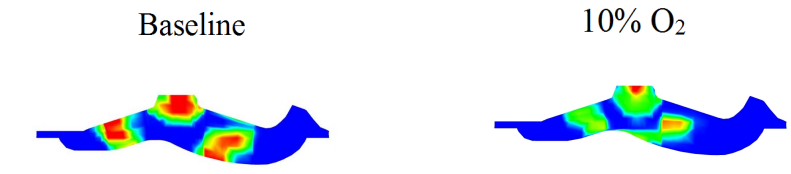

(a) TDC

(b) 20 CAD ATDC

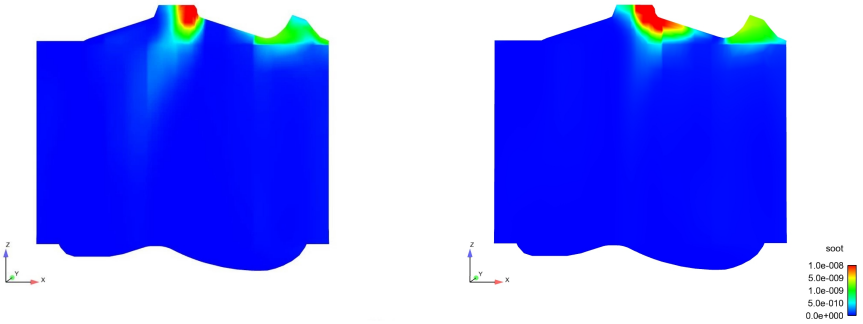

(c) 120 CAD ATDC

Figure 5.9: Time evolution of soot mass fraction distribution .

(a) TDC

(b) 20 CAD ATDC

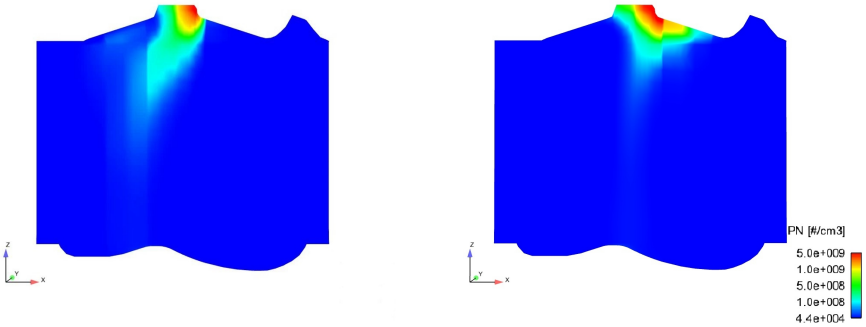

(c) 120 CAD ATDC

Figure 5.10: Time evolution of soot density number distribution.

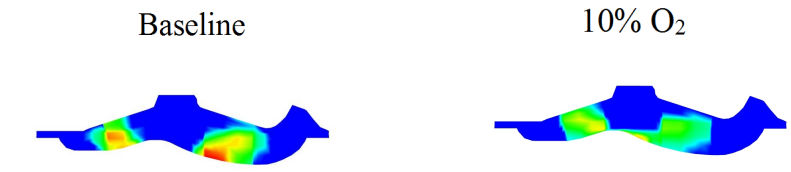

(a) TDC

(b) 20 CAD ATDC

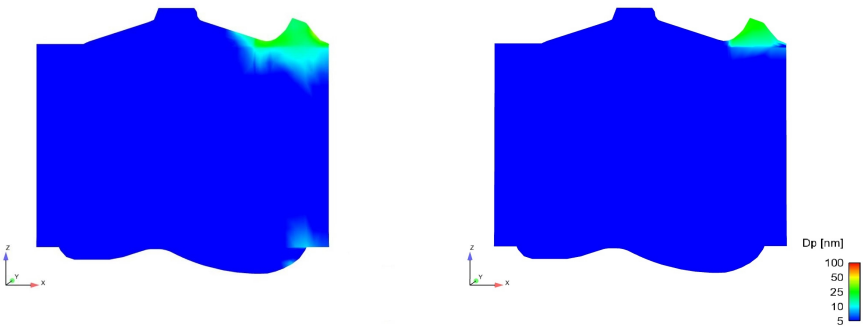

(c) 120 CAD ATDC

Figure 5.11: Time evolution of soot particle sizes distribution.

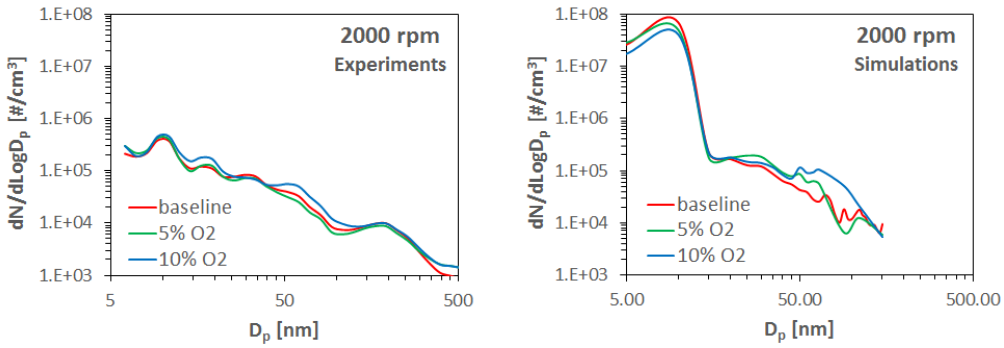

(a) (b)

Figure 5.12: Experimental (a) and predicted (a) PSD functions.

enhanced this aspect, increasing the production rates of both OH radicals and soot precursor species and therefore, at 120° ATDC, the in-cylinder soot mass distribution obtained with oxygen addition was comparable to the baseline case. However, since stoichiometric conditions were considered in both cases the soot mass per kg of fuel was lower for the oxygenated combustion case.

The numerical results were in good agreement with experimentally measured PSDs and provide confidence in the soot model in predicting soot emissions. In addition, the comparison between measured and predicted PSDs showed very good agreement for particles with sizes larger than 10 nm, but the number of the finest particles was overestimated by the numerical model, in a similar way shown in Chapter 3. Therefore, this can be explained by considering oxidation process occurring in the exhaust, which was not considered in the simulations. The implementation of a crevice model will allow to obtain even better agreement with the experimental data.

Influence of Natural Gas Composition 6

This Chapter provides experimental investigations aimed to investigate the influence of natural gas composition on combustion in a single-cylinder Spark-Ignition engine. Natural gas represents one of the most concrete alternatives to replace traditional fuels, especially for heavy-duty engines. Therefore, the need to increase its performance and at same time reduce its emissions for even cleaner engines will became soon stronger and thus operate on its composition could represent an interest and practical solution. In the present experimental tests, Methane/propane mixtures were realized to isolate the effects of a variation of the main constituents in natural gas on engine performance and associated pollutant emissions. The propane fraction was varied from 10 to 40%. The results were compared with pure methane and propane, as well as with natural gas. An innovative experimental procedure to obtain precise real-time mixture fractions injected directly into the intake manifold was designed and validated.

6.1 Introduction

Nowadays, homogeneous charge Spark-Ignition (SI) engines fueled with Compressed Natural Gas (CNG) are gradually replacing diesel powered vehicles in large transport fleets [171, 172]. For example, over the past eight years, 50% of the transport bus fleet in Brisbane, Australia, has been gradually converted from diesel to CNG. In New Delhi, India, one of the most polluted cities in the world, the entire transport fleet was converted to CNG in 2003 resulting in some improvement in air quality in terms of suspended particulate matter, CO, SO_2, and NO_x [171, 173].

One issue that recently has been addressed in both fundamental and applied studies is that a variation in the fuel composition can have non-negligible effects on the combustion process [12, 13, 18–24]. In fact, natural gas is a mixture of various hydrocarbon molecules: the principal component is methane and its compositions can vary from 55.8% to 98.1%; the main heavy hydrocarbons present in natural gas are ethane, which can vary between

0.5% and 13.3%, and propane, in amounts varying between 0% and 23.7% [174]. Diluents such as N_2 and CO_2 are also present in significant fractions. There are also trace levels of sulphur compounds, often added as odorants, and hydrocarbons larger than C_3 [13]. The components concentration change with geographical source, time of year, and treatments applied during production or transportation [17].

Commonly, the Methane Number (MN) is used for quantify the anti-knock properties of natural gas related to its composition. MN is derived experimentally and a 100% methane composition gives MN=100 and as the higher hydrocarbons percentage increases, MN decreases. MN of various natural gas compositions can vary considerably, causing possible knock events in some engines [175].

Previous studies have shown that changes in natural gas composition can impact emissions, as well as engine performance [16, 171–173]. Karavalakis et al. [176] reported that natural gases with higher heating value exhibited higher fuel economy on an energy equivalent basis. Higher flame speeds and higher adiabatic flame temperatures can be obtained with larger amounts of ethane and propane in natural gas, producing more efficient combustion [13, 176, 177]. A reduction in Total Unburned Hydrocarbon (TUHC) emissions was seen for fuels with higher hydrocarbon contents [12, 13]. Some researchers report increases in TUHC emissions with increased ethane and propane concentration [178], although these results are not consistent with other previous studies. NOx emission levels were clearly influenced by the fuel composition, with low MN natural gases resulting in higher NO_x emissions [12, 13, 20, 21, 176]. McTaggart-Cowan et al. [13] suggested that it was due the increased adiabatic flame temperature with a higher fraction of ethane and propane, since NO_x are generated predominantly through the strongly temperature-dependent thermal NO mechanism [31]. They found that a 1% change in adiabatic flame temperature resulted in a 5% change in NO_x emissions. CO is another combustion by-product that is sensitive to fuel composition, but discordant results have been reported in literature [13, 176].

Furthermore, current emission regulations emphasize the need to control greenhouse gas emissions from on-road sources, and consequently there is a need to control methane, as well as CO_2 emissions, from natural gas vehicles [179]. Methane is not toxic and not relevant to ozone-forming potential, but it shows a global warming potential 25 times higher than CO_2 [12]. In general, higher methane emissions were recorded for higher MN fuels [12] and this might be due to the fact that methane is less reactive than higher chain hydrocarbons, so it is more likely that higher amounts survive the combustion process [180]. Higher CO_2 emissions were recorded for natural gases having higher fraction of higher hydrocarbons [176].

McTaggart-Cowan et al. [13] found that relatively high levels of ethane and propane in natural gas can significantly increase Particulate Matter (PM) emissions. In such a study, both black carbon and volatile PM emissions were claimed to be increased by an increase in ethane and propane contents, and other studies have confirmed this trend [18]. The presence of hydrocarbons with longer chains or more complex structures can enhance PM precursor formation in the reaction zone [181, 182], including C_2 species, such as the ethyl radical (C_2H_5) and acetylene (C_2H_2) [18] which are the most abundant gaseous hydrocarbon species in regions where soot is formed in laminar premixed flames [11, 88].

There is a lack of information about the effect that a variation of natural gas composition can produce on Particle Number density (PN) and Size Distribution (PSD) functions. Karavalakis et al. [12] recently reported some measurements, but a clear and exhaustive understanding of the phenomenon is still needed. Therefore, substantially more work is required to understand the effects of the heavier hydrocarbons on particle formation in natural gas engines.

The present study aims to isolate the influence that heavier hydrocarbons have on natural gas combustion. For this purpose, propane addition to pure methane was studied. Among the hydrocarbons present in a relevant amount within natural gas, propane (more than ethane) has thermochemical and combustion properties that are similar in to those of more complex practical fuels [110]. Therefore, it was thought that variations in its concentration would produce more appreciable effects on particulate emissions than those produced by ethane. In addition, propane is used more often than ethane in many combustion applications and laboratory studies [144]. Accordingly, an innovative experimental procedure was designed and validated in order to quantify real-time methane/propane fuel mixtures directly within the intake manifold. Steady-state engine performance and emissions were therefore evaluated considering different amounts of propane in methane. Experiments with pure methane, pure propane and natural gas were also performed and compared.

6.2 Experimental method

Apparatus

The experimental apparatus included:

- a single cylinder SI engine;
- an electrical dynamometer;
- the methane and propane injection lines;
- two single-hole gas injectors;
- the data acquisition and control units;
- four emission measurement systems;

The engine was fueled with pure methane and propane, as well as with their mixtures and with CNG. Methane had a purity expressed in a decimal fraction equal to 3.5 and that of propane was 2.5. The natural gas composition is reported in Table 6.1, as provided by the suppliers.

Engine

A 4-stroke, single cylinder, SI engine with specifications shown in Table 6.2 was used in the experiments. The spark-plug was centrally located in the engine head. A modified intake manifold was employed to fit two single-hole gas injectors, allowing a simultaneous double port fuel injection. The engine was equipped with a Three-Way Catalyst (TWC) and it was water cooled.

Table 6.1: Natural gas chemical composition.

Name	Fraction
Carbon dioxide (CO_2)	1 %
Nitrogen (N_2)	2 %
Methane (CH_4)	88 %
Ethane (C_2H_6)	7 %
Propane (C_3H_8)	2 %

Table 6.2: Engine specifications.

Name	Units	Value
Cylinder volume	cm^3	250
Bore	mm	72
Stroke	mm	60
Compression ratio	None	10.5
Max power	kW	16 at 8000 rpm
Max torque	Nm	20 at 5500 rpm

Emission measurement systems

Gaseous and particulate emissions were measured by sampling directly from the exhausts, shortly after leaving the cylinder.

CO, CO_2 were measured by means of non-dispersive infrared detectors; NO_x emissions were detected by means of electrochemical sensors. UHCs were measured by means of a Flame Ionization Detector, which also allowed separation of the methane content.

PN concentrations and sizes were measured in the range from 5 to 560 nm by means of a TSI Engine Exhaust Particle Sizer. The exhausts were sampled and diluted with air heated at 150 °C . The dilution ratio was fixed at 1:10. A 1.5 m heated line was used for sampling the engine exhausts in order to avoid condensation of combustion water. A Volatile Particle Remover (VPR) was not used in this analysis in order to take into account all types of particles and not only the solid ones, defined by the Particle Measurement Programme [168] as the particles that can survive passing through the VPR.

In addition, Opacity [%] was continuously measured by an AVL 439 Opacimeter sampling downstream the TWC.

6.3 Experimental procedure

The tests were designed to investigate the effect of natural gas composition on engine performance and emissions. In particular, the goal consisted of isolating the influence that propane has on methane combustion.

Engine performance and emissions were evaluated when the engine was fueled with pure methane and pure propane, as well as with four different mixtures, having

respectively 10, 20, 30 and 40% by volume of propane in methane. Experiments with natural gas were also performed and compared. All the tests were performed at steady state conditions. For a more extensive analysis, three different engine speeds were investigated, namely 2000, 3000 and 4000 rpm. Stoichiometric conditions were considered in all tests. To ensure proper operation and reliable response of the exhaust gas analyzers, the engine was first warmed up and the data were recorded only after engine conditions were stabilized. Tests were repeated three times in order to provide good statistics of the measurements and each test was averaged over 300 consecutive cycles.

The in-cylinder pressure was measured by means of a quartz pressure transducer flush-mounted in the region between the intake and exhaust valves. It measures the in-cylinder pressure with a sensitivity of 16.2 pC/bar and a natural frequency of 130 kHz. The sensor signal was recorded by a flexible data acquisition system equipped with 8 high speed analogue inputs. The signals were post-processed by indicating software, which allowed the calculation of combustion parameters, such as IMEP, the Coefficient Of Variation (COV), the Duration of Combustion (DOC) and HRR, as well as MBF5%, MBF50% and MBF90%.

Real-time fuel mixtures

An innovative experimental procedure was designed and validated to realize real-time methane/propane fuel mixtures. Two single-hole gas injectors were used to simultaneously inject two gaseous fuels within the intake manifold. An accurate control strategy, together with proper design of the injection lines, allowed precise mixture fractions and satisfactory mixing.

Figure 6.1 shows a schematic representation of the experimental set-up used for the mixture tests. The two gaseous fuels were supplied by pressurized bottles. Two surge tanks (numbers (3) and (4) in Figure 6.1) were used to absorb sudden changes in pressure due to propagating waves generated during the injection phases. This allowed stable measurements of the static injection pressures and temperatures for both gases. By means of two pressure regulators the injection pressure was set to 5 bar, a value that established choked flow conditions through both the injectors for all the operating conditions considered. The two fuels were injected by employing two identical single-hole injectors (numbers (5) and (6) in 6.1).

If choked flow conditions are ensured, the average value of the mass flow rate injected, $\dot{m}_i$, is estimated by using the following expression:

$$\dot{m}_i = A_{inj} \frac{p_i^0}{\sqrt{R_i T_i^0}} \sqrt{\gamma_i} \sqrt{\left(\frac{2}{\gamma_i + 1}\right)^{\frac{\gamma_i+1}{\gamma_i-1}}} \frac{f_{inj}}{f_{inj}^{ref}}, \tag{6.1}$$

in which A_{inj} is the nozzle cross section area of the injector, p_i^0 and T_i^0 are the total pressure and temperature, respectively, γ_i is the specific heat ratio, R_i the specific gas constant. The subscript i refers to the specific gas considered. The term f_{inj}/f_{inj}^{ref} represents the ratio between the injection frequency and its reference value (in this case $f_{inj}^{ref} = 33.33$ injection per second) and it takes into account the fact that the injector

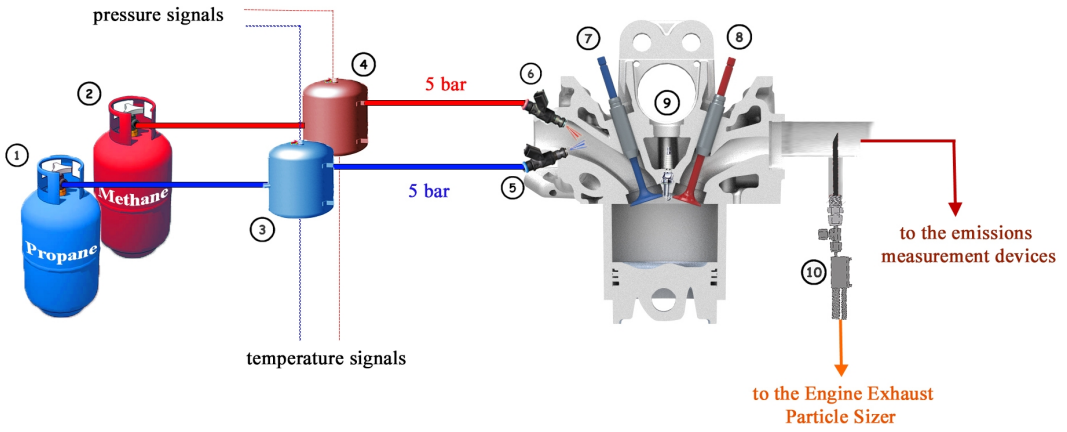

Figure 6.1: Experimental Set-up used for the methane/propane mixtures tests. (1) Propane bottle; (2) Methane bottle; (3) Propane surge tank; (4) Methane surge tank; (5) and (6) 1-hole gas injectors; (7) intake and (8) exhaust valves; (9) spark-plug; (10) particle sizer probe.

does not work continuously during the engine cycle, namely injecting for the same time at two different engine speeds produces two different average values of the fuel mass injected per second.

However, Equation (6.1) needs to be corrected in order to take into account the mechanical delay that an injector intrinsically shows. Considering that the Duration Of Injection (DOI) is small for both gasses, the injection inertia assumes a great importance and cannot be neglected for obtaining accurate results. Therefore, with the aim to quantify the effect that the mechanical delay produces on the injected flow rate, the injector was characterized by using nitrogen injected at 3.5 bar.

Figure 6.2(a) shows that when the DOI is short the mass flow rate injected is significantly less than the expected value. In such a graph, the value $\Gamma = \left(f_{inj}^{ref}/f_{inj}\right)\dot{m}_{meas}$ is plotted (where $\dot{m}_{meas}$ is the measured mass flow rate). Figure 6.2(b) quantifies the deviation from the linearity due to the injector mechanical delay and highlights its importance. Figure 6.2(b) also shows that the deviation can be represented by an exponential curve having the form $-a\Delta t^{-b}$, where Δt is the DOI expressed in ms and the constants a and b assume values equal to 0.754 and 1.398, respectively. In addition, Figure 6.2(a)) shows that the injection frequency does not have relevant influence and additional experiments demonstrated that the injection pressure does not affect the results in an appreciable way as well.

Equation (6.1) can be therefore rewritten as:

$$\dot{m}_i = A_{inj}\frac{p_i^0}{\sqrt{R_i T_i^0}}\sqrt{\gamma_i}\sqrt{\left(\frac{2}{\gamma_i+1}\right)^{\frac{\gamma_i+1}{\gamma_i-1}}\frac{f_{inj}}{f_{inj}^{ref}}\left(1-a\Delta t_i^{-b}\right)}\,. \tag{6.2}$$

From Equation (6.2) it is possible to calculate the ratio between the DOIs of methane and propane $\Delta t_{CH_4}/\Delta t_{C_3H_8}$ from the methane-to-propane mass ratio, which is easily calculable from the desired mixture volume fractions. In order to ensure stochiometric conditions in all the tests, a constant monitoring and properly adjustment of the two

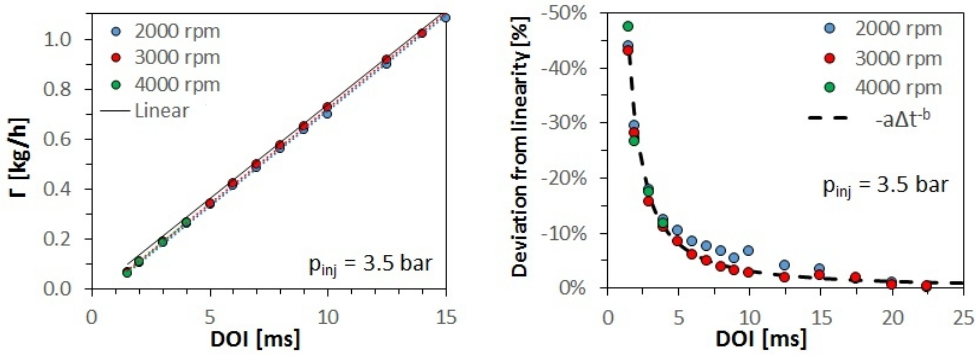

(a) (b)

Figure 6.2: Measured mass flow rate $\Gamma = \frac{f_{inj}^{ref}}{f_{inj}} \dot{m}_{meas}$ (a). Deviation from linearity due to injector mechanical delay (b).

DOIs (by keeping their ratio constant) was realized by means of closed loop control based on the lambda value. A linear lambda sensor Bosch LSU 4.9 was used to measure the air-to-fuel ratio. A programmable electronic control unit allowed the management of the combined injection timing.

Mixing procedure validation

The procedure was validated by analyzing the obtained mixtures with the flame ionization detector during motoring conditions. The sample was properly diluted to meet the instrument working range. In this way it was possible to check if the composition of the obtained fuel blends corresponded to that which was expected. The results are shown in Figure 6.3. The use of Equation (6.2) (green symbols) gave more than satisfactory results. It was confirmed that the injector's mechanical delay needs to be considered in calculations by comparing the results obtained with Equation (6.1) (red symbols in Figure 6.3). In the latter case, the injected mass of propane was overestimated more than that of methane, giving a lower fraction of propane in the resulting mixture. This because the DOI for propane was shorter than for methane and the effects of the injector inertia were stronger (see Figure 6.2(b)).

Finally, to ensure proper mixing of the two gasses within the intake manifold, it was chosen to inject twice per cycle. This strategy ensured to longest time possible for the mixing process, and turbulence within the intake ducts helped the process. The measurements depicted in Figure 6.3 never showed a deviation of the recorded value larger than 0.5%, giving confidence that the mixing process was satisfactory. In addition, performance and emissions measurements (reported in next sections) did not show any appreciable fluctuations attributable to possible not-perfect mixing.

6.4 Results and discussion

In the next sections the effect of propane addition to methane on engine performance is first described. Then, the influence on regulated and greenhouse gas emissions is

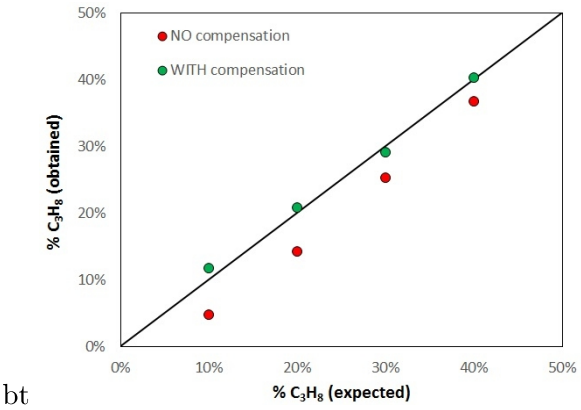

bt

Figure 6.3: Expected vs obtained propane fraction. Red marks refer to $\Delta t_{CH_4}/\Delta t_{C_3H_8}$ calculated by using Equation (6.1), while green marks refer to $\Delta t_{CH_4}/\Delta t_{C_3H_8}$ calculated by using Equation (6.2)

illustrated. For the various methane/propane mixtures the nomenclature P10, P20, P30 and P40 is used in the next section, where the number denotes the propane volume fraction in the mixture.

Engine performance

Varying the fuel composition had a significant influence on the combustion event and therefore on the engine performance. These influences are summarized in Figure 6.4 and in Figure 6.5, where the in-cylinder pressure traces, and HRR, IMEP, COV and DOC are represented for each of the engine speeds considered.

Since propane has a faster burning speed than methane [22, 111, 144], it was found that as the mixture was ignited the in-cylinder pressure increased faster when propane was added to methane for all engine speeds, as shown in Figure 6.4. The larger the propane fraction in methane, the higher was the obtained pressure-peak, as well as the higher was the HHR-peak, which means that a larger amount of energy was released in the initial combustion phases. This is also appreciable from the progressively lower MBF5% values obtained adding propane. This behavior can be explained by considering that, in addition to a faster burring velocity, propane also features a chemical structure that allows it to be ignited easier. For alkane fuels heavier than methane, the initiation reactions occur mainly through the breaking of a C-C bond since the C-H bond has a much higher bond dissociation energy. The longer the chain, the easier is its breaking into smaller intermediate hydrocarbons and chain propagating radicals [23].

Figure 6.5(a) and 6.5(b) show that for all mixtures and conditions, the effect of propane addition was to increase the IMEP and, at the same time, to reduce the COV. In other words, propane presents a more stable and efficient combustion process than methane and therefore, even when small amounts of it are added to methane, it is possible to appreciate beneficial effects on engine performance.

The fact that propane addition speeds up the combustion process is also visible in Figure 6.5(c) when the cases of 3000 and 4000 rpm are considered. The graphs report the values of the DOC, calculated as the difference between the CADs corresponding to

MBF90% and MBF5%.

Contrariwise, when the engine run at 2000 rpm the DOC increased slightly with gradual propane addition. This means that the ending phase of the combustion process was not as fast as the initial one for propane mixtures, as can be inferred from the HRR traces at 2000 rpm in Figure 6.4. This can be attributed to the fact that, once the flame reaches the cylinder walls, the combustion is completed in the absence of a propagating flame and depends on only chemistry. In the last phase of combustion most likely the conversion reactions from CO to CO_2 are taking place, which are commonly considered the slowest part of the oxidation process. In the case of propane and its mixtures the flame reaches the cylinder walls earlier than methane and therefore the ending part of the combustion assumes more relevant importance. At higher speeds the flame reaches the cylinder walls later and furthermore the final oxidation process is enhanced by the increased turbulence.

Natural gas recorded in-cylinder pressure and calculated HRR traces, as well as MBF5% values (Figure 6.4), were in-between those of the two pure compounds and, in particular, they were close to the case with a propane fraction in methane equal to 20% (the natural gas contained appreciable ethane, which has a faster flame speed than propane [22, 111, 144]). However, the presence of diluents, such as nitrogen and CO_2(Table 6.1), explains why the recorded values of IMEP (Figure 6.5(a)) were comparable to or lower than those obtained when the engine was fueled with pure methane. The presence of the small fraction of heavier hydrocarbons ensured, for the aforementioned reasons, lower values of COV (Figure 6.5(b)) and DOC (Figure 6.5(c)) than for pure methane.

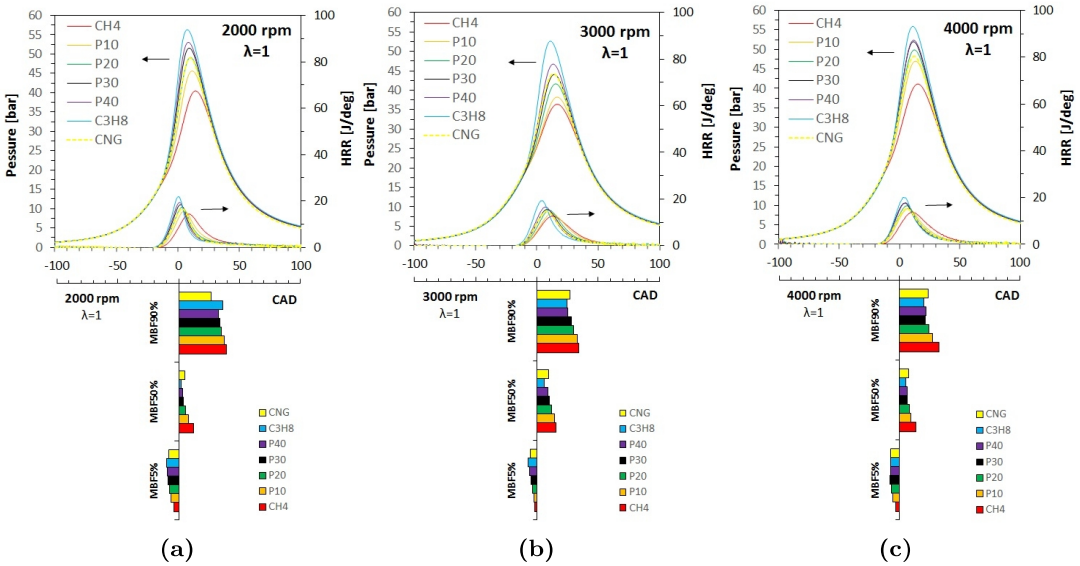

Figure 6.4: In-cylinder pressure, HRR, MBF5%, MBF50% and MBF90% for the three different engine speeds investigated.

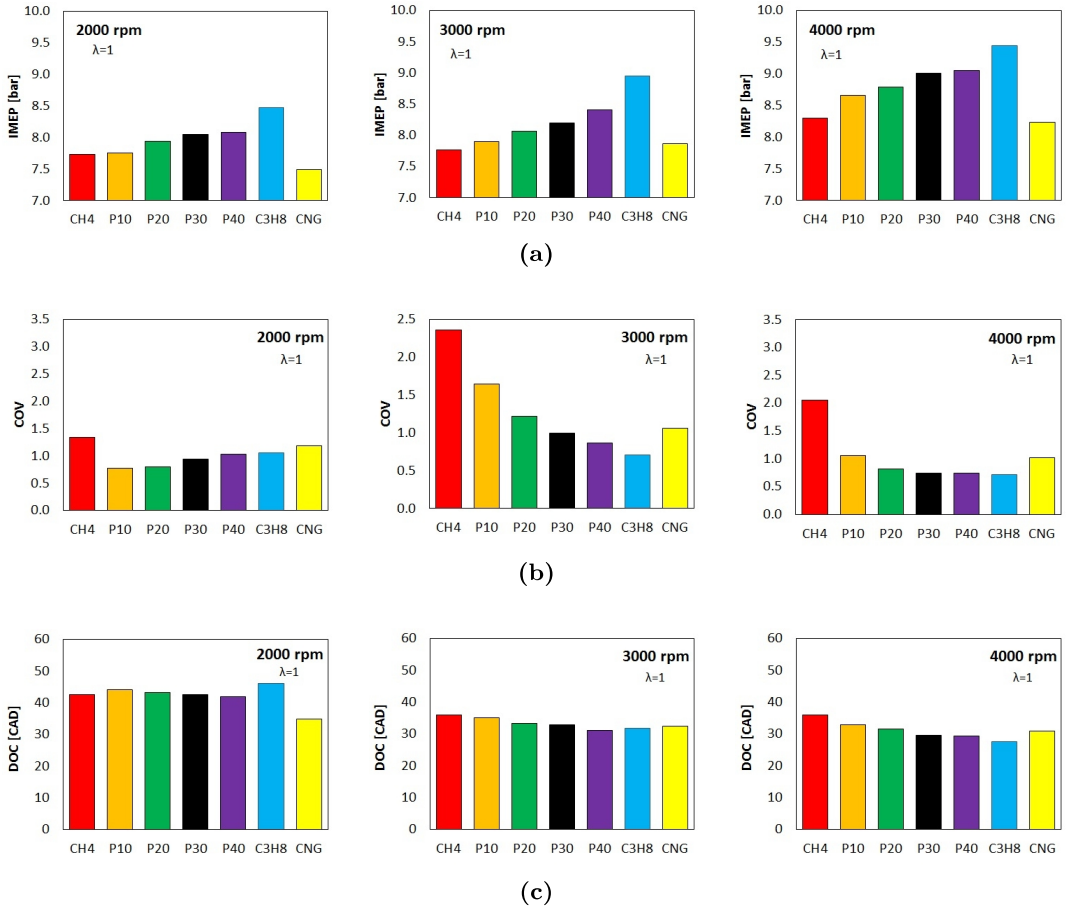

Figure 6.5: IMEP (a) COV (b) and DOC (c) for the three different engine speeds investigated.

Regulated and greenhouse emissions

The values recorded for regulated and greenhouse emissions are reported and the error bars on the graphs represent the standard deviation of the measurements. The UHC emissions are reported in Figure 6.6 for the three different engine speeds investigated. For methane, the great part of UHC emissions was predominantly Methane Unburned Hydrocarbons (MUHC). Analogous behavior was recorded for natural gas, since methane is its main constituted. However, the TUHC level was higher than pure methane and this can be attributed to the presence of heavier hydrocarbons within the natural gas. The recorded value of MUHCs decreased as the propane content in methane/propane mixtures was increased, while, even though the non-methane part increased, the TUHCs decreased when propane was added. The fastest combustion process, together with the higher temperature reached with the presence of propane favors a more complete combustion, explaining the obtained results, that are in agreement with previous studies [12, 13, 176, 177].

The more complete conversion of fuel into CO and CO_2 can also explain their gradually increased values with an increase of propane concentration, as shown in Figure 6.7. This agrees with the interpretation that the UHC emissions are primarily unreacted fuel, while the CO is a by-product of partial combustion [13]. When natural

gas is burned the conversion rate into CO is increased by the heavier hydrocarbons, while the presence of diluents slows down the final conversion process of CO into CO_2.

Figure 6.7 also shows that the NO_x emissions tend to be one of the most sensitive to combustion conditions. When the engine is fueled with propane, higher temperatures are reached within the combustion chamber, due to its higher adiabatic flame temperature than methane. Therefore, higher levels of NO_x are expected. Also, the presence of propane and ethane, as well as of heavier hydrocarbons in the natural gas promotes the formation of reactive radicals, resulting in an increased formation of prompt NO_x [17]. This explains both the highest value recorded for pure propane and the intermediate values recorded for natural gas. The present results agree with previous studies that have reported higher NO_x emissions with low MN fuels [12, 13, 20, 21, 176].

The case of 3000 rpm exhibited the lowest NO_x levels in comparison to the other two engine speeds for all considered fuels. It must be noted that this case showed the highest levels of COV (Figure 6.5(a)), symptomatic of higher combustion instability compared to the other cases, probably due to particular turbulence conditions that characterize the test engine. As a consequence, the recorded in-cylinder pressure peaks were lower (Figure 6.4) and therefore lower temperature were reached, explaining the lower NO_x levels.

Measured PSD functions are depicted in Figure 6.8. In all tests, natural gas showed the highest values of particles emitted by the engine, which resulted in the highest total PN levels shown in Figure 6.9(a). At 2000 rpm, the difference between the methane/propane mixtures were small, although with 40% of propane in methane and more clearly with pure propane, particles with size between 15 and 30 nm started to become predominant and the distribution assumed a shape very similar to that recorded for natural gas.

There are other evidences in the literature that correlate an increase in soot emissions with an increase in ethane and propane content in natural gas [13, 18], and this behavior is commonly attributed to enhanced soot precursor formation in the reaction zone, such as C_2H_2 and C_2H_5, which are important intermediates in the chemical reaction path generated in the combustion of heavier hydrocarbons.

When the engine speed is lower, more time is available during the expansion stroke for oxidation, which is also enhanced by the higher temperatures reached with the presence of propane. Thus, if a larger amount of soot was generated with slightly

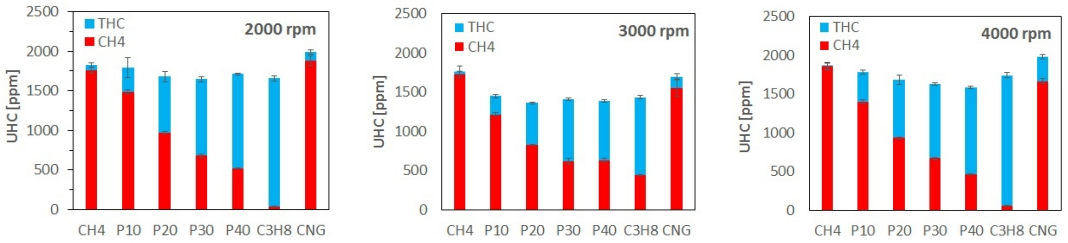

(a) (b) (c)

Figure 6.6: TUHC (blue bars) and MUHC (red bars) emissions for the three different engine speeds investigated.

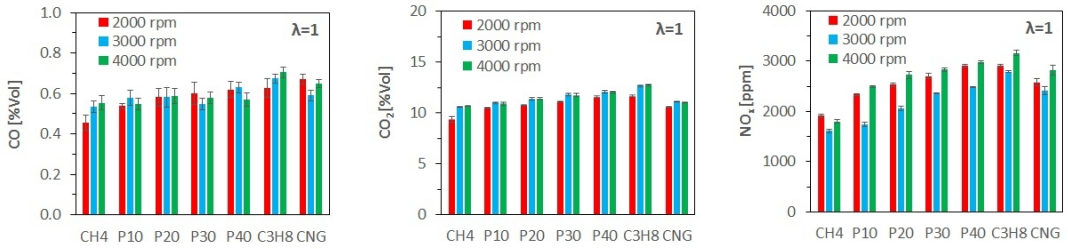

(a) (b) (c)

Figure 6.7: CO, CO_2 and NO_x emissions for the three different engine speeds investigated.

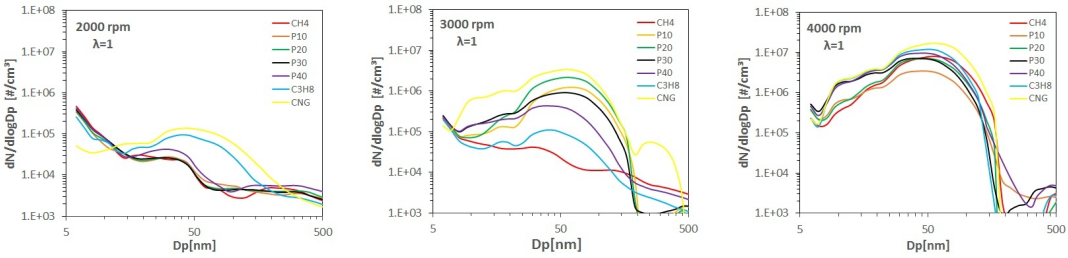

(a) (b) (c)

Figure 6.8: PSD functions for the three different engine speeds investigated.

increased amounts of propane in methane, it was also oxidized faster, resulting in a final level that was comparable to that detected for pure methane.

Increasing the engine speed resulted in a general increase in the number of particles emitted. At 4000 rpm, increasing the propane content produced an increase in the number of particles below 30 nm. This is a relevant result considering that in Euro VI heavy duty emission regulations, only non-volatile particles over 23 nm are taken into account [168].

What appears noticeable is the fact that mixtures with a smaller amount of propane generated a lower number of particles near the distribution peak, namely 50 nm, resulting in a lower total PN value (Figure 6.9(a)). This might be due to the fact that small amounts of propane can increase the mixture's oxidation ability more than its soot tendency. However, the number of particles with the finest dimension were always increased with an increase of propane fraction.

In the central graph of Figure 6.8 is plotted the intermediate case of 3000 rpm. It shows a different behavior from both the two previous cases, and this could be mainly attributable to the above-mentioned turbulence conditions that characterize this engine speed. This highlights the sensitivity of the soot formation process to the thermo-physical combustion conditions. It was confirmed that the highest number of particles were emitted by the natural gas combustion and the lowest by that of methane. A gradual increase of propane fraction in methane first produced an increase in PN and then, for larger fractions, a decrease, as shown in Figure 6.9(a). The particles with size of about 50 nm showed the greatest sensitivity to these conditions (Figure 6.8).

The trends recorded by the spectrometer were confirmed by opacity measurements

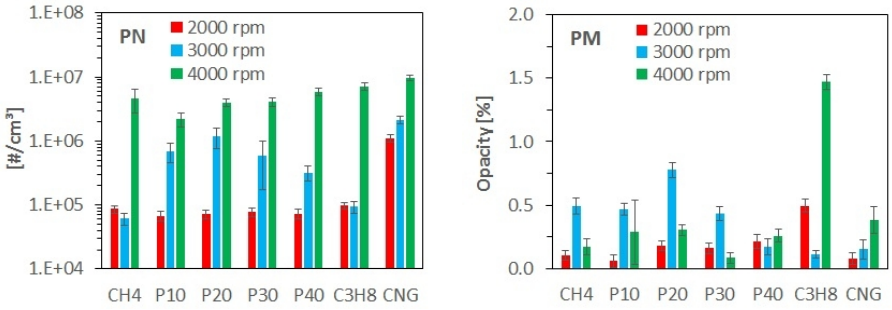

Figure 6.9: PN (a) and PM (b) for the three different engine speeds investigated.

of soot mass, and the results are reported in Figure 6.9(b). However, some differences can be highlighted, e.g., the recorded values for natural gas were lower than propane and the highest opacity values were recorded at 3000 rpm. These discrepancies could be due to the following reasons: first, the opacity samples were collected downstream the TWC to avoid interference between the various instrument probes. Second, only the largest particles can be efficiently measured by the opacimeter device. In addition, the recorded values were close to the lower detection limit of the instrument.

6.5 Conclusions

This Chapter presented experimental results concerning the influence that variations in natural gas composition can have on the performance and emissions of a single-cylinder SI engine. In particular, the work focused on the effects generated by a modification in the heavier hydrocarbons content. To pursue this aim, propane addition to pure methane was studied.

An innovative experimental procedure was designed and validated to realize real-time methane/propane fuel mixtures directly within the intake manifold. To ensure the proper mixing of the two gases, two injections per cycle were adopted. Experiments with pure methane, pure propane and natural gas were also performed.

For all mixtures and conditions, the effect of propane addition was to increase the IMEP value and, at the same time, to reduce the COV, resulting in more stable and efficient combustion than pure methane.

Natural gas recorded in-cylinder pressure and calculated HRR traces were close to the P20 (20% propane in methane) case. However, the presence of diluents, such as nitrogen and CO_2, explained why the recorded values of IMEP were comparable or lower than those of pure methane. The presence of a small fraction of heavier hydrocarbons ensured lower values of COV and DOC than pure methane.

The recorded value of MUHCs (unburned methane) decreased as the propane content in methane/propane mixtures was increased, while, even though the non-methane part increased, the TUHCs (total) decreased when propane was added. The faster combustion process, together with higher temperatures obtained with the presence of propane favor more complete combustion, which can also explain the increased values of CO_2, as well

as the higher levels of NO_x. For natural gas the conversion rate into CO is increased by the heavier hydrocarbons, while the presence of diluents results in a slower conversion process of CO into CO_2. The enhanced formation of reactive radicals due to the heavier hydrocarbons explains the higher NO_x emissions recorded in comparison to pure methane.

In all tests, natural gas showed the highest PN values. Increasing the engine speed resulted in a general increase in the number of particles emitted. At 4000 rpm, increasing the propane content produced an increase in the number of particles between 5 and 30 nm, highlighting the relevance of the ultra-fine range in the particle emissions emitted from natural gas engines. An interesting result was that, at the highest speed, mixtures with a small amount of propane generated less particles near the distribution peak, namely 50 nm, resulting in a lower total PN value. Larger differences in PSDs were detected at intermediate speeds and this was attributed to the engine turbulence at this condition, which also exhibited the highest COV values. This highlights the sensitivity of the soot formation process to the thermo-physical conditions occurring within the combustion chamber. Opacity measurements of PM generally confirmed the detected trends.

In the future the need for even cleaner and better performing engines will need to increase natural gas performance and at same time reduce its emissions. Controlling its composition with addition of hydrocarbons and diluents content could represent a solution. Therefore, further investigations are needed in which different conditions in terms of equivalence ratio, and energy content of the fuel are of interest. The effect of varying natural gas additives should be considered as well. In addition, it is crucial to perform studies in which the fuel composition contribution to particle emissions is separated from that of lubricant oil, which is known to be a major sources of PM in natural gas engines and can affect the results, since lubricating oil-originated hydrocarbons and sulfur compounds can magnify the existing particles in the dilution and cooling process.

7 Role of Lubricant Oil

The influence of engine lubricant on particulate emission is still unclear, so that elucidating the mechanisms of oil-derived soot formation can play an important role towards reducing fuel-derived particulate emissions and may be very important in developing new lubricant oil formulations too. This Chapter presents experimental tests where lubricant oil was added to the engine in order to highlight the contribution of lubricant oil to particle emissions on both gasoline and Compressed Natural Gas SI engines. Three different ways of feeding the extra lubricant oil and two fuel injection modes – Port Fuel Injection (PFI) and Direct Injection (DI) – were investigated to mimic the different ways by which lubricant may reach the combustion chamber. In particular, in the tests using CNG, the oil was injected either into the intake manifold or directly into the combustion chamber, whereas in both the PFI and DI tests using gasoline, the oil was premixed with the fuel. The experiments were performed on a single-cylinder, optically accessible SI engine requiring no lubrication.

7.1 Introduction

Engine lubricant oil is composed of a base oil and an additive package. In general, the base oil is composed of petroleum-derived mineral oils, whereas the additive package is composed of various chemicals, including metal compounds (such as Ca, Ba, Mg, Fe, Ni, Mn, Cu and Zn) [183, 184]. That means that metals traces derived from the lubricant oil can be found in the exhaust of both SI and Diesel engines [40, 185–187]. This aspect emphasizes the need of providing more insight into lubricant oil contribution to particle emissions since health hazard produced by exposure to particles has been shown to increase with the content of metals in nanoparticles [188–190]. Moreover, PM-induced toxic activity of exhausts is strongly associated with traces of lubricant oil emissions, such as Zn, P, Ca, suggesting that the incomplete combustion of lubricant oils leads to increased health risks [186].

The early studies about the oil contribution to the particle emission were focused on modern Diesel engines, in which the oxidation catalyst reduces some of the organic fraction of lubricant oil PM, and the Diesel Particulate Filter (DPF) abates some of the inorganic fraction (soot and metals) of the lubricant oil PM [40]. A study by McGeehan et al. [185] has shown that the ashes deposited in the DPF of a Diesel engine are predominantly inorganic and dominated by lubricant oil additives. In the case of SI engines, the contribution of lubricant oil to tailpipe PM could be significant, because although the Three-Way Catalyst (TWC) will oxidize the organic fraction of the PM, there is no DPF to remove the inorganic fraction of the PM consisting of soot and trace metals [40].

In addition, several studies [191–193] have shown that metal additives may reduce the accumulation mode while increasing the nucleation mode in Diesel engines. A study by Jung et al. [194] showed that metals in lubricant oil blended with fuel might play a similar role. In their experiments, the authors investigated the influence of metals on soot oxidation and particle emissions in Diesel engines using lubricant oil-dosed fuel (2% by volume). PSD measurements showed that particle volume emissions, which are roughly proportional to particle mass, decreased by about a factor of two with dosed fuel, whilst PN emissions increased by an order of magnitude. Most of the PN was found in tiny, solid nuclei-mode particles below 30 nm.

Miller et al. [195] demonstrated that the metal traces emitted by SI engines are derived mainly from combustion of lubricant oil by using a CAT 3304 Diesel modified-engine fueled with hydrogen gas. Modifications included lowering the compression ratio of the engine and equipping it with a SI system and a turbocharger with aftercooler. The results showed that the engine produced exhaust aerosol with log normal-size distributions with geometric mean diameters from 18 to 31 nm. The particles contained organic carbon, little or no elemental carbon, and a much larger percentage of metals than particles from the original engine. These results indicate that the findings highlighted by Jung et al. [194], as well as other studies focused on Diesel engines [191, 193] can be extended to SI engines and are in agreement with Thiruvengadam et al. [40].

More recently, Sonntag et al. [196] estimated that the contribution of lubricant oil to the PM emission rates can be around 25% in gasoline engines. Pirjola et al. [197] studied particle emissions from a modern turbocharged gasoline DI passenger car engine while the vehicle was running with five different lubricant oils. Their results highlighted that particle emissions during transient operation strongly depend on the lubricant oil and a 78% reduction in PN emissions was observed solely by changing its properties.

Therefore, looking at the possible ways by which lubricant oil can reach the exhaust appears crucial in order to understand how lubricant oil can have influence on particle formation. Indeed, it is well known that lubricant oil is continuously consumed in the combustion chamber and, in some cases, it can provide the greatest contribution to the exhaust PM, even though it amounts to only about 0.2% of the fuel consumption [194] and today a preferable maximum is 0.1% [39]. For instance, metals that form solid particles can come from lubricant oil that is spread onto the cylinder walls by the piston rings or that flows into combustion chamber from the top-ring groove [198]. In addition, the design of the cylinder head-cylinder liner block structure allowing locally differing deformation of the liner when under pressure plays a primary role in determining

one of the most important escape routes. Other main routes are represented by the turbocharger seals, the valve stem seals, and the positive crankcase ventilation system [39]. However, due to the complexity of the phenomenon, it is still not entirely clear which mechanism contributes most to oil consumption.

Moreover, it has to be considered that lubricant oil may leave the cylinder walls by either vaporization or atomization. De Petris et al. [198] showed that oil mist (or oil atomized by a reverse blow-by) was a main contributor to oil consumption under their test conditions. The escape route is equally critical in deciding the extent of oxidation: for example, a small leak through the exhaust valve generates more particulate than a far larger leak through the inlet valve, simply because the oil is oxidized less effectively [39].

A crucial aspect that affects oil consumption is engine operation. Namely, significant short-lived increases are seen during accelerations [40, 199]. In the study of Yilmaz et al. [199] a sudden increase of oil consumption was measured during transients from low-load to high-load conditions: oil consumption reached a peak and then gradually decreased to the much lower steady state level of the final operating condition. The increase in oil consumption seen during accelerations is reasonably associated with and explains, at least partially, the great amount of particles (especially in the nucleation mode) released from CNG SI engines during accelerations [171, 200, 201], in particular after long idling periods [11].

The aim of the present study is to provide more insights into the effects of lubricant oil on particle emissions from both gasoline and CNG SI engines by means of an experimental campaign designed for this very purpose. Both direct and port injection modes were investigated. The results demonstrate the formation of particles produced solely from lubricant oil, and help ascertain the concentration number and size distribution of lubricant-oil-derived particles. The strategy adopted in emulating the possible ways by which lubricant oil can reach the combustion chamber was inspired by the technique used in a well-known work by Stanglmaier et al. [202], in which, a controlled amount of liquid fuel was deposited on a given location within the combustion chamber at a desired crank angle by means of a spark-plug-mounted directional injection probe so that the HC emissions due to in-cylinder wall wetting could be studied independently of all other HC sources. Since in a comparable context it was recognized to be a valid method, a similar approach was adopted in the present study. Thus, for the first time, lubricant oil contribution to the particle emission was investigated by means of external oil injection within an engine running without any lubrication. The effects on particle emissions when lubricant oil was blended into the fuel were studied too. Both direct and indirect lubricant oil injection were performed.

7.2 Experimental method

Apparatus

The experimental apparatus included the SI engine later described in detail, an electrical dynamometer, a CNG injection line, a gasoline injection line, a dedicated oil injection line, a three-hole commercial low pressure gasoline injector, a single-hole

Table 7.1: Engine specifications.

Name	Units	Value
Cylinder volume	cm^3	250
Bore	mm	72
Stroke	mm	60
Compression ratio	None	10.5
Max power	kW	7.9 at 5000 rpm
Max torque	Nm	14.7 at 5500 rpm

Natural Gas Injector (NGI), a seven-hole commercial high-pressure gasoline injector, the data acquisition and control units and four emission measurement systems. The engine was fueled with commercial European gasoline and with CNG. The gasoline chemical and physical properties are listed in Table 5.2, while the composition of the natural gas is reported in Table 6.1; the properties of the two fuels were provided by the suppliers.

The injection and ignition parameters, were set by means of a programmable electronic unit. A linear lambda sensor Bosch LSU 4.9 installed at the exhaust was used to measure the air-fuel ratio. The fuel Duration Of Injection (DOI) was properly adjusted by a closed-loop control on the lambda value to obtain a stoichiometric equivalence ratio. The in-cylinder pressure was measured by means of a quartz pressure transducer flush-mounted in the region between the intake and exhaust valves and having a sensitivity of 19 pC/bar and a natural frequency of 130 kHz. The electrical dynamometer allowed the operation under both motoring and firing conditions.

Engine

A 4-stroke, single cylinder, SI, optically accessible engine, with specifications shown in Table 7.1 and not equipped with any after-treatment device was used in all tests at 2000 rpm and full load. The spark plug was centrally located in the engine head. The engine could run in both Direct Injection (DI) and Port Fuel Injection (PFI) modes, and also without lubrication [203]. A six-hole high pressure direct injector was located between the intake valves. The intake duct was equipped with both a three-hole commercial low-pressure injector and a natural gas single-hole injector.

Emission measurement systems

PN concentrations and sizes were measured in the range from 5 to 560 nm by means of a TSI Engine Exhaust Particle Sizer. The exhausts were sampled and diluted by means of the Dekati Engine Exhaust Diluter, according to the Particle Measurement Programme (PMP). The dilution ratio was fixed at 1:79. A 1.5 m heated line was used for sampling the engine exhausts in order to avoid condensation of combustion water. The sample is first diluted with air heated above 150 °C. Then, the sample passes through an evaporation chamber at a temperature above 300 °C for removing volatile particles. This system allows to measure the solid particles defined by the PMP as

particles that can survive passing through an Evaporation Tube with a wall temperature of 300–400 °C. Samples for the particle characterization were taken directly from the exhausts, shortly after leaving the cylinder.

CO, CO_2 and HC emissions were measured by means of non-dispersive infrared detectors; NO_x were detected by means of electrochemical sensors. Opacity [%] was continuously measured by an AVL 439 Opacimeter. Methane-HC emissions were measured by means of a Flame Ionization Detector.

7.3 Experimental procedure

The present work focused on the formation of soot particles derived solely from lubrication oil and, through the analysis of the number concentration and PSD functions, helped to isolate the size ranges and the amounts of lubricant-oil-derived particles.

Eastwood [39] summarized the relevance of engine lubricant for particulate emission as: "*Investigations in which oil consumption is increased deliberately, by artificial means, might be relying on precarious assumptions as to the combustion mode of this oil. These remarks highlight the need to learn much more about the combustion of escaping lubricant.*" This statement is related to what Sutton et al. [204] observed when a lubricant-fuel mixture is burned: the resulting ash differs in its morphology from that observed when lubricant is instead entrained into the air intake as a mist.

In light of these considerations, three different ways of providing the excess lubricant oil and two injection modes (PFI and DI) were investigated. When gasoline was used as fuel, a lubricant-fuel mixture was prepared and then injected in either port or direct mode, allowing to study how the injection mode impacts the soot formation dynamics. When the engine was fueled with CNG, always port injected, the oil was either entrained into the intake manifold or directly into the combustion chamber. In the latter case, a relatively large amount of lubricant was released for a very short time (the oil injection, lasting only 30 CADs, lasted less than 12 engine cycles, namely, about 0.7 s). This procedure aimed at emulating the droplet escape from the valve stem seals directly into the combustion chamber.

By these means, it was possible to observe the lubricant contribution to particle emissions with the oil both separately injected into the intake and directly into the combustion chamber, as well as supplied as "additive" to the fuel, when the latter is provided to the engine both within the intake manifold and directly into the combustion chamber.

In the present experiments, with the purpose of clearly isolating the lubricant contributions, we chose to start from a level of the oil-to-fuel mass equal to 1%, representative of transient operating conditions [199], in which the oil contributes most to particle emissions [11, 171, 200, 201]. Then, oil-to-fuel mass fractions equal to 3, 5 and 7% were used to investigate how PN and sizes relate to the amount of oil entering the combustion chamber.

CNG tests

Figure 7.1 shows a schematic representation of the experimental set-up for CNG tests. The gaseous fuel was supplied by a pressurized bottle using a pressure regulator typically set to 5 bar. The CNG single-hole injector (number 8 in Figure 7.1) was used for the natural gas injection. When the oil was injected into intake manifold, a three-hole commercial low-pressure gasoline injector was used (number 4 in Figure 7.1). In the droplet-emulation tests, in which oil is directly injected into combustion chamber, the six-hole high-pressure commercial injector (number 5 in Figure 7.1) was employed.

The oil injection line is depicted in yellow in Figure 7.1. This arrangement achieved the greatest precision in matching the lowest values of the injected oil mass. Heating the oil to 55 °C allowed a decrease in viscosity (and density), which strongly depends on the temperature (especially below the usual temperature working conditions). It is known that the viscosity of a fluid lubricant affects friction. The addition of a return circuit ensured continuous oil motion into the pipes (especially near the injector nozzle) and avoided oil cooling which might lock the injection at the lowest DOI. A pressure regulator (number 6 in Figure 7.1) was used to set and monitor the oil injection pressure at 2.8 bar, which is a reasonable compromise between the small flow rate required and the proper injector operation.

The oil used in the experiments was a commercial, multi-grade, low viscosity, full-synthetic lubricant 0W-30. Its main physical and chemical characteristics, as provided by the supplier, are listed in Table 7.2.

It was essential to characterize the injector behavior at the lowest injected flows,

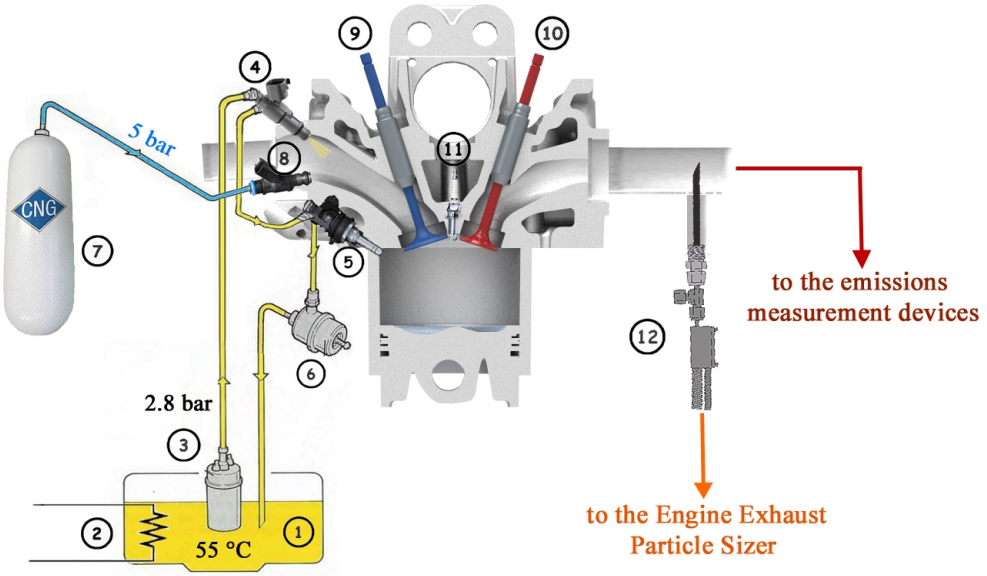

Figure 7.1: Experimental Set-up for the CNG tests. (1) Oil tank; (2) resistors for heating the oil to 55 °C;(3) oil pump; (4) 3-hole commercial low pressure injector; (5) 6-hole commercial high-pressure injector; (6) oil pressure regulator; (7) CNG bottle; (8) CNG 1-hole injector; (9) intake and (10) exhaust valves; (11) spark-plug; (12) particle sizer probe.

Table 7.2: Physical and chemical lubricant oil characteristics (Castrol© EDGE 0W-30 technical datasheet)

Name	Method	Units	Value
Density @ 15 °C, Relative	ASTM D4052	g/ml	0.842
Viscosity, Kinematic 100 °C	ASTM D445	mm^2/s	12.3
Viscosity, CCS -35C (0W)	ASTM D5293	mPa.s (cP)	5800
Viscosity, Kinematic 40 °C	ASTM D445	mm^2/s	72
Viscosity Index	ASTM D2270	None	169
Pour Point	ASTM D97	°C	-51
Flash Point, PMCC	ASTM D93	°C	200
Ash, Sulphated	ASTM D874	%wt	0.8
Distillates (petroleum), hydro-treated heavy paraffinic	CAS: 64742-54-7	%	≤75÷<90
Lubricant oils (petroleum), C20-C50, hydro-treated neutral oil-based	CAS: 72623-87-1	%	<10

since a small amount of injected oil was the desired target. Figure 7.2 reports the results obtained using two different configurations. The red line refers to the earlier described arrangement, while the blue line was obtained without the oil return circuit and by injecting a slightly different oil (a 5W-30 of a different supplier) at room temperature. In this case, it was not possible to inject less than 10% of the fuel mass flow rate, which is disproportionately larger than the selected minimum value of 1%. This highlighted how difficult can be injecting such small oil amounts whit the required precision. Therefore, the experimental set-up of Figure 7.1 was used during the whole experimental campaign.

Since the optical engine can run without requiring any lubrication, it was possible to obtain zero-oil baseline measurements. However, the length of each test had to be short to avoid damage to the self-lubricating teflon-bronze composite piston rings. The extra-oil injected fouls the optical access, without increasing the lubrication effect. Short combustion durations can be a problem in reaching stable measurements. In Figure 7.3(a) a typical observed total number concentration behavior of the emitted

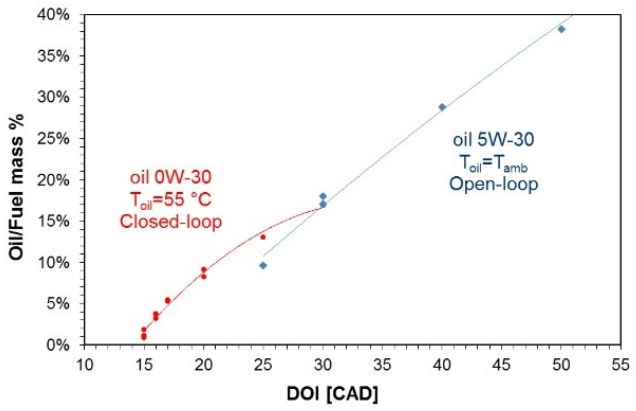

Figure 7.2: Three-hole oil Injector characterization with two different set-ups. The injected mass flow rate is normalized by the fuel mass flow rate.

particles during a test with natural gas and 1% of oil continuously injected into intake manifold is reported. The number of the detected particles increased as soon as combustion started and kept increasing until it ended, and the size distribution also kept changing. Thus, it was not possible to reach a steady state condition before the end of combustion by using a standard oil injection strategy. It was supposed that, the oil impacted the intake manifold walls and a film formed, so that the oil amount carried by the intake air flow increased constantly together with the number of particles detected at the exhausts. In order to avoid this drawback and reach steady conditions just as the combustion started, lubricant oil injection was started about one and half minutes before the combustion, while the engine was motored. This allowed the film thickness to stabilize before the start of the test, as shown in Figure 7.3(b). No appreciable fluctuation was visible in this case during the combustion period. This approach was used in all CNG tests with oil entrained into the intake manifold.

In all tests, the CNG at stoichiometric conditions was injected for 115 CADs, ending at TDC, and ignition was triggered at 24 CADs.

Gasoline tests

In gasoline tests the oil was always mixed with the fuel; four different oil-gasoline mixtures were used and both the PFI and DI strategies were adopted. In the PFI case, the three-hole commercial low-pressure injector (placed in position 4 in Figure 7.1) was used. In the DI case, the six-hole high-pressure commercial injector (located in position 5 in Figure 7.1) was used to inject either the gasoline or the mixture of oil-gasoline directly into the combustion chamber. In the latter case, the gasoline was injected at a

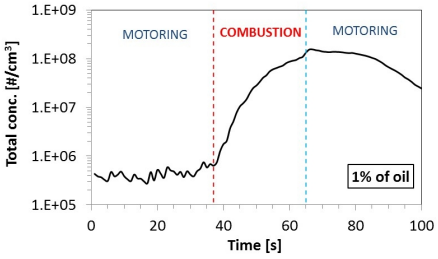

(a)

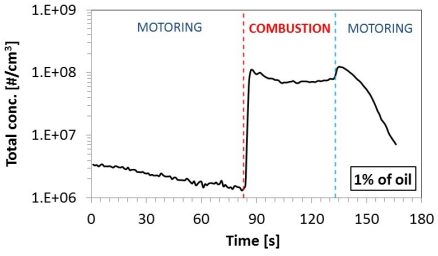

(b)

Figure 7.3: Total PN concentration measurements for CNG test with 1% of oil without (a) and with (b) "film-strategy". Red dashed line: start of combustion; light blue dashed line: end of combustion.

pressure of 100 bar using an additional high-pressure pump. When the PFI mode was employed, steady conditions were not reached just as in the case of CNG tests and the same motoring strategy was again used with success.

For a better comparison with CNG tests, stoichiometric conditions were always enforced and ignition was again triggered at 24 CADs before TDC, which allowed a stable and efficient combustion in all tests.

During the PFI mode, gasoline was injected for 120 CADs and the injection ended 230 CADs before TDC. During the DI mode, an early Injection was adopted, starting 285 CADs before TDC and lasting about 35 CADs.

7.4 Results and discussion

The results obtained in the PFI mode for both the CNG and gasoline tests are described first. Then, we examine those obtained when the oil-gasoline mixture as well as the lubricant oil alone were injected directly into the combustion chamber.

PFI tests

In order to achieve a reasonable statistical validity, several repetitions of each test were carried out, and the derived mean values for each test were used for the comparisons. In each graph of Figure 7.4 all available repetitions of each single test are shown for both CNG and gasoline. This comparison, besides providing statistical validation of the results, highlights the fact that no appreciable differences were seen between the two different ways in providing the excess lubricant from the PN point of view.

Figure 7.5 shows the total concentration number evolution with time for representative tests for each oil percentage considered. In Figure 7.6 the corresponding granulometric distributions are depicted. By looking at Figure 7.5 it is possible to appreciate that all the combustion measurements were stable, and had very low variability. This is also appreciable from the 95% confidence interval reported for each distribution (red lines) in Figure 7.6. It is also interesting to notice that as soon as the amount of the injected lubricant oil starts to be very large (Figure 7.5(d) and 7.5(e) for CNG and 7.5(iv) and 7.5(e) for gasoline), PN started to increase during motoring conditions that preceded the combustion period. It might be reasonable to suppose that the film formation process on the intake manifold walls could be effectively taking place. This aspect appears distinguishable since the oil is 3% of the CNG injected mass (Figure 5 (c)) and even when oil is at 1% for the gasoline tests (Figure 7.5(ii))).

A direct comparison between the mean values reported in Figure 7.4 summarizes these observations. Figure 7.7 uses two different scales to provide a global and detailed view at the same time. If a linear scale is chosen (see Figure 7.7(a) and 7.7(i)), it is not possible to see the baseline zero-oil curve because it is roughly two-orders of magnitude below the value range of the data. Conversely, if the data are plotted along a logarithmic scale, details about the peaks are lost. The level of PN measurable when burning natural gas is so low as to be very close to the level recorded during motoring

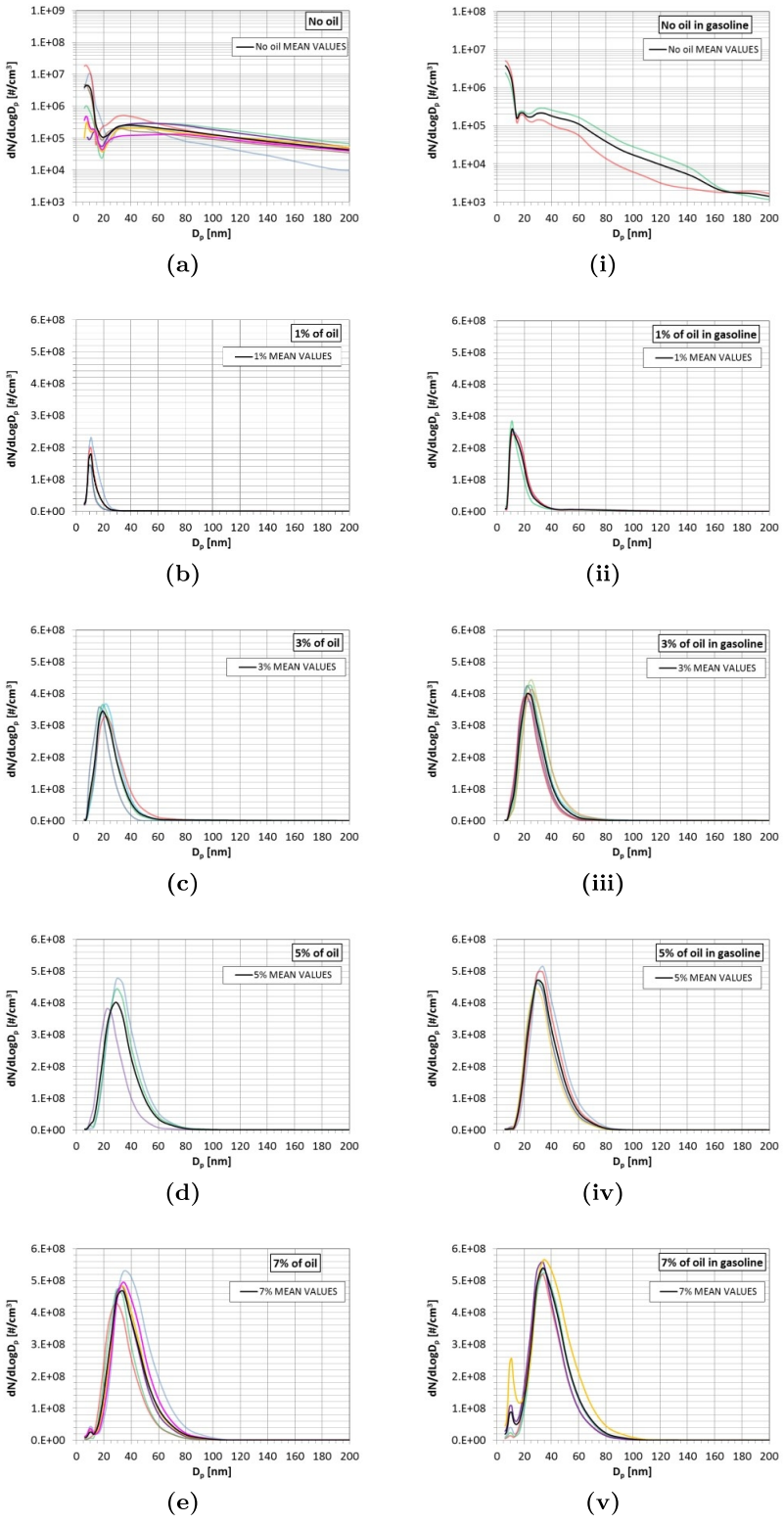

Figure 7.4: Statistical data concerning the PSD functions measured for both CNG (Latin characters) and gasoline (Roman numerals) PFI tests. In each graph, the distributions obtained from each repetition of the same test are reported, together with their calculated mean value (black line). Zero-oil measurements baseline (a) and (i) are reported with a different scale.

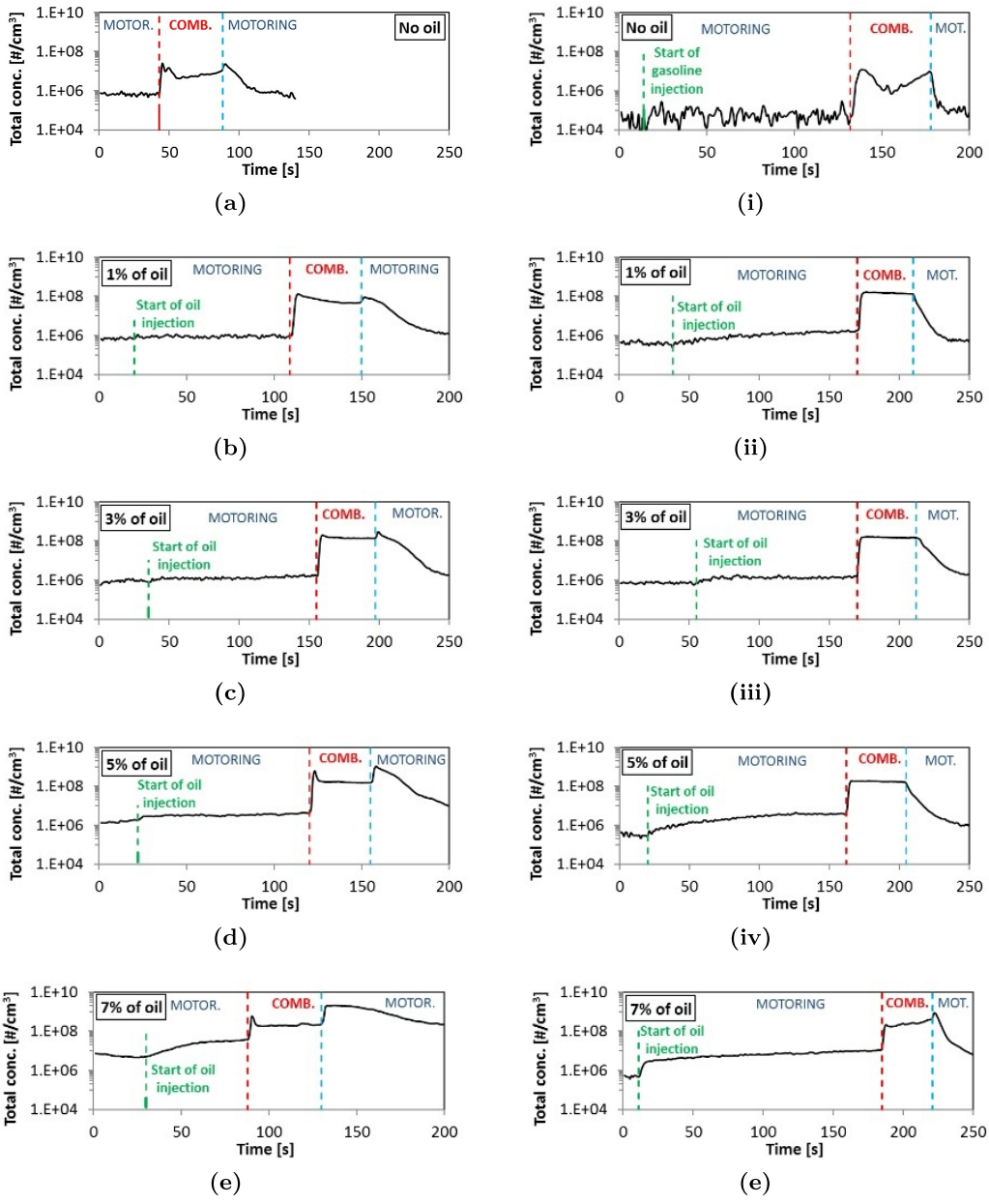

Figure 7.5: Total concentration number trace evolution with time of one representative case for each explored operating condition, for both the CNG (Latin characters) and gasoline (Roman numerals) PFI tests. Green dashed line: start of oil injection into the intake manifold; red dashed line: start of combustion; light blue dashed line: end of combustion.

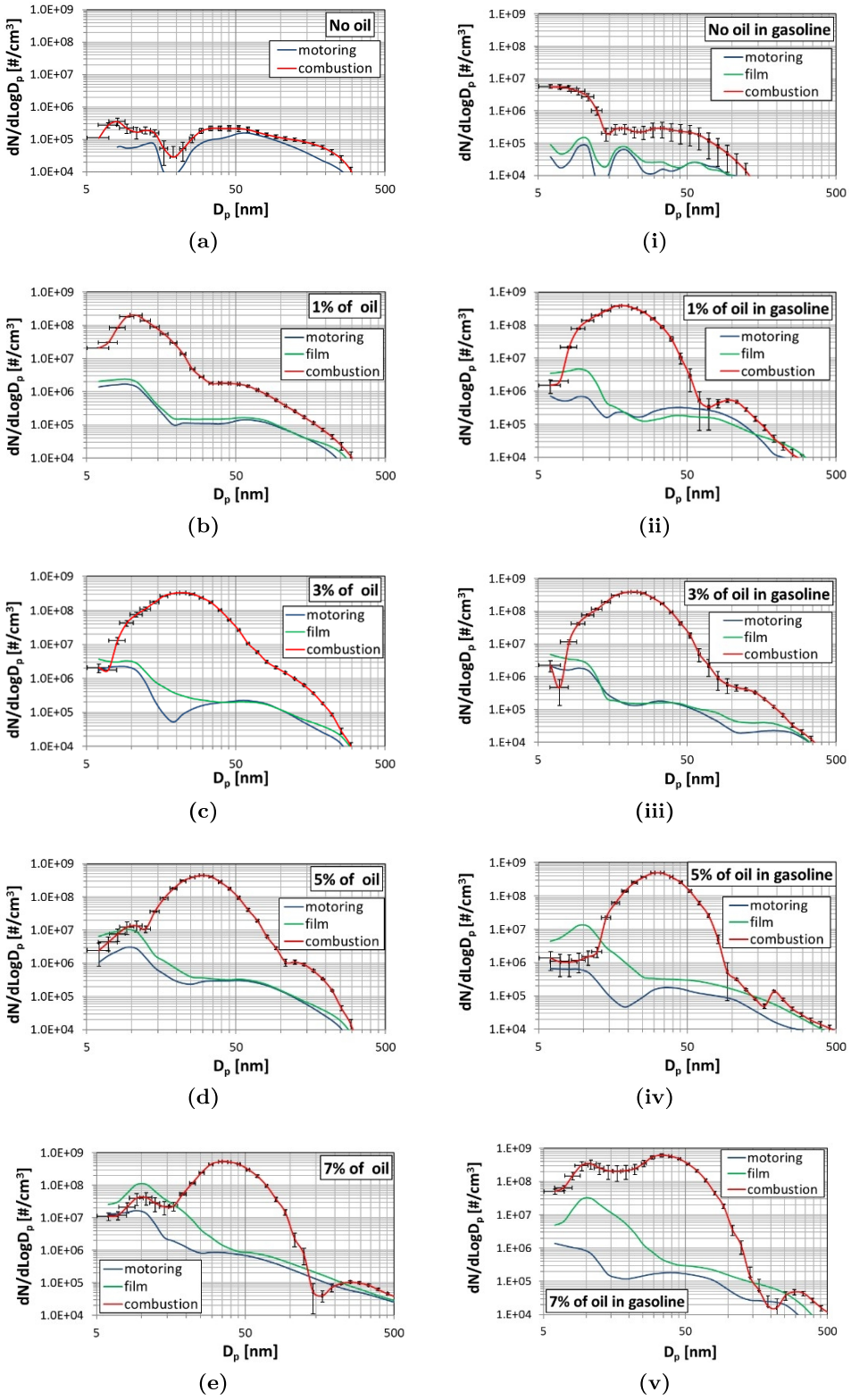

Figure 7.6: PSD functions for one representative case for each explored operating condition for both the CNG (Latin characters) and gasoline (Roman numerals) PFI tests. Light blue line: PSD during motoring conditions; green line: PSD after film forming; red line: PSD during combustion.

conditions, as seen from Figure 7.6(a). The values recorded with gasoline are low too (Figure 7.6(i)).

Adding oil when the fuel is port injected increases the particles emitted in the lowest range-size. Figure 7.7 shows that the peak of the PSD moves with increase of oil content, starting from 10 nm (with 1% of oil), but never exceeds 35 nm (with 7% of oil). That means that, although a very large amount of oil is released, the detectable particles at the exhaust always fall within the nucleation mode distribution, independently of the way lubricant is added.

In the last case (7% of oil) the granulometric distribution starts to become bi-modal. A second mode appears in the lowest size range, while the main peak is at about 35 nm. This behavior was observed during both CNG and gasoline tests. By looking at Figure 7.6, it is possible to see that the particles detected during oil injection in motoring conditions belonged to the finest range of the nucleation mode. When oil is at the maximum considered level (Figure 7.6(e) and 7.6(v)) in all recorded test repetitions (compare Figure 7.4(e) and 7.4(v)) the secondary peak appeared in the same position where the distribution peak was located shortly after that the film was completely formed. This suggests that some oil survived without burning and reached the particle sample point.

Changes were induced to the HC by increasing the lubricant oil amount. Figure 7.8

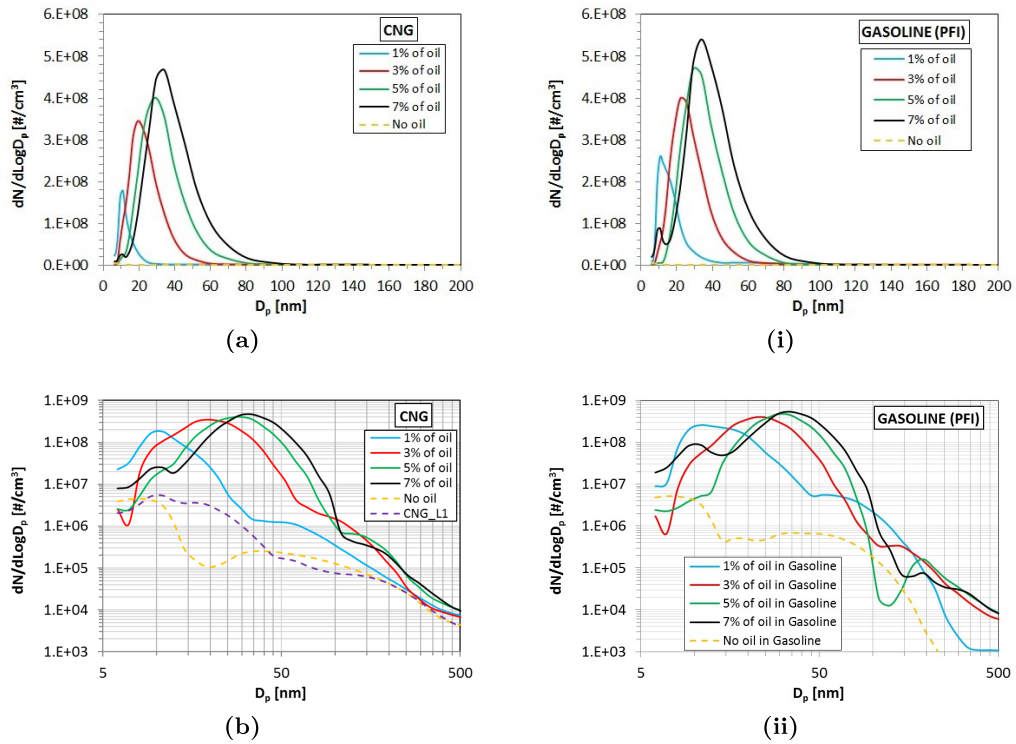

Figure 7.7: PSD functions (mean values) with a mass lubricant oil content equal to 0% (yellow line), 1% (light blue line), 3% (red line), 5% (green line) and 7% (black line), for both the CNG (Latin characters) and gasoline (Roman numerals) PFI tests. For clarity, the data are plotted by using both a linear (a) and (i), and a logarithmic scale (b) and (ii).

shows that in CNG tests the total HC (THC_{c1}) emission level increased because of the increase in Non-Methane-HC (white bars), while Methane-HC remained constant in all cases. A maximum increase of 10% (passing from 0 to 7% of oil) was observable in Non-Methane-HC, while the remaining part was more than doubled (150%), which means a total increase of about 40% in HC emissions. When 1% of oil is considered, the total HCs were 6% more than the base-line value.

On the contrary, it should be noted that no significant variations in the levels of CO, CO_2 and NO_x were observed in the tests. The fact that the Non-Methane-HC increased indicates that the oxidation process of the lubricant oil within the combustion chamber was far from complete, especially for the largest oil amounts. As a consequence, the hydrocarbons that constitute the lubricant oil were not converted into CO or CO_2, explaining why no variations were recorded. For the same reason, no noticeable variations were observed in the heat-release and the NO_x, since the oxygen content within the combustion chamber was also practically unchanged. The fact that no appreciable variations were recorded in the heat-release, as well as in the in-cylinder pressure traces, also highlights the inability in distinguishing how much lubricant oil is

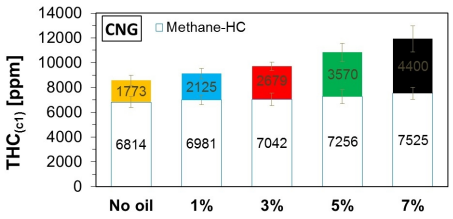

Figure 7.8: Total HC emissions (THC_{c1}) divided in Methane-HC (white bars) and Non-Methane-HC (bars colored according to the oil percentage) for CNG tests

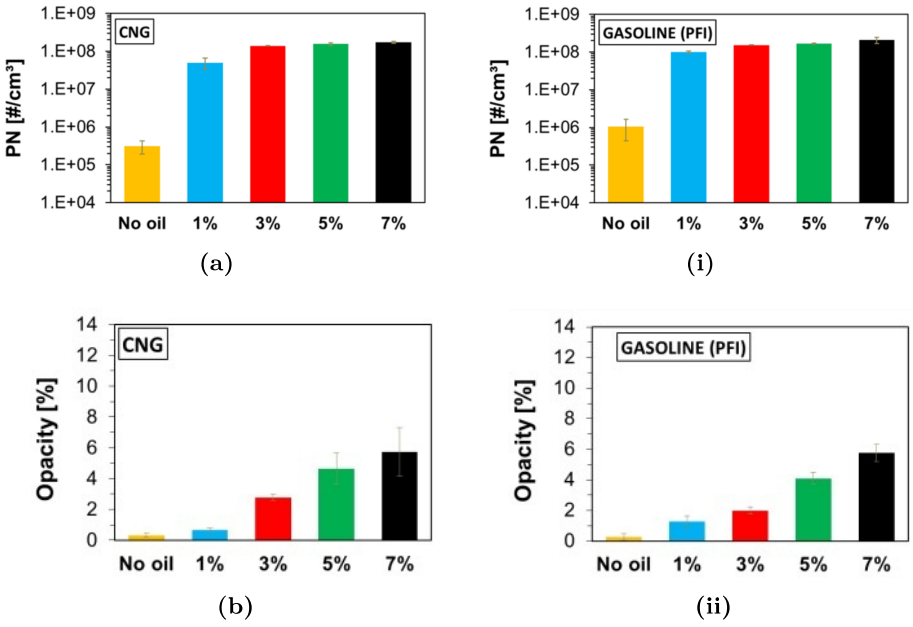

Figure 7.9: Total concentration number for CNG (a) and gasoline (i); opacity [%] for CNG (b) and gasoline (ii) tests.

present in the combustion chamber without performing emissions measurements.

Figure 7.9 depicts the opacity values recorded during CNG (7.9(b)) and Gasoline (7.9(ii)) tests and offers a comparison with the corresponding PN total concentration levels (a), (alpha). The general trends are in good agreement each other and the similarity observed between the two different ways to add lubricant oil to the combustion is also confirmed. The PN suddenly increases by two orders of magnitude as soon as 1% of oil is provided, both in CNG and gasoline operation mode, and then it increases very slightly. The opacity shows a smoother increase, most likely because the emitted particles are too small when the oil content is low and only when their size becomes appreciable do they begin to be detected by the opacimeter.

Gasoline DI tests

Results from the experiments in which an oil-gasoline mixture was directly injected into the combustion chamber are here discussed.

For the DI tests, the repeatability and stability are summarized in Figure 7.10, by taking a representative case as example (5% of oil in gasoline). All repetitions are seen to be close to each other (Figure 7.10(a)). The PN measurement is very stable (Figure 7.10(b)) and consequently the PSD has a well-defined shape (small width of the 95% confidence interval bars in Figure 7.10(c)). All others cases presented very similar characteristics and for the sake of brevity, only the mean values are reported in the following discussion.

A comparison between the measured PSDs when the oil content in the direct injected gasoline was changed from 1 to 7%, is reported in Figure 7.11. As previously done for Figure 7.7, the data of Figure 7.11 are plotted by using two different scales for clarity. The formation mechanics of particulate matter is quite different from the PFI case [205]. When no oil was present in gasoline a predominance of particles attributable to the accumulation mode was observable (yellow curve in Figure 7.7(b)), in contrast to what was obtained in the PFI tests (yellow curve in Figure 7.7(ii)).

When oil was added the number of particles falling in the nucleation mode started to be relevant and the shape of the distribution changed. Once again, oil manifested its presence in the lowest range size, but this time the accumulation mode was not negligible. In this case, an increase in the oil content in gasoline also increased the number of particles with sizes larger than 50 nm. This behavior is mainly derived from the soot formation mechanics related to the DI mode. One of the most important aspects related to the soot emission in DI engines is attributable to the fact that some fuel strikes the piston and accumulates as liquid films or pools, which ignite and burn with sooty flames. This is enhanced when an oil-fuel mixture is injected. The poor combustion in pool fires is also responsible for organic particulate, derived either directly from the fuel or from its pyrolysis [39].

Finally, the opacity [%] and the total number of particles detected per cubic centimeter are reported in Figure 7.12. Because of the larger size of the measured particles, when just gasoline was direct injected (Figure 7.12(b) the opacity recorded was 12-times greater than the corresponding PFI value (Figure 7.9(ii)). The same

reason explains why in DI mode the opacity increased much more when lubricant oil was progressively added to gasoline.

Oil DI tests (emulation of oil droplet release with CNG-PFI)

Results from the third way to provide the excess oil are described. Namely, findings coming from the experiments in which the engine was fueled with CNG in PFI mode and the oil was injected directly into the combustion chamber are now examined. These tests emulated droplet release from valve stem seals with oil direct injection and port injected CNG. A relatively large amount of lubricant was released in a short time period.

Four repetitions of the tests produced identical results, as depicted in Figure 7.13. 7.13(a) shows that the PN starts to increase as soon as the oil is injected. It reaches a peak level significantly higher than the steady state values and then gradually decreases to the initial steady state level. Figure 7.13(b) and 7.13(c) provide the time evolution of the PSD function observed during these "transient" measurements, starting a couple of

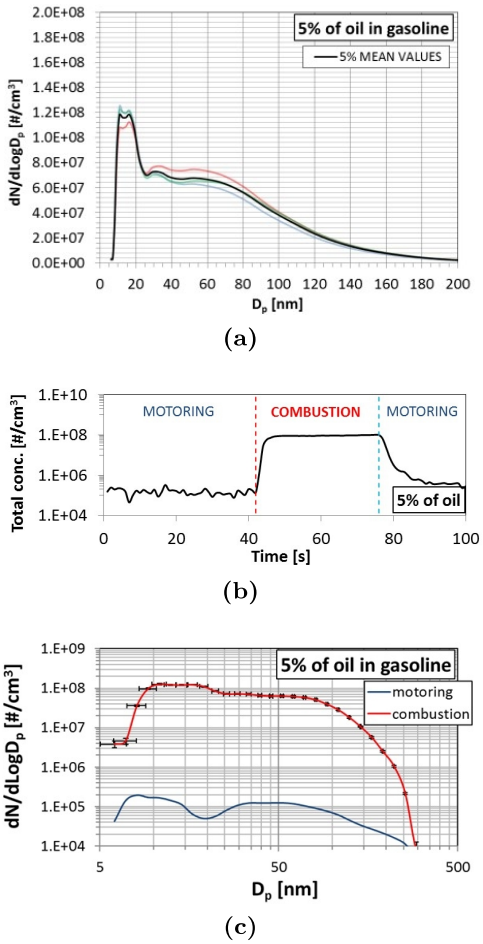

Figure 7.10: Statistical PSD functions (a), total concentration number trace evolution with time (b) and PSD functions during motoring conditions and combustion (c) of one representative case (5% of oil) for gasoline DI tests.

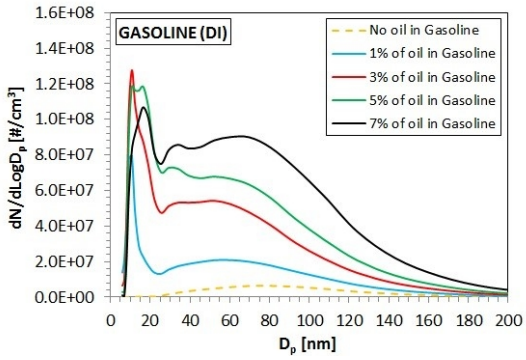

(a)

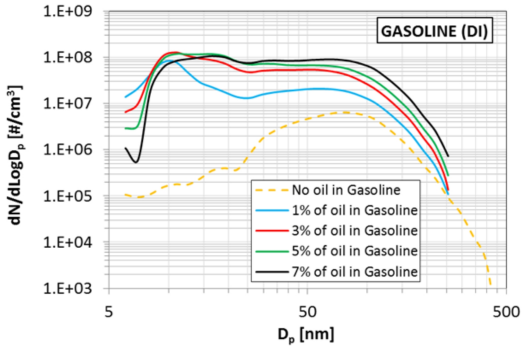

(b)

Figure 7.11: PSD functions (mean values) with mass lubricant oil content equal to 0% (yellow line), 1% (light blue line), 3% (red line), 5% (green line) and 7% (black line). For clarity, the data are plotted by using both a linear (a) and a logarithmic scale (b).

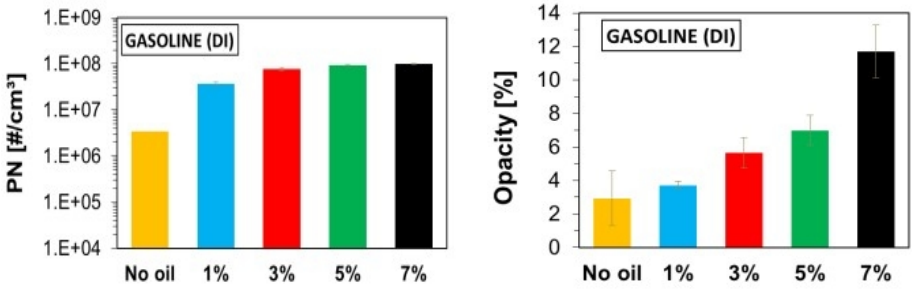

(a) (b)

Figure 7.12: Total concentration number (a) and opacity [%] (b) for gasoline DI tests.

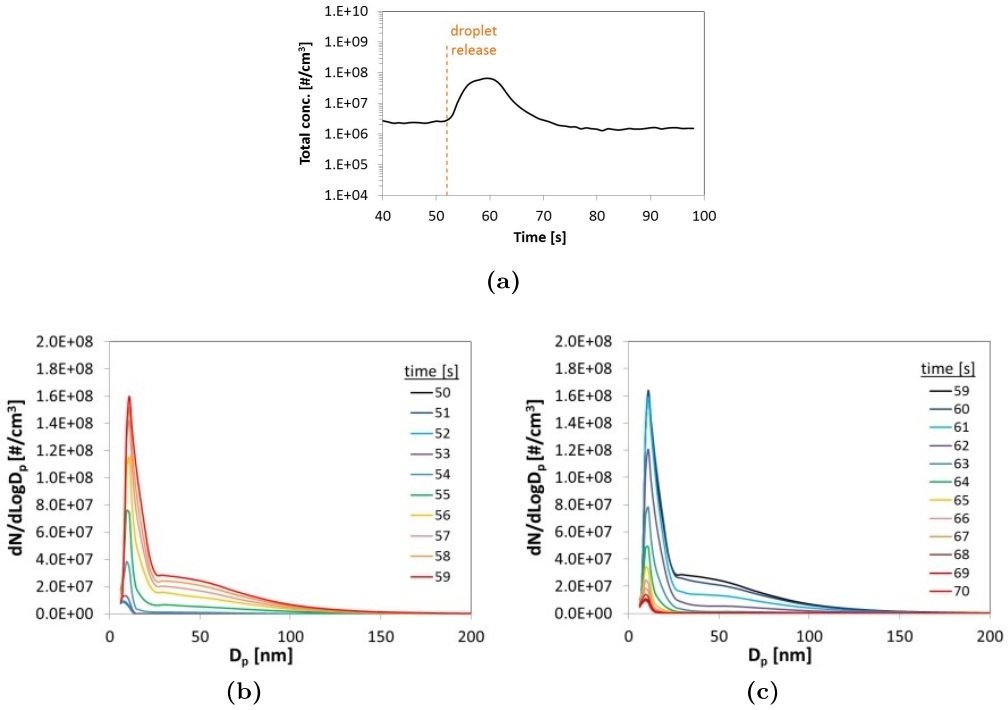

Figure 7.13: Total concentration number trace evolution with time (a) and PSD time evolution during the first 9 seconds (b) and the subsequent 10 seconds (c), for emulation of oil droplet release.

seconds before the start of oil injection. Figure 7.13(b) shows that, during the first nine seconds, the total PN increase corresponds to the increase of the smallest size particles. The PSD shape looks more similar to that seen in the gasoline DI tests (in which a lubricant-fuel mixture was injected directly into the combustion chamber) rather than that observed during the CNG tests (when the oil was injected into the intake manifold as a mist). Figure 7.13(c) shows that the distribution takes on goes back to its original shape before the oil injection start.

These findings highlight that the way the oil reaches the combustion chamber characterizes the particle emission dynamics. Oil always increases the number of very small particles; and in fact, even when the lubricant amount is quite large, particles exceeding 50 nm appear in appreciable quantities only if the oil is injected directly into the combustion chamber so that it can survive as liquid droplets.

7.5 Conclusions

An extensive experimental investigation was conducted to provide insights about the effects of lubricant oil on particle emissions from both gasoline and CNG SI engines. Three different strategies to provide the additional lubricant oil and two combustion modes (PFI and DI) were investigated. When gasoline was used as fuel, a fuel-oil mixture was either port- or direct-injected. When the engine was fueled with CNG, the oil was either injected into the intake flow or directly into the engine combustion

chamber, while port injected CNG was provided as fuel. This last strategy aimed at simulating droplet release from valve stem seals.

The optically accessible engine was run without lubrication. A dedicated oil injection line, coupled with an early lubricant oil injection (oil injection started when the engine was motored) allowed stable and repeatable measurements of the particle emissions, despite the very short available test time. Lubricant oil was 1, 3, 5 and 7% of the fuel mass and the results were compared with the "oil-free" condition for each fuel and injection mode considered.

In all of the experimental arrangements, oil addition produced a significant increase of very small particles emitted. When oil was fed to the intake manifold, both by itself and blended with fuel, the peak of the PSD function increased with the oil content, starting from 10 nm (with 1% of oil), but it never exceeded 35 nm (with 7% of oil).

When no oil was present in the direct injected gasoline, a predominance of particles attributable to the accumulation mode was observed, in contrast to what obtained in PFI mode, as expected with Diesel-like conditions favoring the generation of larger soot particles. When an oil-gasoline mixture was considered in the DI tests, particles with the finest size started to appear and began to predominate. However, in this case, an increase in oil content also led to an increase in the number of particles with sizes larger than 50 nm. This behavior was mainly attributable to the fact that what was seen when just gasoline was direct injected is now enhanced by the presence of lubricant.

The emulation of droplet release coming from valve stem seals was experimentally realized by providing the excess oil directly into the combustion chamber during CNG (PFI) combustion. The PSD function presented a shape more similar to that seen in the gasoline DI tests, rather than that observed during the CNG tests, in which the oil was entrained in the intake manifold.

With lubricant oil addition, no significant variations in engine-out CO, CO_2 and NO_x were observed. However, in the CNG tests the total HC emission levels increased because of the increase in Non-Methane-HC, while Methane-HC remained constant in all cases. This indicated that the oil was not completely oxidized within the combustion chamber. In addition, in both gasoline and CNG (PFI) tests, the PN suddenly increased by roughly two orders of magnitude when 1% of oil was provided. The opacity measurements showed a smoother trend, most likely because the emitted particles were too small for the opacimeter when the oil content was low. This also explained why the opacity number, recorded when just gasoline was direct injected, was 12-times greater than the corresponding value in the PFI mode.

It was found that oil addition always produced a remarkable increase of the finest particles. This finding is in agreement with previous research in which it was shown that lubricant oil assumes the aspect of an exhaust aerosol having log normal-size distributions with geometric mean diameters that never exceed 30 nm. In addition, the present results confirm what obtained in Master's Thesis and in the Chapter 3, as well as, findings from other studies in which it was supposed that the larger oil consumption seen during accelerations might be associated with the great amount of nucleation mode particles released from CNG SI engines during accelerations. In the present work, a noticeable amount of accumulation mode particles was seen only when lubricant oil was directly injected into the combustion chamber, and this proves that the

way lubricant oil reaches the combustion chamber does affect the dynamics of particle emissions formation whether it is blended or not with the fuel. Further improvements of the designed oil injection line would allow the possibility to inject even less oil than the minimum level of 1% considered in this study. In addition, tests with different lubricant composition could also further establish the influence of oil characteristics on soot emissions. A further investigation of the effect that different additional dilutions of the exhaust sample can produce on the results is also needed, since the volatile part of the recorded particle emissions can play a significant role. In addition, exploiting the optical accessibility of the engine will also provide very useful additional information. Therefore, separate tests will be performed in which changes in the apparent luminosity will be recorded, as well as OH* and CH* will be detected by means of UV-visible spectroscopy and images of the oil injection will be recorded.

8 Summary and outlook

The present work, by means of both numerical and experimental investigations, aimed to provide more insights in understanding the mechanisms of particle emission processes in Spark-Ignition engines. Different fuels, including gasoline and natural gas, were considered. In particular, specific tests were designed with the aim to isolate the contribution of the fuel to that of lubricant oil to particle emissions.

After providing some fundamental concepts in Chapter 1 and a brief but exhaustive description of the numerical model used in the simulations in Chapter 2, in Chapter 3 preliminary important results about the role that external sources can have on soot emissions were reported. In particular, 3-D CFD simulations helped to explain the reasons for the results obtained in the experimental campaign carried out during the Mater's Thesis work, in which an EURO-VI, heavy-duty, stoichiometric SI engine fueled with compressed natural gas was tested. It was noted that before the flame front reaches the cylinder walls, soot is mainly produced within the flame region, and soot residing in the burnt regions is reduced with sufficient residence time at high temperatures by oxidation. Soot oxidation was favored when the flame front reached the cylinder walls and no more species for soot inception and surface growth were left after the combustion. The model demonstrated sensitivity to the variation of operating conditions in qualitative agreement with corresponding calculations from measured variables. Considering that further oxidation as well as physical soot transformations could occur in the exhaust pipes the agreement was considered to be satisfactory.The predicted soot particle mass was lower than the experimentally derived value. This suggests that other possible sources which can affect soot formation need to be taken into consideration, as well as fuel combustion.

In the subsequent Chapter 4, to answer to the need of more accurate correlations for laminar flame speeds of practical fuels, simple and workable expressions, suitable for spark-ignition engine simulations were derived. Such relationships allow laminar flame speed calculations as a function of equivalence ratio and unburned mixture temperature and pressure over a wide range of operating conditions. Measurements of laminar

flame speeds in literature were collected and used to develop empirical correlations for equivalence ratios from 0.6 to 1.7, pressures between 1 and 50 atm and temperature from 298 to 800 K. Pure compounds, such as methane and propane, binary mixtures of methane/ethane and methane/propane, as well as more complex fuels like natural gas and gasoline were considered. For binary and ternary mixtures, it was shown that the influence that the amount of the secondary compounds has on the mixture laminar flame speed is different at different equivalence ratios, which has not been considered in previous formulations. An improved formulation was developed for calculating the laminar flame speed of natural gas, which was modeled as a ternary mixture of methane, ethane and propane. In each case, comparisons with experimental data confirmed the obtained improvements.

The implementation of such empirical correlations within the CFD code allowed to obtain very good agreement with the experimental measurements, as reported in Chapter 5, in which load increases were achieved by pure oxygen addition in a gasoline SI engine. The purpose of these tests was to provide additional basic information about oxygenated fuel combustion, while avoiding still existing uncertainties relating to chemistry models. The results showed that the effect of oxygen addition was to speed up the combustion process and the induced increase in load was roughly linear with increased oxygen content. Oxygen addition produced a faster burning velocity and higher in-cylinder temperatures. During the initial combustion stages, higher soot mass fractions were seen near the fame front regions, but the oxidation rates due to OH radicals were enhanced in a significant way as well. Therefore, the in-cylinder soot mass distribution obtained with oxygen addition was comparable to the baseline case. The numerical results were in good agreement with experimentally measured PSDs and provide confidence in the soot model in predicting soot emissions. As for the results shown in Chapter 3 the number of the finest particles was overestimated by the numerical model, but this can be explained by considering that oxidation process that may occur in the exhaust was not considered in the simulations. These results confirmed that soot oxidation rates can have an effect as strong as formation rates have on soot emissions levels eventually detectable at the exhaust of a SI engine.

Chapter 6 presented experimental results concerning the influence that variations in natural gas composition can have on the performance and emissions of a single-cylinder SI engine. In particular, the work focused on the effects generated by a modification in the heavier hydrocarbons content. To pursue this aim, an innovative experimental procedure was designed and validated to obtain precise real-time methane/propane mixtures to be injected directly into the intake manifold. For all mixtures and conditions, the effect of propane addition was to increase the IMEP value and, at the same time, to reduce the COV, resulting in more stable and efficient combustion than pure methane. In all tests, natural gas showed the highest PN values. Increasing the engine speed resulted in a general increase in the number of particles emitted. At 4000 rpm, increasing the propane content produced an increase in the number of particles between 5 and 30 nm, highlighting the relevance of the ultrafine range in the particle emissions emitted from natural gas engines. Further investigations are needed in which different conditions in terms of equivalence ratio, and energy content of the fuel are of interest. The effect of varying natural gas additives should be considered as well. Performing 3-D CFD

simulations of the studied cases will provide further guidance in understanding the mechanisms of particle formation process.

It has been underlined that lubricant oil contribution to particle emissions cannot be neglected, especially when the fuel itself produces low levels of soot emissions. Therefore, it is crucial to perform studies in which the fuel composition contribution to particle emissions is separated from that of the lubricant oil. Chapter 7 demonstrated the formation of particles produced solely from lubricant oil, and helped ascertain the concentration number and size distribution of lubricant-oil-derived particles in both gasoline and CNG SI engines by means of an experimental campaign designed for this very purpose. Three different ways of feeding the extra lubricant oil and two fuel injection modes – Port Fuel Injection (PFI) and Direct Injection (DI) – were investigated to mimic the different ways by which lubricant may reach the combustion chamber. When gasoline was used as fuel, a fuel-oil mixture was either port- or direct-injected. When the engine was fueled with CNG, the oil was either injected into the intake flow or directly into the engine combustion chamber, while port injected CNG was provided as fuel. This last strategy aimed at simulating droplet release from valve stem seals. An optically accessible engine requiring no lubrication was used. A dedicated oil injection line, coupled with an early lubricant oil injection allowed stable and repeatable measurements of the particle emissions. The results showed that adding oil when the fuel is port injected increased the particles emitted in the lowest range-size. It was also observed that the peak of the PSD moved with increase of oil content, but never exceeded 40 nm. Even when the lubricant amount was quite large, particles exceeding 50 nm appeared in appreciable quantities only if the oil is injected directly into the combustion chamber, whether blended or not with the fuel. The present results confirm findings from other studies in which it was supposed that the larger oil consumption seen during accelerations might be associated with the great amount of nucleation mode particles released from CNG SI engines during accelerations. They also confirm what was observed in Master's Thesis experiments and in the Chapter 3, in which it was supposed that the larger oil consumption seen during accelerations might be associated with the great amount of nucleation mode particles released from CNG SI engines during these transient conditions.

Much can still be done for elucidating the mechanisms of oil-derived soot formation, which may be very important in reducing soot emissions in CNG engines and in developing new lubricant oil formulations. Further improvements of the designed oil injection line would allow the possibility to inject less oil with different lubricant composition, allowing to study the influence of oil characteristics on soot emissions. A further investigation of the effect that different additional dilutions of the exhaust sample can produce on the results is also needed, since the volatile part of the recorded particle emissions can play a significant role. In addition, exploiting the optical accessibility of the engine will also provide very useful additional information. Therefore, separate tests will be performed in which changes in the apparent luminosity will be recorded, as well as OH* and CH* will be detected by means of UV-visible spectroscopy and images of the oil injection will be recorded. In addition, as shown in Chapter 3, the development of chemical reaction mechanisms for oil oxidation is needed for more accurately simulating soot formation in SI engines, since the oil contribution cannot be neglected.

Computational mesh employed in Chapter 5

A

The computational mesh of Chapter 5 contains around 100,000 cells at bottom dead center (BDC), including the intake and exhaust manifolds and cylinder. It was generated by using the Ansys ICEM mesher. The cylinder geometry features the whole combustion chamber and head, including both intake and exhaust ports, each one with its corresponding canted valve in almost closed position, as shown in Figure A.1.

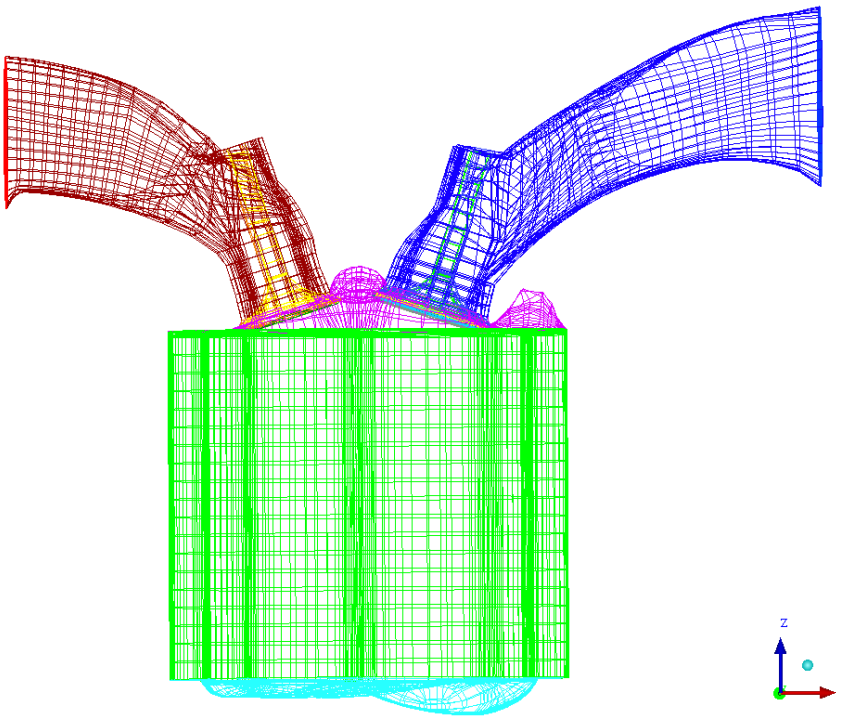

Figure A.1: Computational mesh of the SI engine with pent-roof and bowl piston. 100,000 cells at BDC including intake and exhaust manifolds and valves.

Two longitudinal cross-sections of the 3-D grid are reported in Figure A.2, belonging to the x-z and y-z plane, respectively.

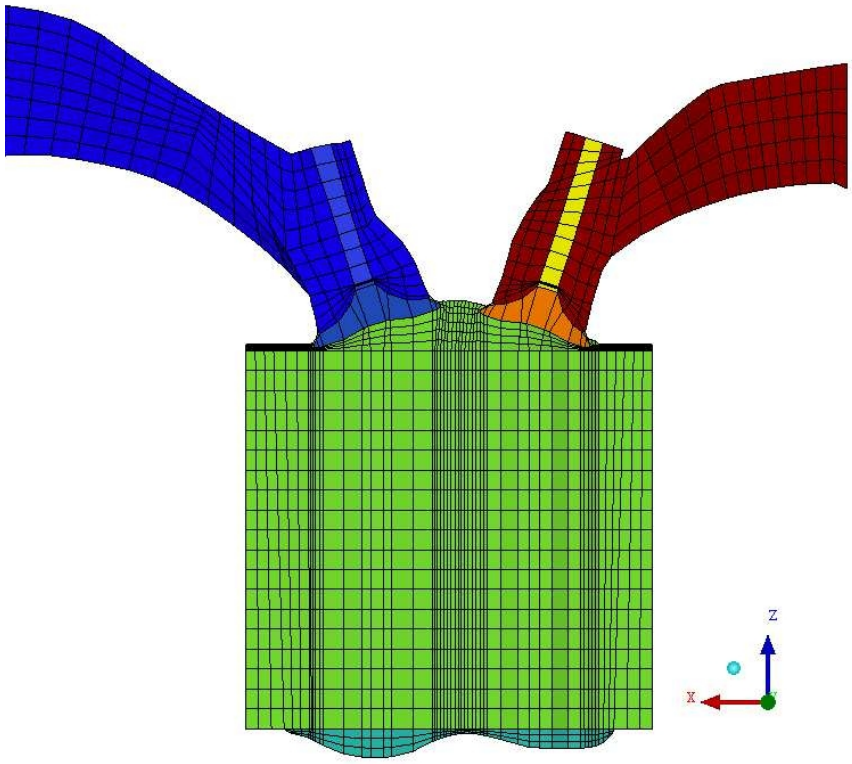

(a)

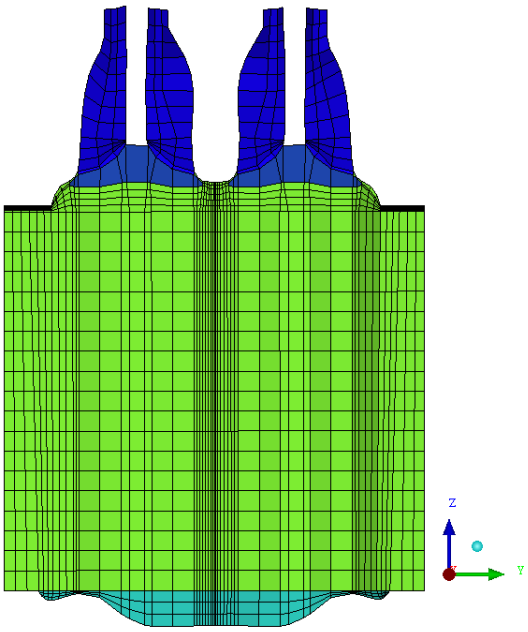

(b)

Figure A.2: Cross-sections on x-z (a) and y-z (b) planes.

Details about the mesh structure in correspondence of the valves, the cylinder head and the bowl piston are provided in Figure A.3.

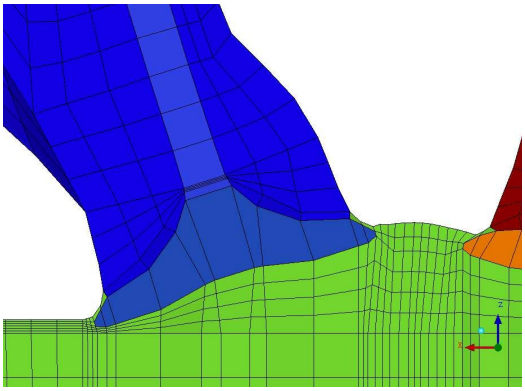

(a)

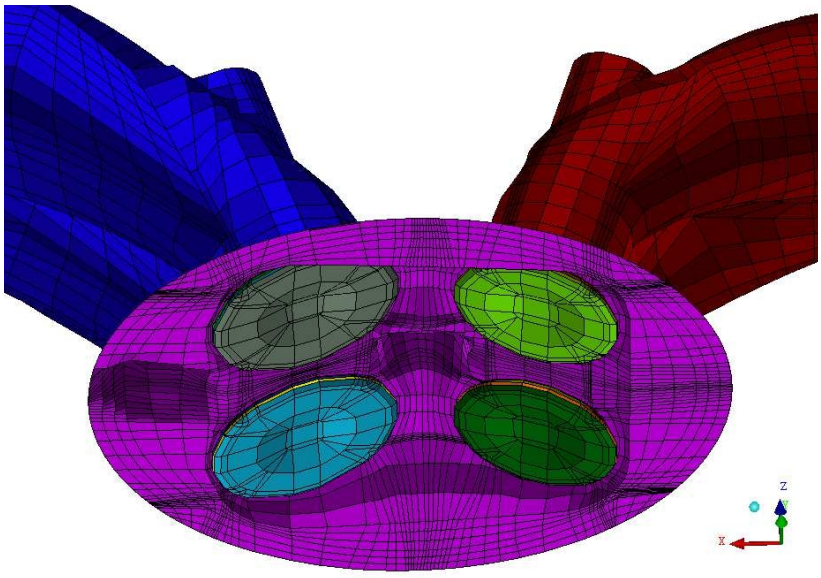

(b)

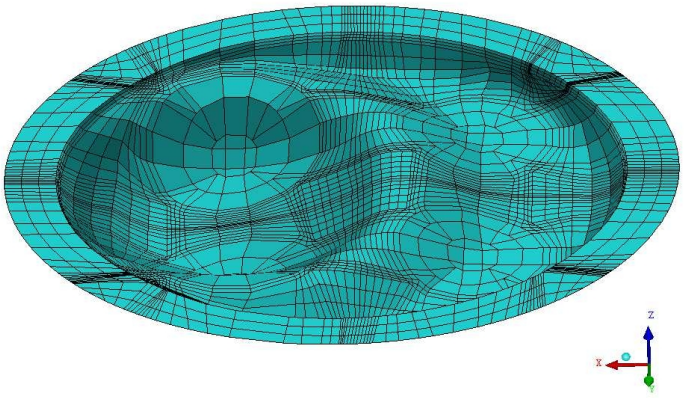

(c)

Figure A.3: Intake valve detail (a); views of the head (b) and the bowl piston (c).

Bibliography

[1] Alaswad, A., Baroutaji, A., and Olabi, A. G. *Application of Fuel Cell Technologies in the Transport Sector. Current Challenges and Developments. State of the Art on Energy Developments*, 2015. volume 11:251.

[2] Amirante, R., Cassone, E., Distaso, E., and Tamburrano, P. *Overview on recent developments in energy storage: Mechanical, electrochemical and hydrogen technologies. Energy Conversion and Management*, 2017. volume 132:372–387. ISSN 01968904. doi:10.1016/j.enconman.2016.11.046.

[3] Gao, D., Jin, Z., Zhang, J., Li, J., and Ouyang, M. *Development and performance analysis of a hybrid fuel cell/battery bus with an axle integrated electric motor drive system. International Journal of Hydrogen Energy*, 2016. volume 41(2):1161–1169.

[4] Lave, L. B. and Maclean, H. L. *An environmental-economic evaluation of hybrid electric vehicles : Toyota's Prius vs. its conventional internal combustion engine Corolla. Transportation Research Part D: Transport and Environment*, 2002. volume 7:155–162.

[5] Hofmann, P., Hofherr, T., Hoffmann, G., and Preuhs, J.-F. *Potential of CNG Direct Injection for Downsizing Engines. MTZ worldwide*, 2016. volume 77(7-8):28–35.

[6] Walker, N. R., Wissink, M. L., DelVescovo, D. A., and Reitz, R. D. *Natural Gas for High Load Dual-Fuel Reactivity Controlled Compression Ignition in Heavy-Duty Engines. Journal of Energy Resources Technology*, 2015. volume 137(4):42202. ISSN 0195-0738. doi:10.1115/1.4030110.

[7] Wermuth, N., Najt, P. M., and Yun, H. *Control strategy for transitions between homogeneous-charge compression-ignition and spark-ignition combustion modes. US Patent 8,955,492*, 2015.

[8] Amirante, R., Casavola, C., Distaso, E., and Tamburrano, P. *Towards the Development of the In-Cylinder Pressure Measurement Based on the Strain Gauge Technique for Internal Combustion Engines Operating Principles of the Proposed Strain. SAE Technical Paper*, 2015. (2015-24-2419). doi:10.4271/2015-24-2419.

[9] Benajes, J., Molina, S., Garcia, A., Monsalve-Serrano, J., and Durrett, R. *Performance and engine-out emissions evaluation of the double injection strategy applied to the gasoline partially premixed compression ignition spark assisted combustion concept. Applied Energy*, 2014. volume 134:90–101.

[10] Zhuang, H., Hung, D., Xu, M., Chen, H., Li, T., Zhang, Y., Yang, J., and Men, Y. *Flame area correlations with heat release at early flame development of combustion process in a spark-ignition direct-injection engine using gasoline, ethanol and butanol. SAE Technical Papers*, 2013. volume 11. doi:10.4271/2013-01-2637.

[11] Amirante, R., Distaso, E., Tamburrano, P., and Reitz, R. D. *Measured and Predicted Soot Particle Emissions from Natural Gas Engines. SAE Technical Paper*, 2015. (2015-24-2518). doi:10.4271/2015-24-2518.

[12] Karavalakis, G., Hajbabaei, M., Jiang, Y., Yang, J., Johnson, K. C., Cocker, D. R., and Durbin, T. D. *Regulated, greenhouse gas, and particulate emissions from lean-burn and stoichiometric natural gas heavy-duty vehicles on different fuel compositions. Fuel*, 2016. volume 175:146–156. ISSN 00162361. doi:10.1016/j.fuel.2016.02.034.

[13] Mctaggart-cowan, G. P., Rogak, S. N., Munshi, S. R., Hill, P. G., and Bushe, W. K. *The influence of fuel composition on a heavy-duty , natural-gas direct-injection engine. Fuel*, 2010. volume 89(3):752–759. ISSN 0016-2361. doi:10.1016/j.fuel.2009.10.007.

[14] Cho, H. M. and He, B. Q. *Spark ignition natural gas engines-A review. Energy Conversion and Management*, 2007. volume 48(2):608–618. ISSN 01968904. doi:10.1016/j.enconman.2006.05.023.

[15] Korakianitis, T., Namasivayam, A. M., and Crookes, R. J. *Natural-gas fueled spark-ignition (SI) and compression-ignition (CI) engine performance and emissions. Progress in Energy and Combustion Science*, 2011. volume 37(1):89–112. ISSN 03601285. doi:10.1016/j.pecs.2010.04.002.

[16] Hallquist, Å. M., Jerksjö, M., Fallgren, H., Westerlund, J., and Sjödin, Å. *Particle and gaseous emissions from individual diesel and CNG buses. Atmospheric Chemistry and Physics*, 2013. volume 13(10):5337–5350. ISSN 16807316. doi:10.5194/acp-13-5337-2013.

[17] Richards, G. A., McMillian, M. M., Gemmen, R. S., Rogers, W. A., and Cully, S. R. *Issues for low-emission, fuel-flexible power systems. Progress in Energy and Combustion Science*, 2001. volume 27(2):141–169. ISSN 03601285. doi:10.1016/S0360-1285(00)00019-8.

[18] Huang, J. and Bushe, W. K. *Experimental and kinetic study of autoignition in methane/ethane/air and methane/propane/air mixtures under engine-relevant conditions. Combustion and Flame*, 2006. volume 144:74–88. doi:10.1016/j.combustflame.2005.06.013.

[19] Aesoy, V. and Valland, H. *The influence of natural gas composition on ignition in a direct injection gas engine using hot surface assisted compression ignition. SAE Technical Paper*, 1996. (961934).

[20] Feist, M. D., Landau, M., and Harte, E. *The Effect of Fuel Composition on Performance and Emissions of a Variety of Natural Gas Engines. SAE International Journal of Fuels and Lubricants*, 2010. volume 3(2):100–117. doi:10.4271/2010-01-1476.

[21] Hajbabaei, M., Karavalakis, G., Johnson, K. C., Lee, L., and Durbin, T. D. *Impact of natural gas fuel composition on criteria, toxic, and particle emissions from transit buses equipped with lean burn and stoichiometric engines. Energy*, 2013. volume 62:425–434. ISSN 03605442. doi:10.1016/j.energy.2013.09.040.

[22] Dirrenberger, P., Gall, L., Bounaceur, R., Herbinet, O., Glaude, P.-a., Konnov, A., and Battin-leclerc, F. *Measurements of Laminar Flame Velocity for Components of Natural Gas. Energy & fuels*, 2011. volume 25(9):3875–3884.

[23] Khalil, E. B. and Karim, G. A. *A Kinetic Investigation of the Role of Changes in the Composition of Natural Gas in Engine. Transactions-American Society of Mechanical Engineeringr Journal of Engineering for Gas Turbines and Power*, 2002. volume 124(2):404–411. doi:10.1115/1.1445438.

[24] Petersen, E. L., Kalitan, D. M., Simmons, S., Bourque, G., Curran, H. J., and Simmie, J. M. *Methane/propane oxidation at high pressures: Experimental and detailed chemical kinetic modeling. Proceedings of the Combustion Institute*, 2007. volume 31 I:447–454. ISSN 15407489. doi:10.1016/j.proci.2006.08.034.

[25] Balki, M. K., Sayin, C., and Canakci, M. *The effect of different alcohol fuels on the performance, emission and combustion characteristics of a gasoline engine. Fuel*, 2014. volume 115:901–906.

[26] Catapano, F., Di Iorio, S., Magno, A., Sementa, P., and Vaglieco, B. M. *A comprehensive analysis of the effect of ethanol, methane and methane-hydrogen blend on the combustion process in a PFI (port fuel injection) engine. Energy*, 2015. volume 88:101–110.

[27] Kim, N., Cho, S., and Min, K. *A study on the combustion and emission characteristics of an SI engine under full load conditions with ethanol port injection and gasoline direct injection. Fuel*, 2015. volume 158:725–732.

[28] Masum, B. M., Masjuki, H. H., Kalam, M. A., Fattah, I. M. R., Palash, S. M., and Abedin, M. J. *Effect of ethanol–gasoline blend on NOx emission in SI engine. Renewable and Sustainable Energy Reviews*, 2013. volume 24:209–222.

[29] Tran, L. S., Sirjean, B., Glaude, P.-A., Fournet, R., and Battin-Leclerc, F. *Progress in detailed kinetic modeling of the combustion of oxygenated components of biofuels. Energy*, 2012. volume 43(1):4–18.

[30] Fisher, E. M., Pitz, W. J., Curran, H. J., and Westbrook, C. K. *Detailed chemical kinetic mechanisms for combustion of oxygenated fuels. Proceedings of the combustion institute*, 2000. volume 28(2):1579–1586.

[31] Ogawa, H., Miyamoto, N., and Yagi, M. *Chemical-kinetic analysis on PAH formation mechanisms of oxygenated fuels. SAE Technical Paper*, 2003. (2003-01-3190). doi:10.4271/2003-01-3190.

[32] Jacobs, L., Nawrot, T. S., De Geus, B., Meeusen, R., Degraeuwe, B., Bernard, A., Sughis, M., Nemery, B., and Panis, L. I. *Subclinical responses in healthy cyclists briefly exposed to traffic-related air pollution: an intervention study. Environmental Health*, 2010. volume 9(1):1.

[33] Su, D. S., Serafino, A., Müller, J.-O., Jentoft, R. E., Schlögl, R., and Fiorito, S. *Cytotoxicity and inflammatory potential of soot particles of low-emission diesel engines. Environmental science & technology*, 2008. volume 42(5):1761–1765.

[34] Brugge, D., Durant, J. L., and Rioux, C. *Near-highway pollutants in motor vehicle exhaust: a review of epidemiologic evidence of cardiac and pulmonary health risks. Environmental Health*, 2007. volume 6(1):1.

[35] Pope III, C. A. and Dockery, D. W. *Health effects of fine particulate air pollution: lines that connect. Journal of the air & waste management association*, 2006. volume 56(6):709–742.

[36] Riediker, M., Cascio, W. E., Griggs, T. R., Herbst, M. C., Bromberg, P. A., Neas, L., Williams, R. W., and Devlin, R. B. *Particulate matter exposure in cars is associated with cardiovascular effects in healthy young men. American journal of respiratory and critical care medicine*, 2004. volume 169(8):934–940.

[37] Bischof, O. F. *Recent Developments in the Measurement of Low Particulate Emissions from Mobile Sources: A Review of Particle Number Legislations. Emission Control Science and Technology*, 2015. volume 1(2):203–212.

[38] Andersson, J., Mamakos, A., Giechaskiel, B., Carriero, M., and Martini, G. *Particle measurement programme (pmp) heavy-duty inter-laboratory correlation exercise (ilce_hd) final report. Final Report. Joint Research Center, Ispra (VA). EUR*, 2010. volume 24561.

[39] Eastwood, P. *Particulate emissions from vehicles*, volume 20. John Wiley & Sons, 2008.

[40] Thiruvengadam, A., Besch, M. C., Yoon, S., Collins, J., Kappanna, H., Carder, D. K., Ayala, A., Herner, J., and Gautam, M. *Characterization of particulate matter emissions from a current technology natural gas engine. Environmental science & technology*, 2014. volume 48(14):8235–8242.

[41] Distaso, E. *Particle number analysis on heavy-duty,* EURO VI*, engine fuelled with compressed natural gas. Thesis, C.R.F. - Polytechnic of Bari*, 2013.

[42] Kennedy, I. M. *Models of soot formation and oxidation. Progress in Energy and Combustion Science*, 1997. volume 23(2):95–132.

[43] Richter, H. and Howard, J. B. *Formation of polycyclic aromatic hydrocarbons and their growth to soot—a review of chemical reaction pathways. Progress in Energy and Combustion science*, 2000. volume 26(4):565–608.

[44] Stanmore, B. R., Brilhac, J.-F., and Gilot, P. *The oxidation of soot: a review of experiments, mechanisms and models. Carbon*, 2001. volume 39(15):2247–2268.

[45] Akinlua, A., Torto, N., Ajayi, T., and Oyekunle, J. *Trace metals characterisation of niger delta kerogens. Fuel*, 2007. volume 86(10):1358–1364.

[46] Kittelson, D. B. *Engines and nanoparticles: a review. Journal of aerosol science*, 1998. volume 29(5):575–588.

[47] Seshadri, K. and Peters, N. *The inner structure of methane-air flames. Combustion and Flame*, 1990. volume 81(2):96–118.

[48] Peters, N. *Length scales in laminar and turbulent flames. Numerical approaches to combustion modeling(A 92-16977 04-25). Washington, DC, American Institute of Aeronautics and Astronautics, Inc., 1991,*, 1991. pp. 155–182.

[49] Peters, N. *Kinetic foundation of thermal flame theory. Advances in combustion science: In honor of Ya. B. Zel'dovich(A 97-24531 05-25), Reston, VA, American Institute of Aeronautics and Astronautics, Inc.(Progress in Astronautics and Aeronautics.*, 1997. volume 173:73–91.

[50] Peters, N. *The turbulent burning velocity for large-scale and small-scale turbulence. Journal of Fluid mechanics*, 1999. volume 384:107–132.

[51] Abraham, J., Williams, F. A., and Bracco, F. V. *A discussion of turbulent flame structure in premixed charges. SAE Technical Paper*, 1985. (850345).

[52] Tan, Z. *Multi-dimensional modeling of ignition and combustion in premixed and DIS/CI (direct injection spark/compression ignition) engines.* Doctoral Dissertation, University of Wisconsin–Madison, 2003.

[53] Chen, Y.-C. and Bilger, R. W. *Experimental investigation of three-dimensional flame-front structure in premixed turbulent combustion—i: hydrocarbon/air bunsen flames. Combustion and flame*, 2002. volume 131(4):400–435.

[54] Haworth, D., Blint, R., Cuenot, B., and Poinsot, T. *Numerical simulation of turbulent propane–air combustion with nonhomogeneous reactants. Combustion and Flame*, 2000. volume 121(3):395–417.

[55] Haworth, D. C. *A review of turbulent combustion modeling for multidimensional in-cylinder cfd. SAE Technical Paper*, 2005. (2005-01-0993).

[56] Peters, N. *Turbulent combustion.* Cambridge university press, 2000.

[57] Herrmann, M. G. *Numerical simulation of premixed turbulent combustion based on a level set flamelet model.* Shaker, 2001.

[58] Turner, S. *An introduction to combustion, concepts and applications.* McGraw-Hill, New York City, 1972.

[59] Curran, H. J., Gaffuri, P., Pitz, W., and Westbrook, C. *A comprehensive modeling study of iso-octane oxidation. Combustion and flame*, 2002. volume 129(3):253–280.

[60] Farrell, J. T., Johnston, R. J., and Androulakis, I. P. *Molecular structure effects on laminar burning velocities at elevated temperature and pressure. SAE Technical Paper*, 2004. (2004-01-2936).

[61] Tanaka, S., Ayala, F., and Keck, J. C. *A reduced chemical kinetic model for hcci combustion of primary reference fuels in a rapid compression machine. Combustion and flame*, 2003. volume 133(4):467–481.

[62] Patel, A., Kong, S.-C., and Reitz, R. D. *Development and validation of a reduced reaction mechanism for hcci engine simulations. SAE Technical Paper*, 2004. (2004-01-0558).

[63] Fieweger, K., Blumenthal, R., and Adomeit, G. *Self-ignition of si engine model fuels: a shock tube investigation at high pressure. Combustion and Flame*, 1997. volume 109(4):599–619.

[64] Metghalchi, M. and Keck, J. C. *Burning Velocities of Mixture of Air with Methanol, Iso-Octane and Indolene at High Pressure and Temperature. Combustion and Flame*, 1982. volume 210:191–210.

[65] Liang, L., Reitz, R. D., Yi, J., and Iyer, C. O. *A g-equation combustion model incorporating detailed chemical kinetics for pfi/di si engine simulations. SAE Congress April*, 2006. volume 2.

[66] Kong, S.-C. and Reitz, R. D. *Application of detailed chemistry and cfd for predicting direct injection hcci engine combustion and emissions. Proceedings of the Combustion Institute*, 2002. volume 29(1):663–669.

[67] Kong, S.-C., Sun, Y., and Rietz, R. D. *Modeling diesel spray flame liftoff, sooting tendency, and nox emissions using detailed chemistry with phenomenological soot model. Journal of Engineering for Gas Turbines and Power*, 2007. volume 129(1):245–251.

[68] Han, Z. and Reitz, R. D. *A temperature wall function formulation for variable-density turbulent flows with application to engine convective heat transfer modeling. International journal of heat and mass transfer*, 1997. volume 40(3):613–625.

[69] Liang, L. and Reitz, R. D. *Spark ignition engine combustion modeling using a level set method with detailed chemistry. SAE Technical Paper*, 2006. (2006-01-0243).

[70] Tesner, P., Tsygankova, E., Guilazetdinov, L., Zuyev, V., and Loshakova, G. *The formation of soot from aromatic hydrocarbons in diffusion flames of hydrocarbon-hydrogen mixtures. Combustion and Flame*, 1971. volume 17(3):279–285.

[71] Surovikin, V. *Analytical description of the processes of nucleus-formation and growth of particles of carbon black in the thermal decomposition of aromatic hydrocarbons in the gas phase. Khimiya Tverdogo Topliva*, 1976. volume 10(1):111–122.

[72] Hiroyasu, H., Kadota, T., and Arai, M. *Development and use of a spray combustion modeling to predict diesel engine efficiency and pollutant emissions: Part 1 combustion modeling. Bulletin of JSME*, 1983. volume 26(214):569–575.

[73] Moss, J., Stewart, C., and Young, K. *Modeling soot formation and burnout in a high temperature laminar diffusion flame burning under oxygen-enriched conditions. Combustion and Flame*, 1995. volume 101(4):491–500.

[74] Leung, K. M., Lindstedt, R. P., and Jones, W. *A simplified reaction mechanism for soot formation in nonpremixed flames. Combustion and flame*, 1991. volume 87(3):289–305.

[75] Kent, J. and Wagner, H. G. *Soot measurements in laminar ethylene diffusion flames. Combustion and Flame*, 1982. volume 47:53–65.

[76] Markatou, P., Wang, H., and Frenklach, M. *A computational study of sooting limits in laminar premixed flames of ethane, ethylene, and acetylene. Combustion and flame*, 1993. volume 93(4):467–482.

[77] Pitsch, H., Riesmeier, E., and Peters, N. *Unsteady flamelet modeling of soot formation in turbulent diffusion flames. Combustion science and technology*, 2000. volume 158(1):389–406.

[78] Hong, S., Wooldridge, M. S., Im, H. G., Assanis, D. N., and Pitsch, H. *Development and application of a comprehensive soot model for 3d cfd reacting flow studies in a diesel engine. Combustion and Flame*, 2005. volume 143(1):11–26.

[79] Celnik, M., Raj, A., West, R., Patterson, R., and Kraft, M. *Aromatic site description of soot particles. Combustion and Flame*, 2008. volume 155(1):161–180.

[80] Mosbach, S., Celnik, M. S., Raj, A., Kraft, M., Zhang, H. R., Kubo, S., and Kim, K.-O. *Towards a detailed soot model for internal combustion engines. Combustion and Flame*, 2009. volume 156(6):1156–1165.

[81] Amsden, A. A., O'rourke, P., and Butler, T. *Kiva-ii: A computer program for chemically reactive flows with sprays. Los Alamos National Lab., NM (USA)*, 1989. (LA-11560-MS).

[82] Amsden, A. A. and Menon, R. *Kiva3. a kiva program with block-structured mesh for complex geometries. Silicon Graphics Computer Systems, Mountain View, CA (United States)*, 1993. (ESTSC-000154SGSUP00).

[83] Amsden, A. A. *Kiva-3v: A block-structured kiva program for engines with vertical or canted valves. Los Alamos National Lab., NM (United States)*, 1997. (ESTSC-000154MLTPL01).

[84] Perini, F., Galligani, E., and Reitz, R. D. *An analytical Jacobian approach to sparse reaction kinetics for computationally efficient combustion modeling with large reaction mechanisms. Energy and Fuels*, 2012. volume 26(8):4804–4822. ISSN 08870624. doi:10.1021/ef300747n.

[85] Kong, S.-C., Marriott, C. D., Reitz, R. D., and Christensen, M. *Modeling and experiments of hcci engine combustion using detailed chemical kinetics with multidimensional cfd. SAE Technical paper*, 2001. (2001-01-1026).

[86] Millo, F. and Ferraro, C. V. *Knock in si engines: a comparison between different techniques for detection and control. SAE Technical paper*, 1998. (982477).

[87] Vishwanathan, G. and Reitz, R. D. *Development of a practical soot modeling approach and its application to low-temperature diesel combustion. Combustion Science and Technology*, 2010. volume 182(8):1050–1082. doi:10.1080/00102200903548124.

[88] Jiao, Q. and Reitz, R. *Modeling of equivalence ratio effects on particulate formation in a spark-ignition engine under premixed conditions. SAE 2014 World Congress and Exhibition*, 2014. volume 1. doi:10.4271/2014-01-1607.

[89] Fan, L. and Reitz, R. *Development of an ignition and combustion model for spark ignition engines. SAE Technical paper*, 2000. (2000-01-2809).

[90] Tan, Z. and Reitz, R. D. *Modeling Ignition and Combustion in Spark-ignition Engines Using a Level Set Method. SAE Technical Paper 2003-01-0722*, 2003. doi:10.4271/2003-01-0722.

[91] Wang, B.-L., Lee, C.-W., Reitz, R. D., Miles, P. C., and Han, Z. *A generalized renormalization group turbulence model and its application to a light-duty diesel engine operating in a low-temperature combustion regime. International Journal of Engine Research*, 2013. volume 14(3):279–292.

[92] Ra, Y., Reitz, R. D., Jarrett, M. W., and Shyu, T. *Effects of piston crevice flows and lubricant oil vaporization on diesel engine deposits. SAE Technical paper*, 2006. (2006-01-1149).

[93] Peters, N. and Dekena, M. *Combustion modeling with the g-equation. Oil & Gas Science and Technology*, 1999. volume 54(2):265–270.

[94] Tan, Z., Kong, S.-C., and Reitz, R. D. *Modeling Premixed and Direct Injection SI Engine Combustion Using the G-Equation Model. SAE Technical Paper*, 2003. ISSN 0148-7191. doi:10.4271/2003-01-1843.

[95] Ewald, J. and Peters, N. *A level set based flamelet model for the prediction of combustion in spark ignition engines. 15th International Multidimensional Engine Modeling User's Group Meeting, Detroit, MI*, 2005.

[96] Han, Z., Weaver, C., Wooldridge, S., Alger, T., Hilditch, J., McGee, J., Westrate, B., Xu, Z., Yi, J., Chen, X., et al. *Development of a new light stratified-charge disi combustion system for a family of engines with upfront cfd coupling with thermal and optical engine experiments. SAE Technical Paper*, 2004. (2004-01-0545).

[97] Smooke, M. D. *Reduced kinetic mechanisms and asymptotic approximations for methane-air flames: a topical volume.* In *Reduced Kinetic Mechanisms and Asymptotic Approximations for Methane-Air Flames*, volume 384. 1991 .

[98] Göttgens, J., Mauss, F., and Peters, N. *Analytic approximations of burning velocities and flame thicknesses of lean hydrogen, methane, ethylene, ethane, acetylene, and propane flames.* In *Symposium (International) on Combustion*, volume 24. Elsevier, 1992 pp. 129–135.

[99] Müller, U., Bollig, M., and Peters, N. *Approximations for burning velocities and markstein numbers for lean hydrocarbon and methanol flames. Combustion and Flame*, 1997. volume 108(3):349–356.

[100] Heywood, J. B. et al. *Internal combustion engine fundamentals*, volume 930. Mcgraw-hill New York, 1988.

[101] Kravchik, T., Sher, E., and Heywood, J. *From spark ignition to flame initiation. Combustion science and technology*, 1995. volume 108(1-3):1–30.

[102] Herweg, R. and Maly, R. *A fundamental model for flame kernel formation in si engines. SAE Technical Paper*, 1992. (922243).

[103] Jiao, Q. and Reitz, R. D. *Modeling soot emissions from wall films in a direct-injection spark-ignition engine. International Journal of Engine Research*, 2014. volume 16(8):1468087414562008–. ISSN 1468-0874. doi:10.1177/1468087414562008.

[104] Leung, K. M., Lindstedt, R. P., and Jones, W. *A simplified reaction mechanism for soot formation in nonpremixed flames. Combustion and flame*, 1991. volume 87(3):289–305.

[105] Singh, S., Liang, L., Kong, S.-C., and Reitz, R. D. *Development of a Flame Propagation Model for Dual-Fuel Partially Premixed Compression Ignition Engines. International Journal of Engine Research*, 2006. volume 7(1):65–75. ISSN 1468-0874. doi:10.1243/146808705X7464.

[106] Perini, F., Ra, Y., Hiraoka, K., Nomura, K., Yuuki, A., Oda, Y., Rutland, C., and Reitz, R. *An Efficient Level-Set Flame Propagation Model for Hybrid Unstructured Grids Using the G-Equation. SAE International Journal of Engines*, 2016. volume 9(3):582–2016. ISSN 1946-3944. doi:10.4271/2016-01-0582.

[107] Buckmaster, J., Clavin, P., Liñán, A., Matalon, M., Peters, N., Sivashinsky, G., and Williams, F. A. *Combustion theory and modeling. Proceedings of the Combustion Institute*, 2005. volume 30(1):1–19. ISSN 15407489. doi:10.1016/j.proci.2004.08.280.

[108] Brandl, A., Pfitzner, M., Mooney, J. D., Durst, B., and Kern, W. *Comparison of combustion models and assessment of their applicability to the simulation of premixed turbulent combustion in IC-engines. Flow, Turbulence and Combustion*, 2005. volume 75(1-4):335–350. ISSN 13866184. doi:10.1007/s10494-005-8584-3.

[109] Veynante, D. and Vervisch, L. *Turbulent combustion modeling. Progress in Energy and Combustion Science*, 2002. volume 28(3):193–266. ISSN 03601285. doi:10.1016/S0360-1285(01)00017-X.

[110] Gülder, Ö. L. *Correlations of laminar combustion data for alternative SI engine fuels. SAE Technical paper*, 1984. (841000).

[111] Ranzi, E., Frassoldati, A., Grana, R., Cuoci, A., Faravelli, T., Kelley, A. P., and Law, C. K. *Hierarchical and comparative kinetic modeling of laminar flame speeds of hydrocarbon and oxygenated fuels. Progress in Energy and Combustion Science*, 2012. volume 38(4):468–501. ISSN 03601285. doi:10.1016/j.pecs.2012.03.004.

[112] Metghalchi, M. and Keck, J. *Laminar burning velocity of propane-air mixtures at high temperature and pressure. Combustion and Flame*, 1980. volume 38:143–154. ISSN 00102180. doi:10.1016/0010-2180(80)90046-2.

[113] Hu, E., Li, X., Meng, X., Chen, Y., Cheng, Y., Xie, Y., and Huang, Z. *Laminar flame speeds and ignition delay times of methane-air mixtures at elevated temperatures and pressures. Fuel*, 2015. volume 158:1–10. ISSN 00162361. doi:10.1016/j.fuel.2015.05.010.

[114] Sileghem, L., Alekseev, V. A., Vancoillie, J., Van Geem, K. M., Nilsson, E. J. K., Verhelst, S., and Konnov, A. A. *Laminar burning velocity of gasoline and the gasoline surrogate components iso-octane, n-heptane and toluene. Fuel*, 2013. volume 112:355–365. ISSN 00162361. doi:10.1016/j.fuel.2013.05.049.

[115] Wu, C. K. and Law, C. K. *On the determination of laminar flame speeds from stretched flames.* In *Symposium (International) on Combustion*, volume 20. Elsevier, 1985 pp. 1941–1949.

[116] Lavoie, G. *Correlations of Combustion Data for SI Engine Calculations- Laminar Flame Speed, Quench Distance and Global Reaction Rates. SAE Technical Paper 780229*, 1978. doi:10.4271/780229.

[117] Ryan, T. W. and Lestz, S. S. *The laminar burning velocity of isooctane, n-heptane, methanol, methane, and propane at elevated temperature and pressures in the presence of a diluent. SAE Technical Paper*, 1980. (800103).

[118] Dugger, G. L. *Effect of initial mixture temperature on flame speed of methane-air, propane-air, and ethylene-air mixtures.* 1952.

[119] Gu, X. J., Haq, M. Z., Lawes, M., and Woolley, R. *Laminar burning velocity and Markstein lengths of methane–air mixtures. Combustion and flame*, 2000. volume 121(1):41–58.

[120] Gülder, O. L. *Burning velocities of ethanol–air and ethanol–water–air mixtures. AIAA Progr Astronaut Aeronaut*, 1984. volume 95:181–197.

[121] Koda, S., Oda, K., Hirano, M., Hirano, T., and Akita, K. *Burning characteristics of methanol/water air mixtures in a constant volume combustion vessel. Combustion and flame*, 1982. volume 46:17–28.

[122] Van Tiggelen, A. and Deckers, J. *Chain branching and flame propagation.* In *Symposium (International) on Combustion*, volume 6. Elsevier, 1957 pp. 61–66.

[123] Ferguson, C. R. and Keck, J. C. *On laminar flame quenching and its application to spark ignition engines. Combustion and Flame*, 1977. volume 28:197–205.

[124] Tabaczynski, R. J., Ferguson, C. R., and Radhakrishnan, K. *A turbulent entrainment model for spark-ignition engine combustion. SAE Technical Paper*, 1977. (770647).

[125] Tanford, C. *The role of free atoms and radicals in burner flames.* In *Symposium on Combustion and Flame, and Explosion Phenomena*, volume 3. Elsevier, 1948 pp. 140–146.

[126] Andrews, G. E. and Bradley, D. *The burning velocity of methane-air mixtures. Combustion and Flame*, 1972. volume 19(2):275–288.

[127] Elia, M., Ulinski, M., and Metghalchi, M. *Laminar Burning Velocity of Methane–Air–Diluent Mixtures. Journal of Engineering for Gas Turbines and Power*, 2001. volume 123(1):190. ISSN 07424795. doi:10.1115/1.1339984.

[128] Han, P., Checkel, M. D., Fleck, B. A., and Nowicki, N. L. *Burning velocity of methane/diluent mixture with reformer gas addition. Fuel*, 2007. volume 86(4):585–596.

[129] Ouimette, P. and Seers, P. *Numerical comparison of premixed laminar flame velocity of methane and wood syngas. Fuel*, 2009. volume 88(3):528–533.

[130] Liao, S. Y., Jiang, D. M., and Cheng, Q. *Determination of laminar burning velocities for natural gas. Fuel*, 2004. volume 83(9):1247–1250. ISSN 00162361. doi:10.1016/j.fuel.2003.12.001.

[131] Huzayyin, A. S., Moneib, H. A., Shehatta, M. S., and Attia, A. M. A. *Laminar burning velocity and explosion index of LPG–air and propane–air mixtures. Fuel*, 2008. volume 87(1):39–57.

[132] Choi, M., Song, J., and Park, S. *Modeling of the fuel injection and combustion process in a CNG direct injection engine. Fuel*, 2016. volume 179:168–178.

[133] Shiga, S., Ozone, S., Machacon, H. T. C., Karasawa, T., Nakamura, H., Ueda, T., Jingu, N., Huang, Z., Tsue, M., and Kono, M. *A study of the combustion and emission characteristics of compressed-natural-gas direct-injection stratified combustion using a rapid-compression-machine. Combustion and Flame*, 2002. volume 129(1):1–10.

[134] Zeng, K., Huang, Z., Liu, B., Liu, L., Jiang, D., Ren, Y., and Wang, J. *Combustion characteristics of a direct-injection natural gas engine under various fuel injection timings. Applied thermal engineering*, 2006. volume 26(8):806–813.

[135] Goswami, M., Derks, S. C. R., Coumans, K., Slikker, W. J., de Andrade Oliveira, M. H., Bastiaans, R. J. M., Luijten, C. C. M., de Goey, L. P. H., and Konnov, A. A. *The effect of elevated pressures on the laminar burning velocity of methane+ air mixtures. Combustion and Flame*, 2013. volume 160(9):1627–1635.

[136] Rallis, C. J. and Garforth, A. M. *The determination of laminar burning velocity. Progress in Energy and Combustion Science*, 1980. volume 6(4):303–329.

[137] Coppens, F. H. V., De Ruyck, J., and Konnov, A. A. *The effects of composition on burning velocity and nitric oxide formation in laminar premixed flames of CH 4+ H 2+ O 2+ N 2. Combustion and Flame*, 2007. volume 149(4):409–417.

[138] Pitz, W. J., Cernansky, N. P., Dryer, F. L., Egolfopoulos, F. N., Farrell, J. T., Friend, D. G., and Pitsch, H. *Development of an Experimental Database and Chemical Kinetic Models for Surrogate Gasoline Fuels. SAE Technical Paper*, 2007. volume 2007-01(724):0175. ISSN 0148-7191. doi:10.4271/2007-01-0175.

[139] Dirrenberger, P., Glaude, P.-A., Bounaceur, R., Le Gall, H., da Cruz, A. P., Konnov, A. A., and Battin-Leclerc, F. *Laminar burning velocity of gasolines with addition of ethanol. Fuel*, 2014. volume 115:162–169.

[140] Zhao, Z., Conley, J. P., Kazakov, a., and Dryer, F. L. *Burning velocities of real gasoline fuel at 353 K and 500 K. SAE-transactions*, 2003. volume 112(724):2624–2629. ISSN 0148-7191. doi:10.4271/2003-01-3265.

[141] Takashi, H. and Kimitoshi, T. *Laminar flame speeds of ethanol, n-heptane, iso-octane air mixtures. JSAE paper*, 2006. (20068518).

[142] Hassan, M. I., Aung, K. T., and Faeth, G. M. *Measured and predicted properties of laminar premixed methane/air flames at various pressures. Combustion and Flame*, 1998. volume 115(4):539–550.

[143] Rozenchan, G., Zhu, D. L., Law, C. K., and Tse, S. D. *Outward propagation, burning velocities, and chemical effects of methane flames up to 60 atm. Proceedings of the Combustion Institute*, 2002. volume 29(2):1461–1470.

[144] Bosschaart, K. J. and De Goey, L. P. H. *The laminar burning velocity of flames propagating in mixtures of hydrocarbons and air measured with the heat flux method. Combustion and Flame*, 2004. volume 136(3):261–269. ISSN 00102180. doi:10.1016/j.combustflame.2003.10.005.

[145] Bourque, G., Healy, D., Curran, H., Zinner, C., Kalitan, D., de Vries, J., Aul, C., and Petersen, E. *Ignition and Flame Speed Kinetics of Two Natural Gas Blends With High Levels of Heavier Hydrocarbons. Journal of Engineering for Gas Turbines and Power*, 2009. volume 132(2):21504. ISSN 0742-4795. doi: 10.1115/1.3124665.

[146] Park, O., Veloo, P. S., Liu, N., and Egolfopoulos, F. N. *Combustion characteristics of alternative gaseous fuels. Proceedings of the Combustion Institute*, 2011. volume 33(1):887–894.

[147] Lowry, W., de Vries, J., Krejci, M., Petersen, E., Serinyel, Z., Metcalfe, W., Curran, H., and Bourque, G. *Laminar Flame Speed Measurements and Modeling of Pure Alkanes and Alkane Blends at Elevated Pressures. Journal of Engineering for Gas Turbines and Power*, 2011. volume 133(9):91501. ISSN 07424795. doi: 10.1115/1.4002809.

[148] Li, N., Wang, Y., Tang, D., and Zhou, H. *Integrating a Photocatalyst into a Hybrid Lithium-Sulfur Battery for Direct Storage of Solar Energy. Angewandte Chemie*, 2015. volume 127(32):9403–9406. ISSN 00448249. doi:10.1002/ange.201503425.

[149] Kuehl, D. K. *Laminar-burning velocities of propane-air mixtures.* In *Symposium (International) on Combustion*, volume 8. Elsevier, 1961 pp. 510–521.

[150] Agnew, J. and Graiff, L. *The pressure dependence of laminar burning velocity by the spherical bomb method. Combustion and Flame*, 1961. volume 5(May):209–219. ISSN 00102180. doi:10.1016/0010-2180(61)90099-2.

[151] Chase, J. D. and Weinberg, F. J. *The Acetylene Decomposition Flame and the Deduction of Reaction Mechanism from Global Flame Kinetics.* In *Proceedings of the Royal Society of London A: Mathematical, Physical and Engineering Sciences*, volume 275. The Royal Society, 1963 pp. 411–430.

[152] Vagelopoulos, C. M. and Egolfopoulos, F. N. *Direct experimental determination of laminar flame speeds.* In *Symposium (international) on combustion*, volume 27. Elsevier, 1998 pp. 513–519.

[153] Jomaas, G., Zheng, X. L., Zhu, D. L., and Law, C. K. *Experimental determination of counterflow ignition temperatures and laminar flame speeds of C 2–C 3 hydrocarbons at atmospheric and elevated pressures. Proceedings of the Combustion Institute*, 2005. volume 30(1):193–200.

[154] Tang, C., He, J., Huang, Z., Jin, C., Wang, J., Wang, X., and Miao, H. *Measurements of laminar burning velocities and Markstein lengths of propane-hydrogen-air mixtures at elevated pressures and temperatures. International Journal of Hydrogen Energy*, 2008. volume 33(23):7274–7285. ISSN 03603199. doi: 10.1016/j.ijhydene.2008.08.053.

[155] Razus, D., Oancea, D., Brinzea, V., Mitu, M., and Movileanu, C. *Experimental and computed burning velocities of propane-air mixtures. Energy Conversion and Management*, 2010. volume 51(12):2979–2984. doi:10.1016/j.enconman.2010.06.041.

[156] Wang, Q., Chen, X., Jha, A. N., and Rogers, H. *Natural gas from shale formation–the evolution, evidences and challenges of shale gas revolution in United States. Renewable and Sustainable Energy Reviews*, 2014. volume 30:1–28.

[157] Ayala, A., Kado, N., Okamoto, R., Gebel, M. R. P., Kobayashi, R., and Kuzmicky, P. *CNG and Diesel Transit Bus Emissions in Review. 9th Diesel Engine Emissions Reduction (DEER) Workshop 2003, Newport, RI (US)*, 2003. p. 6.

[158] Pratson, L. F., Haerer, D., and Patiño-Echeverri, D. *Fuel prices, emission standards, and generation costs for coal vs natural gas power plants. Environmental science & technology*, 2013. volume 47(9):4926–4933.

[159] Kishore, V. R., Duhan, N., Ravi, M. R., and Ray, A. *Measurement of adiabatic burning velocity in natural gas-like mixtures. Experimental Thermal and Fluid Science*, 2008. volume 33(1):10–16.

[160] Jerzembeck, S., Peters, N., Pepiot-Desjardins, P., and Pitsch, H. *Laminar burning velocities at high pressure for primary reference fuels and gasoline: Experimental and numerical investigation. Combustion and Flame*, 2009. volume 156(2):292–301.

[161] Tian, G., Daniel, R., Li, H., Xu, H., Shuai, S., and Richards, P. *Laminar burning velocities of 2,5-dimethylfuran compared with ethanol and gasoline. Energy and Fuels*, 2010. volume 24(7):3898–3905. ISSN 08870624. doi:10.1021/ef100452c.

[162] Zhao, F., Lai, M.-C., and Harrington, D. L. *Automotive spark-ignited direct-injection gasoline engines. Progress in energy and combustion science*, 1999. volume 25(5):437–562.

[163] Asad, U., Kumar, R., Zheng, M., and Tjong, J. *Ethanol-fueled low temperature combustion: A pathway to clean and efficient diesel engine cycles. Applied Energy*, 2015. volume 157:838–850.

[164] Nadim, F., Zack, P., Hoag, G. E., and Liu, S. *United States experience with gasoline additives. Energy Policy*, 2000. volume 29(1):1–5. ISSN 03014215. doi:10.1016/S0301-4215(00)00099-9.

[165] Yunoki, S. and Saito, M. *A simple method to determine bioethanol content in gasoline using two-step extraction and liquid scintillation counting. Bioresource technology*, 2009. volume 100(23):6125–6128.

[166] Harper, M. R., Van Geem, K. M., Pyl, S. P., Marin, G. B., and Green, W. H. *Comprehensive reaction mechanism for n-butanol pyrolysis and combustion. Combustion and Flame*, 2011. volume 158(1):16–41.

[167] Herbinet, O., Biet, J., Hakka, M. H., Warth, V., Glaude, P.-A., Nicolle, A., and Battin-Leclerc, F. *Modeling study of the low-temperature oxidation of large methyl esters from c 11 to c 19. Proceedings of the Combustion Institute*, 2011. volume 33(1):391–398.

[168] Giechaskiel, B., Chirico, R., Decarlo, P. F., Clairotte, M., Adam, T., Martini, G., Heringa, M. F., Richter, R., Prevot, A. S. H., Baltensperger, U., and Astorga, C. *Science of the Total Environment Evaluation of the particle measurement programme (PMP) protocol to remove the vehicles ' exhaust aerosol volatile phase. Science of the Total Environment, The*, 2010. volume 408(21):5106–5116. ISSN 0048-9697. doi:10.1016/j.scitotenv.2010.07.010.

[169] Zhou, J., Richard, S., Mounaïm-Rousselle, C., and Foucher, F. *Effects of controlling oxygen concentration on the performance, emission and combustion characteristics in a downsized si engine. SAE Technical paper*, 2013. (2013-24-0056).

[170] Reitz, R. D. and Kuo, T.-w. *Modeling of hc emissions due to crevice flows in premixed-charge engines. SAE Technical paper*, 1989. (892085).

[171] Jayaratne, E. R., Meyer, N. K., Ristovski, Z. D., Morawska, L., and Miljevic, B. *Critical analysis of high particle number emissions from accelerating compressed natural gas buses. Environmental Science and Technology*, 2010. volume 44(10):3724–3731. ISSN 0013936X. doi:10.1021/es1003186.

[172] Huang, Z., Wang, J., Liu, B., Zeng, K., Yu, J., and Jiang, D. *Combustion characteristics of a direct-injection engine fueled with natural gas-hydrogen blends under different ignition timings. Fuel*, 2007. volume 86(3):381–387. ISSN 00162361. doi:10.1016/j.fuel.2006.07.007.

[173] Goyal, P. and Sidhartha. *Present scenario of air quality in Delhi: A case study of CNG implementation. Atmospheric Environment*, 2003. volume 37(38):5423–5431. ISSN 13522310. doi:10.1016/j.atmosenv.2003.09.005.

[174] Liss, W., Thrasher, W., Steinmetz, G., Chowdiah, P., and Attari, A. *Variability of natural gas composition in select major metropolitan areas of the united states. GRI report*, 1992. volume 92:0123.

[175] Kakaee, A.-H., Paykani, A., and Ghajar, M. *The influence of fuel composition on the combustion and emission characteristics of natural gas fueled engines. Renewable and Sustainable Energy Reviews*, 2014. volume 38:64–78. ISSN 13640321. doi:10.1016/j.rser.2014.05.080.

[176] Karavalakis, G., Hajbabaei, M., Durbin, T. D., Johnson, K. C., Zheng, Z., and Miller, W. J. *The effect of natural gas composition on the regulated emissions, gaseous toxic pollutants, and ultrafine particle number emissions from a refuse*

hauler vehicle. Energy, 2013. volume 50(1):280–291. ISSN 03605442. doi: 10.1016/j.energy.2012.10.044.

[177] Yossefi, D., Belmont, M. R., Ashcroft, S. J., and Maskell, S. J. *A comparison of the relative effects of fuel composition and ignition energy on the early stages of combustion in a natural gas spark ignition engine using simulation. Proceedings of the Institution of Mechanical Engineers Part D-Journal of Automobile Engineering*, 2000. volume 214(D4):383–393. doi:10.1243/0954407001527709.

[178] Min, B., Bang, K., Kim, H., and Chung, J. *Effects of gas composition on the performance and hydrocarbon emissions for CNG engines. SAE Technical paper*, 1998. (981918).

[179] Stanton, D. W. *Systematic development of highly efficient and clean engines to meet future commercial vehicle greenhouse gas regulations. SAE International Journal of Engines*, 2013. volume 6(3):1395–1480.

[180] Burcat, A., Scheller, K., and Lifshitz, A. *Shock-tube investigation of comparative ignition delay times for C1-C5 alkanes. Combustion and Flame*, 1971. volume 16(1):29–33. ISSN 00102180. doi:10.1016/S0010-2180(71)80007-X.

[181] El-Sherif, a. S. *Effects of natural gas composition on the nitrogen oxide, flame structure and burning velocity under laminar premixed flame conditions. Fuel*, 1998. volume 77(14):1539–1547. ISSN 00162361. doi:10.1016/S0016-2361(98)00083-0.

[182] Caillol, C., Delorme, T., Denis, P., and Berardi, G. *A Combustion Model for Analyzing the Effects of Natural Gas Composition on the Operation of a Spark Ignition Engine. SAE Technical Paper series*, 2002. (724):1–10. doi: 10.4271/2002-01-2236.

[183] Haycock, R. F., Caines, A. J., and Hillier, J. E. *Automotive lubricants reference book*, volume 354. John Wiley & Sons, 2004.

[184] Gidney, J. T., Twigg, M. V., and Kittelson, D. B. *Effect of organometallic fuel additives on nanoparticle emissions from a gasoline passenger car. Environmental science & technology*, 2010. volume 44(7):2562–2569.

[185] McGeehan, J. A., Yeh, S., Couch, M., Hinz, A., Otterholm, B., Walker, A., and Blakeman, P. *On the road to 2010 emissions: field test results and analysis with DPF-SCR system and ultra low sulfur diesel fuel. SAE Technical Paper*, 2005. (2005-01-3716).

[186] Cheung, K. L., Ntziachristos, L., Tzamkiozis, T., Schauer, J. J., Samaras, Z., Moore, K. F., and Sioutas, C. *Emissions of particulate trace elements, metals and organic species from gasoline, diesel, and biodiesel passenger vehicles and their relation to oxidative potential. Aerosol Science and Technology*, 2010. volume 44(7):500–513.

[187] Lee, D. G., Miller, A., Park, K. H., and Zachariah, M. R. *Effects of trace metals on particulate matter formation in a diesel engine: Metal contents from ferrocene and lube oil. Int. J. Automot. Technol*, 2006. volume 7:667–673.

[188] Duffin, R., Tran, L., Brown, D., Stone, V., and Donaldson, K. *Proinflammogenic effects of low-toxicity and metal nanoparticles in vivo and in vitro: highlighting the role of particle surface area and surface reactivity. Inhalation toxicology*, 2007. volume 19(10):849–856.

[189] Wilson, M. R., Lightbody, J. H., Donaldson, K., Sales, J., and Stone, V. *Interactions between ultrafine particles and transition metals in vivo and in vitro. Toxicology and applied pharmacology*, 2002. volume 184(3):172–179.

[190] Donaldson, K., Tran, L., Jimenez, L. A., Duffin, R., Newby, D. E., Mills, N., MacNee, W., and Stone, V. *Combustion-derived nanoparticles: a review of their toxicology following inhalation exposure. Particle and fibre toxicology*, 2005. volume 2(1):1.

[191] Skillas, G., Qian, Z., Baltensperger, U., Matter, U., and Burtscher, H. *The influence of additives on the size distribution and composition of particles produced by diesel engines. Combustion science and Technology*, 2000. volume 154(1):259–273.

[192] Jung, H., Kittelson, D. B., and Zachariah, M. R. *The influence of a cerium additive on ultrafine diesel particle emissions and kinetics of oxidation. Combustion and Flame*, 2005. volume 142(3):276–288.

[193] Kasper, M., Sattler, K., Siegmann, K., Matter, U., and Siegmann, H. C. *The influence of fuel additives on the formation of carbon during combustion. Journal of Aerosol Science*, 1999. volume 30(2):217–225.

[194] Jung, H., Kittelson, D. B., and Zachariah, M. R. *The influence of engine lubricating oil on diesel nanoparticle emissions and kinetics of oxidation. SAE Technical Paper*, 2003. (2003-01-3179).

[195] Miller, A. L., Stipe, C. B., Habjan, M. C., and Ahlstrand, G. G. *Role of lubrication oil in particulate emissions from a hydrogen-powered internal combustion engine. Environmental science & technology*, 2007. volume 41(19):6828–6835.

[196] Sonntag, D. B., Bailey, C. R., Fulper, C. R., and Baldauf, R. W. *Contribution of lubricating oil to particulate matter emissions from light-duty gasoline vehicles in Kansas City. Environmental science & technology*, 2012. volume 46(7):4191–4199.

[197] Pirjola, L., Karjalainen, P., Heikkil´a, J., Saari, S., Tzamkiozis, T., Ntziachristos, L., Kulmala, K., Keskinen, J., and R´onkk´o, T. *Effects of fresh lubricant oils on particle emissions emitted by a modern gasoline direct injection passenger car. Environmental science & technology*, 2015. volume 49(6):3644–3652.

[198] De Petris, C., Giglio, V., and Police, G. *Some insights on mechanisms of oil consumption. SAE Technical Paper*, 1996. (961216).

[199] Yilmaz, E., Thirouard, B., Tian, T., Wong, V. W., Heywood, J. B., and Lee, N. *Analysis of Oil Consumption Behavior during Ramp Transients in a Production Spark Ignition Engine. SAE Technical Paper*, 2001. (2001-01-3544).

[200] Graskow, B. R., Kittelson, D. B., Abdul-Khalek, I. S., Ahmadi, M. R., and Morris, J. E. *Characterization of exhaust particulate emissions from a spark ignition engine. SAE Technical Paper*, 1998. (980528).

[201] Tonegawa, Y., Oguchi, M., Tsuchiya, K., Sasaki, S., Ohashi, T., and Goto, Y. *Evaluation of Regulated Materials and Ultra Fine Particle Emission from Trial Production of Heavy-Duty CNG Engine. SAE Technical Paper*, 2006. (2006-01-3397).

[202] Stanglmaier, R. H., Li, J., and Matthews, R. D. *The effect of in-cylinder wall wetting location on the HC emissions from SI engines. SAE Technical Paper*, 1999. (1999-01-0502).

[203] Di Iorio, S., Sementa, P., and Vaglieco, B. M. *Experimental investigation on the combustion process in a spark ignition optically accessible engine fueled with methane/hydrogen blends. International journal of hydrogen energy*, 2014. volume 39(18):9809–9823.

[204] Sutton, M., Britton, N., Otterholm, B., Tengström, P., Frennfelt, C., Walker, A., and Murray, I. *Investigations into lubricant blocking of diesel particulate filters. SAE Technical Paper*, 2004. (2004-01-3013).

[205] Di Iorio, S., Sementa, P., and Vaglieco, B. M. *Experimental Characterization of an Ethanol DI-Gasoline PFI and Gasoline DI-Gasoline PFI Dual Fuel Small Displacement SI Engine. SAE Technical Paper*, 2015. (2015-01-0848).